Tampere University

HOY-MY PHUNG

Semiconductor Membrane External-Cavity Surface-Emitting Lasers (MECSELs)

Power scaling, thermal management, and wavelength extension

Tampere University Dissertations 519

Tampere University Dissertations 519

HOY-MY PHUNG

Semiconductor Membrane External-Cavity Surface-Emitting Lasers (MECSELs)

Power scaling, thermal management, and wavelength extension

ACADEMIC DISSERTATION
To be presented, with the permission of
the Faculty of Engineering and Natural Sciences
of Tampere University,
for public discussion in the auditorium SA203
of the Sähkötalo Building, Korkeakoulunkatu 3, 33720 Tampere,
on 22nd of November 2021, at 12 o'clock.

ACADEMIC DISSERTATION
Tampere University, Faculty of Engineering and Natural Sciences
Finland

Responsible supervisor and Custos
Professor
Mircea Guina
Tampere University
Finland

Supervisor
Postdoctoral Research Fellow
Hermann Kahle
Tampere University
Finland

Pre-examiners
Professor
Ursula Keller
ETH Zürich
Switzerland

Professor
Mansoor Sheik-Bahae
University of New Mexico
United States of America

Opponent
Professor
Arnaud Garnache
University of Montpellier
France

Cover design: Roihu Inc.

ISBN 978-952-03-2206-9 (print)
ISBN 978-952-03-2207-6 (pdf)
ISSN 2489-9860 (print)
ISSN 2490-0028 (pdf)
http://urn.fi/URN:ISBN:978-952-03-2207-6

PunaMusta Oy – Yliopistopaino
Joensuu 2021

Dedicated to my family.

ACKNOWLEDGMENTS

The completion of my dissertation would not have been possible without the endless and invaluable support and help as well as opportunities that I have all received.

First of all, I would like to thank my supervisor, Professor Mircea Guina who provided me the opportunity to come to Finland and join the ORC and work at the MECSEL project in such a wonderful environment. I am thankful for his trust, freedom, being straight-forward, and profound belief in my abilities. Special thanks to all the guidance and support in performing and finalizing my PhD study.
I would also like to thank Professor Arnaud Garnache for taking over the PhD exam, Professor Ursula Keller and Professor Mansoor Sheik-Bahae for the report of my thesis.
I am extremely grateful to my instructor, my laser-idol, Dr. Hermann Kahle, who taught me anything about lasers from the very beginning of my research work, and also took me into the MECSEL business in Tampere.
For the financial support, I would like to thank the Academy of Finland, the Finnish National Agency for Education (Opetushallitus), the Magnus Ehnrooth Foundation, the Finnish Foundation for Technology Promotion.
Many thanks to Patrik Rajala and Dr. Sanna Ranta who have fabricated so many awesome laser structures that were essential for the success of the thesis. At this point, I would also like to acknowledge Prof. Dr. Cyril Paranthoën, Prof. Dr. Christophe Levallois, Prof. Dr. Mehdi Alouini and the whole Institut FOTON research group for the QD MECSEL collaboration.
I would also like to thank the whole MECSEL team, Philipp Tatar-Mathes for being my MECSEL team mate, Aaron Rogers for proof-reading the articles and manuscript, and also Antti Rantaniemi, Roope Vuohenkunnas, and Jesse Koskinen for all the help with the measurements. I enjoyed to work with you together, and also all other events we had outside from the university.

I would like to acknowledge Dr. Antti Tukiainen, Dr. Antti Härkönen, and Jussi-Pekka Penttinen for sharing their expertise in optics, semiconductors, and lasers, and also Dr. Teemu Hakkarainen for the μPL measurements.
I would like to thank Abhiroop Chellu and Nouman Zia for their help in labs for the SEM measurements and the Logitech Lapping device as well as for their friendship.
For technical help, special thanks goes to Mervi Koskinen, Mariia Bister, Maija Karjalainen, Ilkka Hirvonen, Jarno Reuna, and Riku Koskinen.
I wish to thank Anne Viherkoski and Marketta Myllymäki for the professional help in all my administrative questions.
I would like to thank all colleagues for the great time and good discussions in semipub. Thanks to you, I felt very warmly welcomed even though I arrived at the coldest and darkest time of Tampere.
Special thanks goes to my amazing friends in Tampere and Stuttgart. I appreciate our friendship and the unforgettable activities we had over the years.
Last but not least, I thank my family for all the support.

Thank you!

Tampere, 16.08.2021
Hoy-My Phung

ABSTRACT

Research on semiconductor disk lasers has been driven by their unique features enabling multi watt output power operation with an excellent beam quality. Wavelength versatility is one further key advantage of this technology and is enabled by band gap engineering of various types of available semiconductor gain materials. The wavelength coverage of semiconductor disk lasers is thus, broad and ranges in the fundamental emission from the red to the near infra red. Further extending the wavelength versatility of semiconductor lasers, this work concentrates on an alternative approach, the membrane external-cavity surface-emitting laser (MECSEL), which is similar to a classical semiconductor disk laser but without a distributed Bragg reflector (DBR) and the substrate. The absence of the DBR offers more flexibility in gain chip fabrication. When it comes to thermal management, the gain region in the form of a membrane is cooled between two intra cavity heat spreaders. This double-side cooling approach is remarkable in thermal management, since the gain membrane can be already cooled with relatively poor but more cost-effective heat spreaders, such as silicon carbide (SiC) or sapphire heat spreaders. To better estimate the heat dissipation capability, thermal simulations that are based on experiments, are presented. Several pumping techniques are applied in various MECSEL gain regions emitting in the near infra red spectral regions for power scaling. These techniques include double-side pumping, pump beam area optimization, and parabolic mirror pumping which are relevant for the heat and charge carrier distribution within the membrane and can be applied to generate high power semiconductor membrane lasers. One part of this work concentrates on the critical 1.5 µm wavelength region, at which the DBR quality is low for monolithic integration. A MECSEL with an InAs/InP quantum dot gain membrane sandwiched between two SiC heat spreaders, provides 320 mW output power and 86 nm tuning range. Compared with previous semiconductor disk lasers with a monolithic DBR in this wavelength region, the thermal resistance of 2.3 K/W is more than two orders of magnitude lower.

CONTENTS

1 Introduction 1
1.1 MECSELs state-of-the-art 4
1.2 Research questions 7
1.3 Outline of the thesis 8

2 MECSEL operation principles 11
2.1 MECSEL gain membrane region 11
2.2 Optical pumping 12
2.2.1 Barrier and in-well pumping 12
2.2.2 Pump arrangements 13
2.3 Laser cavity design aspects 16
2.4 Thermal management 18
2.4.1 Thermal effects 18
2.4.2 Use of double intra cavity heat spreaders 19
2.4.3 Heat transfer simulation 21
2.5 Integrated gain bandwidth 21

3 Experimental methods 25
3.1 Material system 25
3.2 Molecular beam epitaxy 27
3.3 Structure pre-characterization methods after growth 28
3.4 Assessment of the heat spreader optical quality 31
3.5 Processing 32

4 Simulation of thermal behavior 35

4.1 Finite-element modeling 36
4.2 Simulation parameters 37
4.3 Relevance of the contact surfaces 40
4.4 Heat spreader materials and configurations 41
4.4.1 Power scalability with various types of heat spreaders 41
4.4.2 Significance of double-side cooling 43
4.5 Relevance of the pumping conditions 46
4.5.1 Lateral power scaling 46
4.5.2 Gaussian and super-Gaussian pump beam profile 49
4.6 Conclusion 50

5 From single-side to double-side pumping 53
5.1 SSP vs. DSP with SiC 54
5.1.1 Gain membrane #1 54
5.1.2 Experimental setup 55
5.1.3 Comparison of the output power performance 56
5.1.4 Spectral characteristics 57
5.1.5 Thermal investigations 58
5.1.6 COMSOL Multiphysics® simulations 60
5.2 DSP with sapphire heat spreaders 63
5.2.1 Gain membrane #2 63
5.2.2 Cavity and pump configurations for gain membrane #2 65
5.2.3 Power performance 65
5.3 Conclusion 66

6 High-power 8XX nm MECSELs 69
6.1 Gain membrane 70
6.2 Experimental setup 71
6.3 Results 72
6.3.1 Power characteristics 72
6.3.2 Optimal outcoupling value 74

6.3.3 Covering a spectral gap in the short 8XX nm region 75
6.3.4 Thermal resistance 76
6.3.5 Thermal lensing and its effect on the beam quality 77
6.4 Conclusion 81

7 Quantum dot MECSEL at 1500 nm 83
7.1 Gain membrane 84
7.1.1 Photoluminescence before and after processing 85
7.2 Experimental setup 85
7.3 Results 87
7.3.1 Power performance 87
7.3.2 Thermal resistance 88
7.3.3 Spectral characteristics 89
7.3.4 Beam quality 89
7.3.5 Degree of linear polarization 90
7.4 Conclusion 92

8 Summary and future work 95

References 99

Publication I 119

Publication II 125

Publication III 131

Publication IV 139

List of Figures

1.1 Schematic drawing of an LD and a VCSEL [7]. 2

1.2 Schematic drawing of an optically pumped VECSEL [11]. 3

1.3 Schematic drawing of a MECSEL with a linear cavity [33]. 5

1.4 Photograph of a red-emitting MECSEL from Kahle et al. from 2016 [29]. 6
1.5 Scheme illustration of the approaches in thermal management and wavelength extension of this thesis. 8

2.1 Schematic drawing of a resonant periodic gain (RPG) structure within a semiconductor membrane gain region. 11
2.2 Double-side pumping concept originating from a Nd:YAG rod laser, end-pumped with four 10 W diode laser bars [51]. 14
2.3 Schematic drawing of a 90° off-axis parabolic mirror. 15
2.4 Schematic drawing of a VCSEL array pumped VECSEL using a parabolic mirror [52]. 16
2.5 Simulated VECSEL beam brightness and the applied Gaussian pump power plotted against the cavity mode/ pump mode area ratio, w_0/w_p by Laurain et al. [59]. 17
2.6 Simulations of the maximum temperature rise within the gain region as a function of the incident power for different cooling approaches. 20
2.7 Integrated gain factor for a gain structure with twelve QWs for z = 0.75 λ_0 and z = 100.25 λ_0 at λ_0 = 1.05 µm [38]. 23
2.8 Calculated integrated gain near λ_0 = 1.05 µm for (a) z = L/2 and (b) z = L/10. [38] 24

3.1 Band gap energy with the corresponding wavelength plotted over the lattice constant of various types of III-V compound semiconductors at 300 K. 25
3.2 Schematic drawing of an MBE chamber [93]. 27
3.3 SEM image of an as-grown GaInAsP MECSEL structure for an emission around 800 nm taken with the back scattered electron signal. . . 29

3.4 PL measurement performed for the 825 nm GaInAsP MECSEL structure at room temperature with (a)-(c) a PL mapping system Accent RPM 2000 across the whole wafer, and (d) at a separate vertical PL setup where the pump power is manually adjustable. 30

3.5 Surface-top view microscope images of the semiconductor structure from a Nikon Eclipse optical microscope. 33

4.1 FEM mesh for the MECSEL gain sandwich. 36

4.2 Spectral shift measurements with the dissipated power and heat sink temperature of the 800 nm MECSEL. 39

4.3 FEM simulation of the 800 nm MECSEL with two 350 µm thick SiC heat spreaders. 40

4.4 Relevance of the bonding layer property. 41

4.5 Temperature rise plotted over the heat spreader thickness for SiC at various pump diameters d_{p}. 42

4.6 Temperature rise plotted over the heat spreader thickness for sapphire at various pump diameters d_{p}. 42

4.7 Temperature rise plotted over the heat spreader thickness for diamond at various pump diameters d_{p}. 43

4.8 Cross-section view of a single-side cooled gain membrane. 44

4.9 Comparison between SSC and DSC for various heat spreaders at varying thicknesses. 45

4.10 Radial average temperature rise plotted over the pump beam diameter for various heat spreaders. 46

4.11 Temperature contour plots at various d_{p} and constant pump power density. 48

4.12 Relevance of the gain membrane thermal conductivity. 49

4.13 Radial average temperature rise of the gain membrane pumped by a Gaussian and a 10^{th} order super-Gaussian pump beam profile. 50

5.1 A photograph of the 780 nm emitting MECSEL with a double-side pump approach. 53
5.2 T-matrix simulation of the electric field distribution and refractive index along the 780 nm gain membrane. 54
5.3 Schematic drawing of the MECSEL setup with the used laser mirrors M1, M2, and M3 for the V-cavity, and the measurement devices for the characterization of single-side and double-side pumping. 55
5.4 Output power comparison in SSP1 (pump arm 1) and DSP configurations at 20°C. 57
5.5 HR spectrum of the free-running 780 nm MECSEL. 57
5.6 Wavelength tuning results of the 780 nm MECSEL. 58
5.7 Spectral shift of the MECSEL in relation to the dissipated power and the heat sink temperature. 59
5.8 Simulated maximum temperature (dash dots) and radial average temperature (short dashes) within the 577 nm thick gain membrane using SSP (red) and DSP (black). 61
5.9 Maximum temperature increase plotted versus the membrane thickness. 62
5.10 Temperature increase averaged over the radial distance from the center of the membrane plotted versus the membrane thickness. 62
5.11 Vertical temperature distribution across a 500 nm thin membrane. . 63
5.12 Vertical temperature distribution across a 1.5 µm thick membrane compared between SSP and DSP at 9 W absorbed pump power. 63
5.13 Transmission measurements through the sapphire - 760 nm membrane - sapphire sandwich. 64

5.14 Power performance of a 760 nm sapphire MECSEL, gain membrane #2. 65
5.15 Spectral characteristics of the 760 nm sapphire-cooled MECSEL. . . . 66

6.1 A photograph of the 825 nm emitting MECSEL during operation. . . 69
6.2 T-matrix simulation of the electric field distribution and refractive index along the MECSEL structure. 70
6.3 Schematic drawing of the 825 nm emitting MECSEL setup with the double-side pump arrangement. 71
6.4 Power scaling results in an 825 nm MECSEL. 72
6.5 Optimal outcoupling mirror transmission in cavity 2 for the 825 nm MECSEL around 1.2%. 75
6.6 HR spectrum of the free-running 825 nm MECSEL measured with an Ando AQ6317C OSA with an average time of 20 s. 75
6.7 Wavelength tuning with a 2 mm thick intra cavity birefringent filter and $T_{M3} = 2.5\%$ outcoupling mirror at $P_{abs} = 11.5\,W$. 76
6.8 Spectral shift measurements of the 825 nm MECSEL. 76
6.9 Beam profile measured at 3.4 W (left), 6.8 W (center), and 10.2 W (right) absorbed pump power. 77
6.10 Beam diameter, beam waist positions, divergence angles, and beam waist diameter ob-tained from the M^2 measurement in cavity 2. 78
6.11 Simulated beam diameter within the cavity 2 in tangential plane for a laser emission wavelength of 825 nm. 79
6.12 Thermal lens dioptric power by the ray matrix from the ray matrix calculations based on the experimental data. 80

7.1 T-matrix simulation of the electric field distribution (red lines) and refractive index (grey lines) along the asymmetric QD MECSEL structure. 84
7.2 PL spectrum of the QD MECSEL structure before and after processing. 85

7.3 Schematic drawing of the 1.5 µm QD MECSEL. 86
7.4 Total output power of the 1.5 µm QD MECSEL measured at all transmitted beams from the V-cavity. 87
7.5 Spectral shift of the QD MECSEL with the dissipated power and the heat sink temperature. 88
7.6 Output power plotted versus emission wavelength, which is tuned by rotating a 1.5 mm thick birefringent filter set at Brewster's angle. . 89
7.7 M^2 measurement of the QD MECSEL along both tangential and sagittal axis using a dual scanning-slit BP209-IR/M beam profiler and a Thorlabs M2 M2MS measurement system. 90
7.8 Photograph of the 1.5 µm QD MECSEL setup with a linear cavity used to characterize the degree of linear polarization. 91
7.9 Output recorded at two orthogonal angles of the polarizer transmission axis from M2. 91
7.10 Polarization investigations of the QD MECSEL. 92

8.1 Overview of MECSEL results showing the maximum output power reached at different wavelengths. 95

List of Tables

3.1 Etching solutions for GaAs substrates with an AlAs process layer used for the wet-chemical process in this work. 33
3.2 Etching solutions for InP substrates with an InGaAs etch stop layer used in this work. 34

4.1 Simulation parameters for the FEM thermal model 38

5.1 Parameters used in the simulation. 61

ABBREVIATIONS

CB	Conduction band
DBR	Distributed Bragg reflector
DSC	Double-side cooling
DSP	Double-side pumping
EEL	Edge-emitting laser
FEM	Finite-element method
FSR	Free spectral range
FWHM	Full width at half maximum
HR	Highly reflective
Laser	Light amplification by stimulated emission of radiation
LD	Laser diode
LIDAR	Light detection and ranging
LIGO	Laser interferometer gravitational-wave observatory
MBE	Molecular beam epitaxy
MECSEL	Membrane external-cavity surface-emitting laser
MOVPE	Metal-organic vapour phase epitaxy
MQW	Multi quantum well
OCT	Optical coherence tomography
PL	Photoluminescence
QD	Quantum dot
QW	Quantum well

RHEED	Reflection high-energy electron diffraction
RPG	Resonant periodic gain
RPM	Revolutions per minute
SEM	Scanning electron microscopy
SESAM	Semiconductor saturable absorber mirror
SiC	Silicon carbide
SSC	Single-side cooling
SSP	Single-side pumping
TEC	Thermoelectric cooling
VB	Valence band
VCSEL	Vertical-cavity surface-emitting laser
VECSEL	Vertical-external-cavity surface-emitting laser
XRD	X-ray diffraction

ORIGINAL PUBLICATIONS

Publication I H. Kahle, J.-P. Penttinen, H.-M. Phung, P. Rajala, A. Tukiainen, S. Ranta and M. Guina. Comparison of single-side and double-side pumping of membrane external-cavity surface-emitting lasers. *Optics Letters* **44**, 5 (2019), 1146–1149. DOI: 10.1364/OL.44.001146.

Publication II H.-M. Phung, H. Kahle, J.-P. Penttinen, P. Rajala, S. Ranta and M. Guina. Power scaling and thermal lensing in 825 nm emitting membrane external-cavity surface-emitting lasers. *Optics Letters* **44**, 2 (2020), 547–550. DOI: 10.1364/OL.382377.

Publication III H.-M. Phung, P. Tatar-Mathes, C. Paranthoën, C. Levallois, N. Chevalier, M. Perrin, A. Kerchaoui, H. Kahle, M. Alouini and M. Guina. Quantum dot membrane external-cavity surface-emitting laser at 1.5 µm. *Applied Physics Letters* **118**, 23 (2021), 231101. DOI: 10.1063/5.0053961.

Publication IV H.-M. Phung, P. Tatar-Mathes, A. Rogers, P. Rajala, S. Ranta, H. Kahle and M. Guina. Thermal behavior and power scaling potential of membrane external-cavity surface-emitting lasers (MECSELs). *XXX* (2021). Submitted for publication to IEEE Journal Quantum Electronics. DOI: N/A.

Author's contribution

Publication I The author contributed as a co-author in writing the manuscript. She supported Hermann Kahle in the structure processing. The author performed the measurements and analyzed the data to-

gether with Hermann Kahle. The structure was designed and fabricated by Sanna Ranta and Patrik Rajala. Hermann Kahle, Jussi-Pekka Penttinen, and Antti Tukiainen were involved in the structure design. Mircea Guina contributed to the manuscript writing process.

Publication II — The author processed the structure, built the experimental setup, coordinated the experiments with Hermann Kahle and performed the measurements. The structure was fabricated by Sanna Ranta and Patrik Rajala. Hermann Kahle and Jussi-Pekka Penttinen supported in the structure design. The measurement data was analyzed by the author together with Hermann Kahle. The author wrote the manuscript under the guidance of Mircea Guina.

Publication III — The work was performed in collaboration with the Institut FOTON from the University of Rennes, France. Cyril Paranthoën, Christophe Levallois, Nicolas Chevalier, Mathieu Perrin, Anwar Kerchaoui, and Mehdi Alouini designed and fabricated the structure. Together with Philipp Tatar-Mathes, the author processed the structures. The author was responsible for the setup design and construction, performed the measurements and wrote the manuscript. The experiments were planned with all the co-authors. Hermann Kahle coordinated the experiments, and Mircea Guina the manuscript writing process.

Publication IV — The author planned the experiments with the co-authors. Aaron Rogers built the experimental setup and measured the thermal resistance. The author processed the structures with Philipp Tatar-Mathes. The structure was designed and fabricated by Hermann Kahle (design), Patrik Rajala and Sanna Ranta (design and fabrication). The author carried out the thermal simulations and wrote the manuscript. All the work was guided by Hermann Kahle and Mircea Guina.

1 INTRODUCTION

Nowadays, light amplification by stimulated emission of radiation, abbreviated as Laser [1], is an important technology used in many fields including industry, medicine, meteorology, optical data storage, data communication, or research. With such diverse fields of applications, the laser has contributed either directly or indirectly to a more simple day-to-day life. In industrial manufacturing processes, common applications are laser cutting, boring, welding, and engraving as lasers work more accurate and faster than other methods. Furthermore, lasers play a crucial role in a few clinical procedures, such as cancer therapies, ophthalmic surgeries, and skin treatments. Most recent high-resolution imaging such as optical coherence tomography (OCT) [2] relies on lasers. For scientific research, lasers are optimized for spectroscopy, quantum experiments as well as light detection and ranging (LIDAR). Without a laser, optical tweezers [3] would not exist for which the Physics Nobel prize 2018 was awarded. Also, there would be no recent scientific breakthrough in the detection of gravitational waves with the laser interferometer gravitational-wave observatory (LIGO) [4]. For this, also a Nobel Prize was awarded in 2017. Frontiers of laser features are continuously advanced and new developments are likely to continue long into the future.

It is evident that all the different applications require different properties, such as emission wavelength, beam quality, or output power in continuous-wave or pulsed operation. These specific requirements are mainly defined by the applications. As soon as the requirements are known, various types of laser gain media, such as gases, doped solid-state crystals, or semiconductors, are chosen to tackle the problem.

Among the various types of gain media, semiconductors possess the feature that the band gap can be modified to a large extent by varying the material composition. This technique called band gap engineering is a material-intrinsic feature and allows a wide spectral coverage from the blue to the mid-infrared. The operational properties can be influenced by the circumstances under which the laser is operating, such

as the way of pumping and laser architecture.

If we now turn our view to semiconductor lasers, laser diodes (LDs) [5] are well-developed and available with a large wavelength versatility. LDs are electrically driven with a pn-junction. As the schematics shows in Fig. 1.1, this makes LDs compact and therefore, attractive for industrial and medical applications. By stacking several LDs on top of each other to one- or two-dimensional bars, high-power laser diode modules can be realized. The laser cavity is formed by two cleaved-facet ends which makes LD thus, suitable for cost-efficient mass-production. The main disadvantage of LDs is that they are edge-emitters and have a high beam divergence. To obtain a circularly symmetric beam, the high beam ellipticity of the LD usually requires complicated beam shaping optics.

With the monolithic integration of two distributed Bragg reflectors (DBRs), surrounding the gain region, the laser cavity in vertical-cavity surface-emitting lasers or VCSELs [6] can be formed perpendicularly to the semiconductor layer plane as shown in Fig. 1.1. The gain region with a typical thickness below one micrometer, is laterally homogeneous and does not distort the intra cavity beam as it is the case in LDs. Therefore, VCSELs offer circularly symmetric high-quality beams instead of elliptical ones. Either pumped electrically or optically, a VCSEL unit can usually achieve output powers of a few milli watts only, which is principally limited by the small cavity mode dimensions. In summary, the drawback of the compact LDs is the poor beam quality while the output power that can be achieved by VCSELs is not very high.

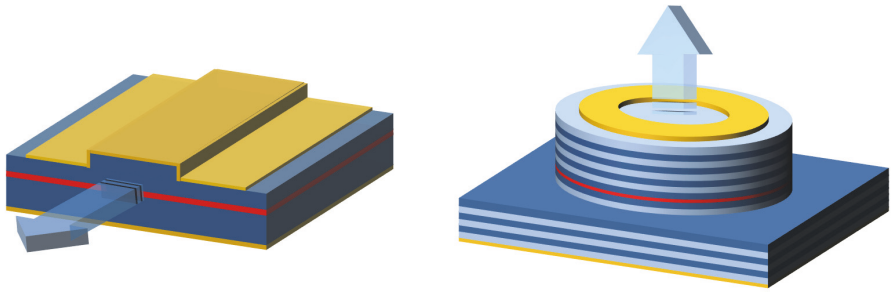

Figure 1.1 Schematic drawing of an LD (left) and a VCSEL (right) [7]. With the optical cavity formed by two cleaved-facet ends in an LD, the light emission occurs in plane of the semiconductor layer (red). In a VCSEL, the optical cavity is formed by a top and a bottom DBR (blue-lightblue stripes) surrounding the semiconductor layer (red) which permits light emission from the surface of the semiconductor layer (red) in the VCSEL.

Besides the LD and VCSEL technology, a versatile platform, the vertical-external-cavity surface-emitting laser (VECSEL) [8, 9] has emerged by combining the benefits of semiconductor lasers and thin-disk solid-state lasers [10]. After Kuznetsov et al. [11] demonstrated a VECSEL capable of high-power operation with a near-diffraction limited beam quality operating at room temperature conditions in 1997, the VECSEL technology has attracted special attention in research. The main components of the VECSEL are a pump laser and a semiconductor chip, incorporating the gain region and a monolithically integrated DBR. A laser cavity is formed between the DBR and one or more external laser mirrors. As schematically shown in Fig. 1.2, the VECSEL is indeed more bulky in comparison with LDs and VCSELs but offers a few advantages, which are only hardly feasible by a waveguide cavity and electrical pumping.

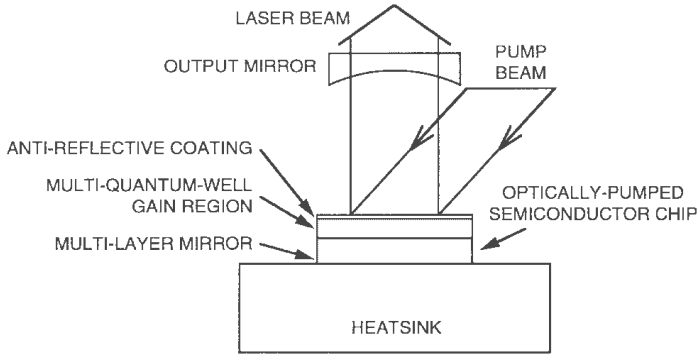

Figure 1.2 Schematic drawing of an optically pumped VECSEL [11]. The VECSEL chip includes a multi-quantum well gain region, a multi-layer mirror (which practically corresponds to the DBR) soldered to a heat sink.

A main advantage is that both, the operation mode and the pumped region are scalable in size, owing to the external cavity architecture and optical pumping [12]. This permits to increase the output power to a certain point at which the high quality of beam is still preserved as it is the case in thin-disk solid-state lasers [13]. In short terms, VECSELs are able to provide high output power with a high beam quality [14].

To improve the thermal management, one common method is to contact an intra cavity heat spreader, which is transparent for the pump and lasing wavelength, on top of the gain region [15–17]. Generally, a high intra cavity power is generated within the external cavity making VECSELs suitable for efficient intra cavity fre-

quency conversion [18–21]. Also, the external cavity provides huge flexibility in the implementation of intra cavity elements, including nonlinear frequency conversion crystals, linewidth narrowing or wavelength selecting elements as etalons or birefringent filters [22–24], or semiconductor saturable absorber mirrors (SESAMs) [25] for pulsed operation.
To date, the high power VECSELs exceeding 106 W in multi transversal mode [26] and 72 W in single transversal mode operation [14] have been demonstrated around the 1 µm wavelength region. The reliable, high laser performance is mainly enabled by the mature development stage of the InGaAs and AlGaAs material systems providing high DBR reflectivities, high carrier confinement, and reasonably high thermal conductivities. However, when turning away from this wavelength, different material systems are required and their performance is generally worse [27]. Due to various reasons, such as the maturity of technology or the intrinsic material properties, a combination of the relevant features of carrier confinement, thermal conductivity, and reflectivity of the DBR, will become increasingly difficult to handle at certain wavelengths [28]. For this reason, the power performance is neither equally distributed nor wavelength coverage is fully provided by VECSELs over the wavelength regions covered by typical III-V compound semiconductors. In more simple terms, we can emphasize that the main limitation comes from the DBR as its layer components need a fairly high refractive index contrast. At the same time, the DBR material should be suitable for monolithic integration. The lattice constant in that sense needs to be nearly matched to the gain region and the substrate lattice. All these features are available for the 1 µm region, but lacking for other wavelength regions. For instance, the gain region for the 1.3 µm - 1.5 µm wavelength region is covered by the InP material system but lacks of suitable InP DBR materials while the InP-based gain region is only hardly compatible with GaAs/AlGaAs DBRs without inducing much excessive strain into the structure.

1.1 MECSELs state-of-the-art

To exploit a broader wavelength coverage offered by the III-V material compounds than it would be possible with the conventional VECSELs, and also to elevate the gain heterostructure performance by a more efficient thermal management, the membrane external-cavity surface-emitting laser (MECSEL) [28, 29] has emerged. In this

alternative laser concept, the DBR is abandoned, which any way has a low thermal conductivity [30–32]. This has the benefit that it requires less development steps in structure design as well as epitaxial growth. Thus, only the laser-active quantum wells (QWs) or quantum dots (QDs) heterostructure is bonded between two transparent intra cavity heat spreaders. A very close contact to the heat spreaders, enables cooling of the gain region from two sides as illustrated in Fig. 1.3. The benefit of being more effective in thermal management in general allows the use of more cost-effective materials such as silicon carbide (SiC) or sapphire with a lower thermal conductivity, besides the diamond heat spreaders used for VECSELs.

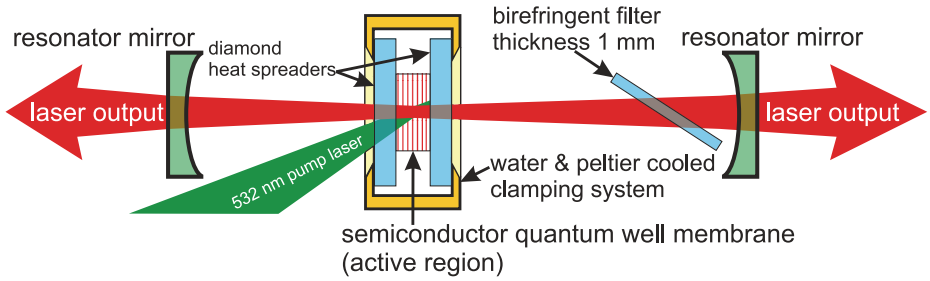

Figure 1.3 Schematic drawing of a MECSEL with a linear cavity [33].

Several research groups have contributed to the MECSEL focussing on a better thermal management and also a broader wavelength coverage. In 2008, Moloney et al. proposed the idea of cooling a VECSEL where the substrate is completely removed from both sides via two heat spreaders [34], one intra cavity, one directly behind the DBR. Six years later, a "double-diamond high-contrast-gratings vertical external cavity surface emitting laser", which is practically a MECSEL, but named differently at that time, has been proposed by Iakovlev et al [35]. The idea of sandwiching a gain membrane between two diamond heat spreaders has been proposed. High contrast gratings can be applied on both outer surfaces of the diamonds, where one grating serves as a pump mirror while the other grating takes the function of a back side laser mirror. Furthermore, the concept of operating a semiconductor gain medium in transmission mode is not new. A GaAs disk laser demonstrated by Le et al. in 1991 [36], as well as an AlGaInAs QWs disk laser from 2006 [37] operated in transmission. This was enabled by the substrates, which were transparent for the lasing wavelength.

In 2015, Yang et al. demonstrated the first MECSEL with the gain membrane bonded

onto a diamond heat spreader [28]. By this approach, the output power exceeded 2.5 W at 1160 nm and 10°C heat sink temperature. A better cooling of the gain membrane using two heat spreaders has been studied by thermal simulations and also proposed. At that time the membrane laser was called a "DBR-free VECSEL". In 2016, Kahle et al. have demonstrated a MECSEL with double-side cooling for the first time [29]. A photograph of the pioneering red-emitting MECSEL at around 657 nm and at a heat sink temperature of 10°C is depicted in Fig. 1.4. 595 mW output power was demonstrated.

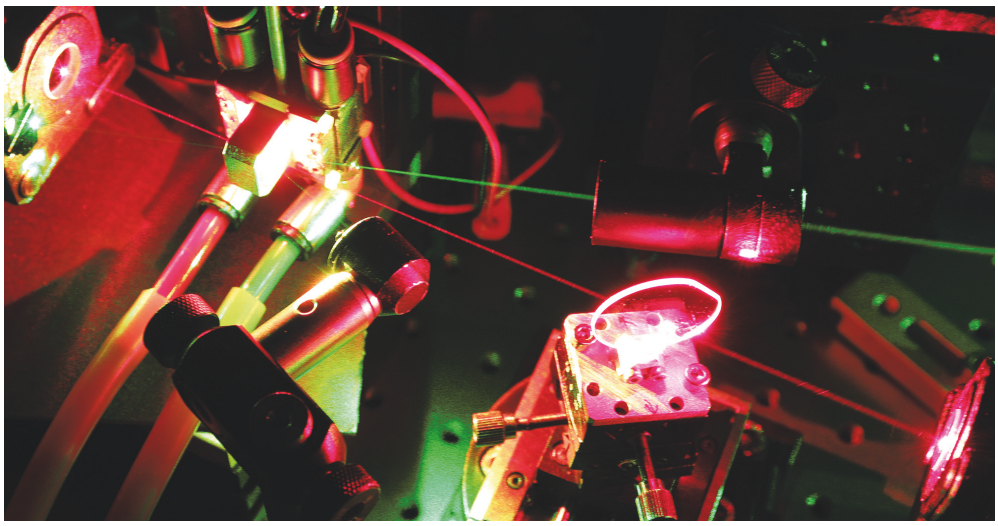

Figure 1.4 Photograph of a red-emitting MECSEL from Kahle et al. from 2016 [29]. The gain element is sandwiched between two intra cavity diamond heat spreaders and placed within a linear cavity. A birefringent filter positioned within the cavity was used for wavelength tuning.

The power performance was compared to a VECSEL with the identical gain structure of 5×4 GaInP QWs and AlGaInP barrier and cladding layers. The maximum output power for the VECSEL was 570 mW. The slope efficiency for the MECSEL resulted to be about 22.3 %, which was significantly higher than what has been achieved by the VECSEL with 18.8 %.
In the same year, a single-side diamond MECSEL with 12 InGaAs QWs provided more than 6 W output power at 1055 nm [38]. A high tuning range of 80 nm, which corresponds to 21.6 THz, was achieved. Also, a theoretical study based on the spatial position of the gain membrane within the laser cavity was presented by Yang et al. It was shown in the simulations that the gain bandwidth in MECSELs can be up to a factor two larger than conventional VECSELs with a standard resonant periodic

gain structure (RPG). The limitations in the VECSELs mainly arise from the DBR, which is directly attached to the gain and fixes the phase of the electric standing electric wave field. Furthermore, MECSELs are able to achieve larger wavelength tuning owing to the use of external dielectric mirrors which typically can provide a larger reflection band than it would be possible with semiconductor DBRs. In 2017, a MECSEL incorporating eight InGaAs QWs with an emission wavelength of 980 nm and 3.2 W maximum output power was demonstrated [39]. At 1007 nm, a MECSEL with ten InGaAs QWs provided more than 10.1 W (6 W) output power at a heat sink temperature of -10°C (12°C) using SiC heat spreaders [40]. Subsequently, over 16 W output power was achieved by a MECSEL with 12 InGaAs QWs in the gain membrane cooled by two SiC heat spreaders at 10.5°C [41]. A direct comparison in the laser performance shows that the output power is more than twice higher than achieved by the single heat spreader approach, which proves the more efficient heat dissipation. The latest results have presented a MECSEL operating around 1178 nm with 20 W maximum output power [42]. The gain membrane is made of eleven InGaAs QWs and GaAs barriers, and is cooled by SiC heat spreaders to -10°C.
Generally, research on MECSELs has been mainly concentrated on wavelength extension in particular for certain wavelength regions at which the DBR becomes difficult to handle. For instance, a MECSEL emitting at 1640 nm has been demonstrated with more than 1.2 W output power [43]. The gain membrane employs eight InGaAs QWs and was cooled to 2°C between two diamond heat spreaders. Subsequently, a 1770 nm-emitting MECSEL provided 3.5 W at 20°C [44, 45].

1.2 Research questions

The aim of this research work is to improve the performance of III-V semiconductor MECSELs in terms of output power by developing and applying advanced pumping arrangements. The work also includes the processing of MECSEL structures starting from the semiconductor wafer. As the double-heat spreader approach in the MECSEL generally points out its better thermal management compared with the single-heat spreader approach, the key research questions are:

- What are the limits of thermal management in MECSELs and what influences them?

- How does the pumping arrangement affect the MECSEL performance?

On another line of work the development of MECSEL gain membranes are motivated by their ability of wavelength extension. In this work, we also address the critical 1.5 µm wavelength where also VECSELs have had limited success. To this end, the main research questions are:

- Is the MECSEL an alternative versatile platform for DBR-critical wavelength around 1.5 µm?
- How much better is the wavelength tunability in MECSELs than in conventional VECSELs at this wavelength range?

1.3 Outline of the thesis

The choronological approach of the research can be summarized in a schematic diagram as illustrated in Fig. 1.5.

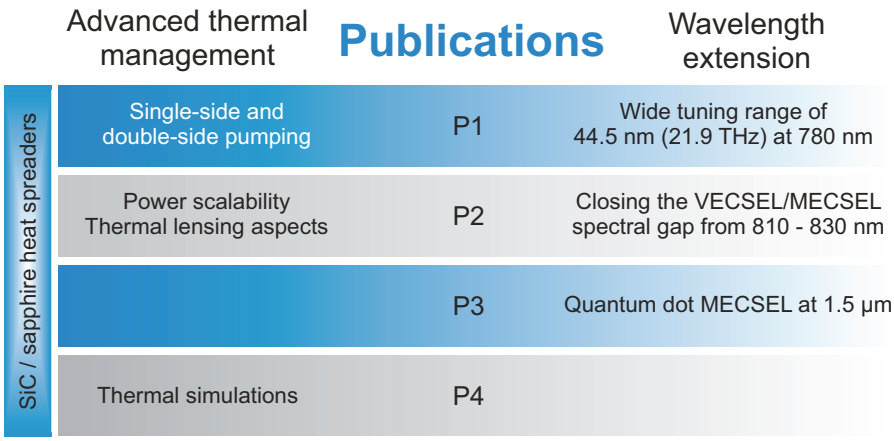

Figure 1.5 Scheme illustration of the approaches in thermal management and wavelength extension of this thesis.

The thesis is structured in eight chapters and reviews the results of the publications P1-P4. An introduction to the basic concepts of the MECSEL technology is given in chapter 2. It begins with the operation principles of the gain membrane, followed by the aspects of optical pumping, laser cavity design, and thermal management. Chapter 3 reviews the methodology, which has been applied for the fabrication, characterization, and processing of the MECSEL structures.

Chapter 4 presents the results of a finite-element analysis of a MECSEL (P4) to understand the limits of thermal management for different architectures. Based on the thermal simulations, it has been analyzed how several parameters of the heat spreaders, such as thermal conductivity and heat spreader thicknesses affect the temperature situation of a gain structure with a certain thickness. Also, the thermal situation has been studied at different pumping configurations. To validate the theoretical values, a comparison to the experiments is performed.
In chapter 5, the MECSEL lasing performance via single- and double-side pumping is compared in output power and thermal resistance. The results reveal how the pumping arrangement can improve the lasing are published as P1.
In chapter 6, the power scalability as well as thermal lensing effects are investigated. A QD MECSEL emitting at 1.5 µm is demonstrated in chapter 7. A 90° off-axis parabolic mirror is applied for pumping under small incident angles. Main focus here is the MECSEL practicability and the wavelength coverage. A conclusion and an outlook on further MECSEL challenges are given in the last chapter (8).

2 MECSEL OPERATION PRINCIPLES

In this chapter, general aspects of the MECSEL gain structure, thermal management, optical pumping, laser cavity design, and wavelength tunability are reviewed.

2.1 MECSEL gain membrane region

In a MECSEL, the gain element is the semiconductor membrane. A schematic drawing and a band diagram that illustrate the key elements of the semiconductor gain membrane region are illustrated in Fig. 2.1.

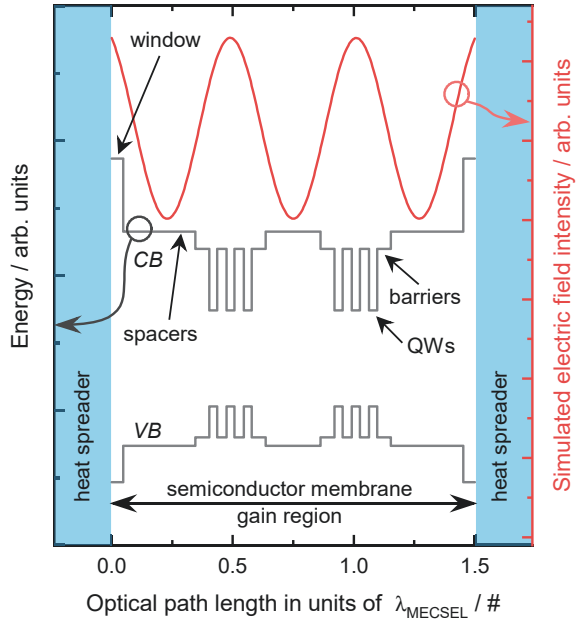

Figure 2.1 Schematic drawing of a resonant periodic gain (RPG) structure within a semiconductor membrane gain region. Illustrated is the conduction band (CB) minimum and the valence band (VB) maximum (left y-axis), and the simulated electric field intensity (right y-axis). For barrier-pumping, absorption takes place in the QWs and barriers/spacers, and emission in the QWs.

The MECSEL's gain region is similar to those used in VECSELs. It consists of low-dimensional structures, i.e. quantum wells (QWs) or quantum dot (QD) layers providing the gain via optical pumping. To prevent charge carrier diffusion and produce population inversion, QWs or QD layers are separated by higher-band gap barrier layers.
In this work, all layers in the gain region are made of III-V undoped compound semiconductors. The gain region can be individually designed for a wide of emission wavelengths by the various material compositions and the QW layer thickness. The overall thicknesses of the gain regions designed for the red and near-infrared spectral regions are below 2 µm whereas the thickness of a QW or QD layer is typically less than 10 nm. Because the radiative QWs or QD layers are so thin, the overall interaction length with the laser mode is small. To maximize the interaction and thus, also the modal gain, the radiative layers are positioned individually or in groups near the antinodes of the standing wave field of the laser mode. In such an arrangement, the structure is called a resonant periodic gain (RPG) structure [46, 47] and typically makes use of the resonances of the sub-cavity formed within the semiconductor membrane gain region to define the standing wave. To arrange the QWs or QW packages at the field antinodes in the sub-cavity, the antinodes should be separated by layers with an optical thickness that corresponds to a multiple of $\lambda_{\mathrm{MECSEL}}/2$.
In addition, both outer ends of the gain region are surrounded by window layers with a larger band gap than the barriers. These window layers confine the electrons and holes in the gain region and block them from diffusing to the semiconductor-heat spreader interface. This reduces the probability of non-radiative surface recombination, an unwanted effect taking place.

2.2 Optical pumping

2.2.1 Barrier and in-well pumping

To invert the population within the energy bands, the gain region is optically pumped, where electrons from the valence are lifted to the conduction band. In exchange of that, holes are created in the valence band. Both charge carriers, electrons and holes, then diffuse to the QWs, where the charge carriers are spatially confined, recombine, and release lasing photons of lower energy than the pump photons.

Here, the beam quality of the pump laser does not play a crucial role. Thus, low-cost and sufficient beam quality laser diodes that provide the needed pump power density can be used as a pump laser. These laser diodes are nowadays broadly developed at diverse emission wavelengths and partly available as fiber-coupled modules for a more convenient handling. Since semiconductors have typically a broad absorption spectrum, for optical pumping the pump laser does not need to meet a certain wavelength. There are only a few requirements to ensure a proper pump absorption in the gain region. For barrier-pumping, meaning that the pump beam is mainly absorbed in the barriers, the photon energy of the pump beam needs to be higher than the barrier band gap energy. Owing to the relatively high absorption coefficient which is in the range of $\sim 10^4 \mathrm{cm}^{-1}$, the gain region absorbs the pump beam during a single-pass well enough. As the gain medium operates in transmission mode, the pump absorption is a quantity that can be experimentally measured in a MECSEL. For instance, about 90% of the penetrating pump beam is absorbed in the ~ 577 nm thick gain region from Chapter 5.
The energy difference between the pump and lasing photon is known as the quantum defect, which is deposited as heat in the gain structure, and limits the laser performance in output power and efficiency. A way to reduce the quantum defect is to apply in-well pumping, where the pump photon energy is slightly higher than the QW band gap energy [21, 48–50]. Since pump absorption takes place only in the QWs, in-well pumping suffers from the reduced pump absorption. To compensate for the small absorption of a single pump pass, the pump beam is directed multiple times to the gain region (multi-pass pumping) to sum up the small fraction absorbed within each pass.

2.2.2 Pump arrangements

Single-side pumping. In conventional VECSELs, the gain region has been optically pumped from the surface side only. The Beer-Lambert law implies that the pump light absorbed in the gain structure decays exponentially in intensity. Thus, the pump light and charge carrier distributions become highly asymmetric for thick gain structures. However, this is generally not a critical issue. Only if the structure is too thick just so that the gain is increased, it may occur that the pump light cannot penetrate through the whole structure. This will lead to unpumped back side QWs

or QD layers, which will rather generate losses than gain.

Double-side pumping. The MECSEL allows the implementation of double-side pumping, meaning that the gain structure can be pumped from both sides. As shown in Fig. 2.2, such a pump arrangement originates from the architecture of solid-state lasers [51]. Since this double-side pumping allows a more homogeneous absorption of the pump, this pump arrangement can be beneficial in terms of operating efficiencies and power scaling. In P1, the laser performance is compared for single- and double-side pumping.

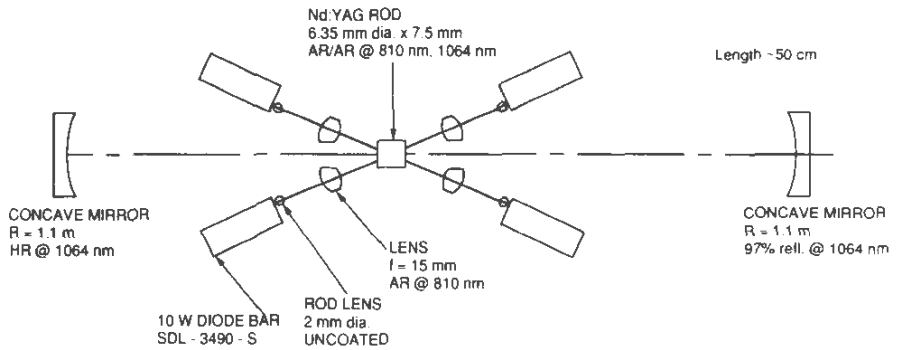

Figure 2.2 Double-side pumping concept originating from a Nd:YAG rod laser, end-pumped with four 10 W diode laser bars. This pumping concept was demonstrated by Tidwell et al. in 1992 [51].

Parabolic mirror pumping. If VECSEL or MECSEL gain structures are optically pumped by laser diodes, the pump incident angles have been usually reported to be larger than 20°. Such large incident angles are not only needed due to practical reasons. The focussing optics needs to be very close to the gain structure without cutting the intra cavity beam. By this, the pump beam shape turns out to be slightly elliptal, which can become disadvantageous in terms of mode-matching the pump to the cavity mode beam. Alternatively, the pump beam can be re-shaped to a circular one by a pair of cylindrical lenses. On the other hand, this increases the complexity of the pump optics without having spherical abberation. An alternative method of pumping the gain structures at an angle of less than 15°, is the use of a 90° off-axis parabolic mirror for focussing the beam [52]. Such a 90° off-axis parabolic mirror is able to focus a collimated pump beam without introducing any spherical abber-

ation. As can be seen in Fig. 2.3, the mirror surface corresponds to an excerpt of a paraboloid in a way to deflect and focus the collimated pump beam by 90°.

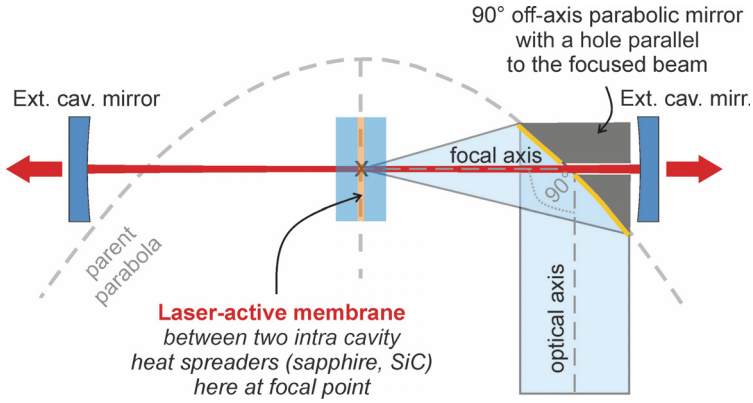

Figure 2.3 Schematic drawing of a 90° off-axis parabolic mirror. A collimated pump beam is focused by the parabolic mirror. For pumping a semiconductor membrane, it can be positioned to the focal point of the parabolic mirror. A hole with a diameter of ∼ 3 mm parallel to the focused beam allows to place the parabolic mirror in front of the semiconductor membrane without cutting the intra cavity MECSEL beam.

The gain structure can be basically positioned to the focal point. For the external cavity, one of the laser mirrors is typically placed behind the parabolic mirror. As such, the laser mirror does not need to be anti-reflection coated on the back surface for the pump beam. This arrangement is also advantageous in a way that the pump beam does not need to travel through the laser mirror, which could otherwise cause beam distortion and absorption losses. Also, the reflective coating of the mirror would have to be transparent for the pump. In our experiments (P3), we used a 90° off-axis parabolic mirror with a 3 mm diameter hole pointing parallel to the focal axis (Thorlabs (MPD249H-M01). In principle, double-side pumping is also possible with this pump arrangement for pumping thicker MECSEL structures in the future. To this end, one can implement the scheme proposed by Herper et al. using VCSEL arrays as a pump source and a parabolic mirror [52]. As can be seen in the schematic in Fig. 2.4, multiple VCSEL chips are mounted next to the VECSEL chip onto the same heat sink. A parabolic mirror on top directs the VCSEL pump beam onto the VECSEL chip. With such an arrangement an optical-to-optical efficiency of more than 26% has been achieved.

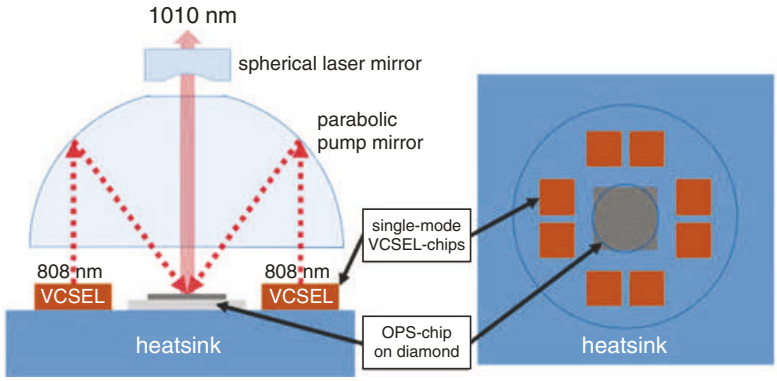

Figure 2.4 Schematic drawing of a VCSEL array pumped VECSEL using a parabolic mirror [52]. This pump arrangement mainly enables compactness of a semiconductor disk laser. Left shows the side-view, where, the VCSEL chips and the pumped VECSEL chip share the same heat sink. Right shows the top-view.

2.3 Laser cavity design aspects

Compared with conventional VECSELs, where the external cavity is formed by a monolithically integrated semiconductor DBR next to the gain region and an external laser mirror, the MECSEL completely avoids the DBR. Instead, two or more external mirrors are used for various types of cavity geometries. The simplest type is the linear cavity. A V- or Z-shaped cavity is used when intra cavity elements, such as a SESAM or a frequency doubling crystal, need to be placed at a specific cavity mode beam diameter for an efficient mode-locking [53–55] or intra cavity frequency conversion [18, 56, 57].

When the cavity geometry is known, cavity stability aspects must be considered. For a cavity made of two mirrors with the radii of curvature R_1 and R_2, and a total cavity length of L, the cavity stability criterion is given by [58]

$$0 \leq \left(1 - \frac{L}{R_1}\right) \cdot \left(1 - \frac{L}{R_2}\right) \leq 1. \tag{2.1}$$

The equation implies that the cavity must be able to reproduce the intra cavity beam within each cavity roundtrip. If the cavity is unable to refocus the beam, the beam will get only wider; optical feedback mechanism cannot be ensured and the cavity becomes unstable. The beam diameter distribution within the cavity is usually pre-simulated in advance using the ray matrix method for Gaussian beams. Here, typi-

cal parameters are the radius of curvature, mirror distances, and the emission wavelength. The intra cavity heat spreaders of the MECSEL sandwich are taken into consideration as an element placed near the intra cavity beam waist, whereas the semiconductor membrane is neglectable. It is simply too thin to matter in terms of intra cavity beam optics. Since the pumped area on the semiconductor membrane acts like a gain aperture and defines where the amplification takes place, the cavity mode area should spatially overlap with the pumped area. According to the simulations of Laurain et al. in Fig. 2.5 [59] for a VECSEL (which has been found in this thesis to also apply for the MECSEL as well), the pumped area can be slightly larger than the cavity mode area.

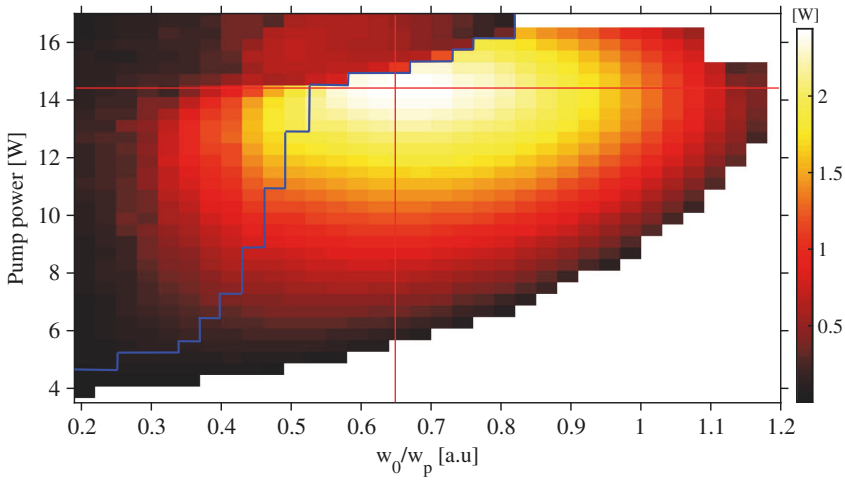

Figure 2.5 Simulated VECSEL beam brightness (right y-axis) and the applied Gaussian pump power (left y-axis) plotted against the cavity mode/pump mode area ratio, w_0/w_p by Laurain et al. [59]. The blue line highlights the transition between multi mode (left) and single mode (right) operation.

If the pump area is too large compared to the cavity mode area, the laser emits also in a higher-order transversal mode. On the other hand, too small pump regions reduces the power performance, due to the unpumped regions. For a Gaussian beam, a clear transition from the multi mode to the single transversal mode operation can be seen. In contrast to a super-Gaussian beam, which has a flatter pump power distribution, the transition for various pump powers does not occur at the same mode ratio if the pump power is increased. Instead, the transition moves towards a higher cavity mode / pump mode area ratio the higher the pump power gets. This is because the net spatial width of the gain grows with higher pump power in a Gaussian beam. Also, the

gain and temperature gradient is more pronounced. A Gaussian beam filters out the higher order modes more effectively, as the gain near the edges of the pump beam is much lower than in the center. As such, the transition from a multi mode to a single transversal mode occurs at a smaller cavity mode to pump mode area ratio. By considering the beam brightness, which is defined as the output power divided by the beam quality M^2 factor, an optimum can be found at a cavity to pump mode area ratio of $w_0/w_p = 0.65$. Near and above thermal rollover, the gain in the pup beam center is reduced due to heating effects, and higher order modes become more probable.

Typically, one of the laser mirrors serves as an outcoupler, being less reflective than the other mirrors of the cavity. With a higher transmission, there are two competing effects that defines the output. First, the output power increases because of the higher probability that photons are extracted from the cavity. This holds true until the photon extraction rate surpasses the photon generation rate in the cavity. A further increase of the outcoupler transmission would lead to a decrease of output power. Due to the relatively small gain volume of QWs and the low gain, the outcoupler transmission optimum for VECSELs and MECSELs is often in the range of $1-10\%$ [60, 61]. Dielectric mirrors, that are originally optimized for solid-state lasers and commercially available for different wavelength regions, can be directly applied in MECSELs.

2.4 Thermal management

2.4.1 Thermal effects

Owing to the quantum defect between the pump and laser emission, a fractional part of the pump photon energy is transferred to heat. If the temperature within the semiconductor gain region becomes too high, charge carriers are able to thermally escape from the QWs. This thermal issue especially becomes critical if the QWs are shallow. As a consequence, the rate of stimulated emission drops and thus also the gain.

In addition, the semiconductor band gap depends on the temperature. As such, heating up the gain medium causes a red shift of the gain spectrum. The sub-cavity resonance varies with the temperature as well, due to thermal expansion and the

temperature-dependent refractive index. Moreover, it is an issue that the gain and the sub-cavity resonance shift at different rates. If they become spectrally and spatially misaligned, it lowers the modal gain [62]. At this place, it should be mentioned that the reflectivity at the semiconductor heat spreader interface in a MECSEL is typically in the range of $\sim 10-20\%$. Hence, a low-finesse sub-cavity results and the MECSEL is less sensitive to the misalignment between the gain peak and the sub-cavity resonance than a VECSEL [38].
The rate of non-radiative processes, such as defect recombination or Auger recombination also increases at elevated temperatures. It should be noted here, that defect recombination is not significant in case of high quality crystal growth [63]. Nonetheless, all these effects from non-radiative recombination and quantum defect cause that the slope efficiency drops. The laser output power curve reaches its maximum, and thermal roll-over occurs at increased pumping. Furthermore, pump-induced heating can create a temperature gradient in a solid state gain medium [12]. From the thermo-optical effect, a refractive index gradient results, which leads to the formation of a thermal lens [64]. Such a thermal lens can be approximated by a GRIN or a physical lens which has a focussing or defocussing effect to the intra cavity beam. It should be considered here, that the cavity mode shape change is related to the temperature gradient or the pump power distribution. Thus, thermal lensing can cause a mode mismatch between the laser and the pump. Higher-order transversal modes that reduce the beam quality, can appear as summarized in the previous section. Thermal lensing has been used to control the cavity mode size in microchip VECSELs with a Fabry-Pérot cavity [65].

2.4.2 Use of double intra cavity heat spreaders

For power scaling, efficient thermal management is essential. As the pumped area on the semiconductor membrane is typically more than two orders of magnitude larger than the membrane thickness, the semiconductor membrane adapts the disk geometry from solid-state or semiconductor disk lasers [8, 10]. Accordingly, heat flow can be considered as one-dimensional, in axial direction of the membrane surface. A MECSEL fully exploits the potential of cooling the semiconductor membrane between two intra cavity heat spreaders without any other layers (such as the DBR) in between which would otherwise hamper the heat dissipation. As such, the thermal

simulations in Fig. 2.6 by Yang et al. [28] reveal a significantly lower maximum temperature rise within the gain region than the case of a thin device VECSEL without the substrate. Compared with the MECSEL with one heat spreader, the temperature rise in a double heat spreader MECSEL is about ∼ 30% lower.

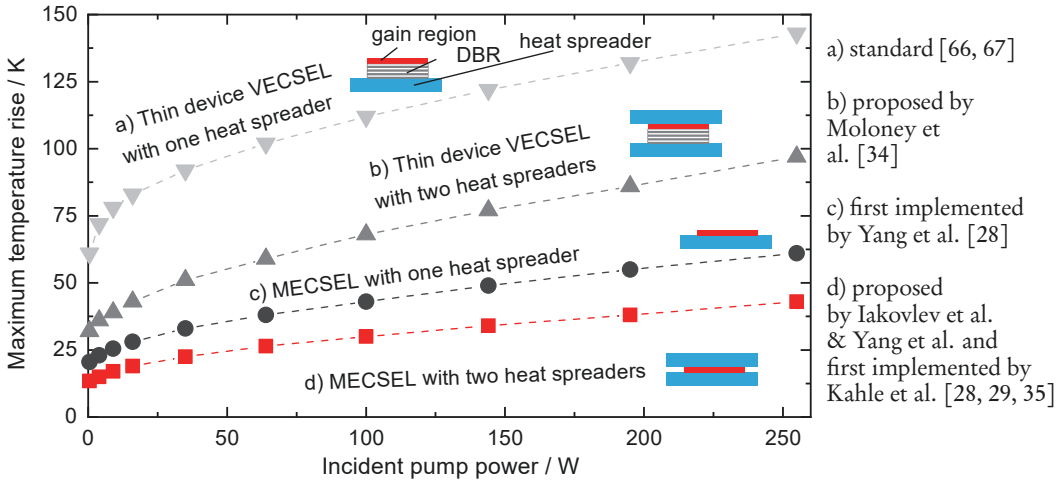

Figure 2.6 Simulations of the maximum temperature rise within the gain region as a function of the incident power for different cooling approaches a) - d). The data and images are adapted from Yang et al. [28]. Diamond is used as a heat spreader. The heat sink mount is not illustrated here.

Heat is dissipated through the heat spreaders and flows to the copper heat sink. Indium foil with a thickness of 50 µm inbetween is used to improve the thermal contact. Two different ways of cooling the gain membrane are applied in this thesis. By stabilizing the heat sink plate temperature with a peltier element or cooling it with a continuous water/glycol flow, the gain element has been cooled. When considering the optical properties of the heat spreaders, they must be transparent for the pump and the laser wavelength with low absorption and low optical birefringence. In the ideal case, the heat spreaders should at the same time, exhibit a high thermal conductivity, but these are not available at a lower price. In more simple terms, the heat spreader price among sapphire with a thermal conductivity of $k_{\text{Sapphire}} \sim (30\ldots46)$ W/m·K [68], and undoped, silicon carbide (4H-SiC) [69, 70] with $k_{\text{SiC}} \sim$490 W/m·K, and single-crystal synthetic diamonds [71–73] with $k_{\text{Diamond}} \sim 2000$ W/m·K, currently scales with the thermal conductivity value. According to current average market price, the cost of a 4×4 mm^2 sapphire piece is

$\sim$ 0.4 EUR. The price for SiC is $\sim$ 7 EUR, and diamond $\sim$ 1000 EUR. However, the better thermal management in a MECSEL allows to use the more cost-effective sapphire or SiC as heat spreaders. Both, sapphire and SiC are commercially available in wafer-quality. This allows to wafer-bond the heat spreaders and the gain medium which makes the fabrication of MECSELs suitable for low-cost mass production. Also, sapphire has a better optical quality than SiC with less birefringence.

2.4.3 Heat transfer simulation

To see the limits of thermal management using sapphire, SiC, and diamond, the temperature rise within the gain membrane is simulated in Chapter 4 and 5.1.6. Here, the simulations are based on Fourier's heat equation

$$\underbrace{\rho \cdot c_p \frac{\partial T(r,z,t)}{\partial t}}_{=0 \text{ (steady-state)}} - \nabla (k \cdot \nabla T(r,z,t)) = Q(r,z), \tag{2.2}$$

which describes how heat diffuses through a medium. ρ denotes the mass density, c_p the specific heat capacity, k the thermal conductivity, T the temperature at any time t and any radial coordinate r and axial coordinate z, and $Q(r,z)$ the generated heat energy. Since we only consider the temperature rise at a steady-state, the first term with the time-dependency in Eq. 2.2 can be neglected. The temperature rise is given by the thermal conductivity as the only material parameter, and the generated heat energy. The finite-element method (FEM) in COMSOL Multiphysics® was used in this thesis to solve the heat equation.

2.5 Integrated gain bandwidth

In semiconductor disk lasers, the effective gain, which is in particular relevant for the power performance and wavelength tuning range, basically depends on the spatial and spectral overlap between the QWs (or QD layers) and the electric standing wave field formed within the laser cavity. To maximize the output power, most of the gain structures possess an RPG structure, where the QWs (or QD layers) are optimized for a specific wavelength and arranged at the field antinodes. If one considers that the field nodes are located at the end mirrors, it should be noted that one

of the field nodes is fixed in position by the DBR in a VECSEL, which means that the phase is fixed. For a wavelength, which is slightly different than the structure has been previously designed for, the resonances become misaligned to the QWs (or QD layers), especially if the gain region is relatively thick. Since the phase is fixed, the overlap becomes smaller the more different the wavelength becomes. To ensure sufficient gain for lasing, the wavelength cannot be much different. Hence, the DBR can limit the gain bandwidth in such a way.

In a MECSEL, the gain element can be moved freely within the laser cavity, and the resonances can be matched individually within a broader wavelength region. As proposed by Yang et al., the position of the gain element within the laser cavity can have impact on the integrated gain bandwidth. The integrated gain can be expressed as [38]

$$G(\lambda, z) = \int_0^L g(\lambda, z' - z) \sin^2\left[\frac{\pi m(\lambda) z'}{L}\right] dz'. \tag{2.3}$$

λ denotes the wavelength, z the nearest distance between the gain medium and the cavity node of the end mirror, L the cavity length, $m(\lambda) = 2L/\lambda$ the mode index. $g(\lambda, z' - z)$ corresponds to the longitudinal gain profile for one gain layer per period and is expressed as

$$g(\lambda, z' - z) = G_0(\lambda) \sum_{l=1}^{N} \delta\left[z - \frac{(l-1)\lambda_0}{2}\right], \tag{2.4}$$

for a N-QW periodic gain structure and a structure design wavelength of λ_0. $\delta(z)$ denotes the Dirac delta function. $G_0(\lambda)$ describes the integrated gain for a single QW and is considered as a constant due to the flat MQW gain distribution. The calculation of Eq. 2.3 with Eq. 2.4 and an approximation of $\lambda_0/\lambda \approx 1$, yields

$$G(\lambda, z) \approx \frac{N}{2} G_0 [1 + \mathrm{sinc}(N\pi\epsilon) \cos[(N - 1 + M)\pi\epsilon]]. \tag{2.5}$$

$\epsilon = (\lambda - \lambda_0)/\lambda_0$ corresponds to the normalized detuning, and $M = 4z/\lambda_0$ the displacement of the gain structure from the end mirror.

Fig. 2.7 shows the gain factor G/G_0 plotted in the wavelength domain for a gain structure with twelve QWs for a design wavelength of 1.05 µm.

The FWHM integrated gain bandwidth is mainly given by the sinc-envelope term and the cosine modulation term. If the QWs are close to the cavity node (which

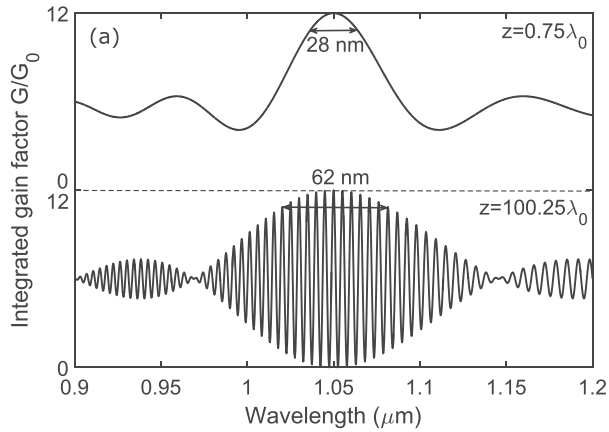

Figure 2.7 Integrated gain factor for a gain structure with twelve QWs for z = 0.75 λ_0 and z = 100.25 λ_0 at λ_0 = 1.05 µm [38]. The bandwidth at 90% of the maximum integrated gain is for small distances about 28 nm. For larger distances, the fast modulation term enlargens the bandwidth to about 62 nm.

describes the scenario in a VECSEL with the gain region next to the DBR), a bandwidth of about $\Delta\lambda = \lambda_0/2N$ results. For larger distances z the modulation becomes finer, which increases the bandwidth by a factor of two. It also has to be noted here, that the bandwidth gets broader with a smaller number of QWs. This could be a reason why rather thin gain structures are applied for mode-locking [74], and also explain why certain QD-based VECSELs besides the potentially wider gain bandwidth of the QD ensemble, have a larger tuning range than QW-based VECSELs with a thicker gain structure at the same wavelength region [75]. The integrated gain bandwidth can be increased by incorporating more than one QW per period at the expense of the maximum value of the integrated gain.

As can be seen from the above analysis in Fig. 2.7, the gain bandwidth is indeed increased with the larger distances of the gain element to the nodes in a MECSEL. However, there is a discrete set of allowed longitudinal modes in case of a standing electric wave field. If one assumes that ϵ in Eq. 2.5 can be expressed as $\epsilon = (m_0 - m)/m_0$, with $m = 2L/\lambda$ the longitudinal mode index, and $m_0 = 2L/\lambda_0$, the position-dependent phase term $M\pi\epsilon$ corresponds to

$$M\pi\epsilon = \frac{2\pi(m - m_0)}{L} \cdot z \tag{2.6}$$

as a finite set of numbers. By considering this position dependent phase term, the calculated gain bandwidth is plotted near the design wavelength $\lambda_0 = 1.05\,\mu m$ for different positions z in Fig. 2.8. As can be seen, every p-th longitudinal mode experiences the maximum gain for distances of $z = L/p$ as it is shown for $p = 2$ (when the gain element is exactly at the center of the cavity) and $p = 10$. The wavelength will be not continuously tunable. But the longitudinal mode spacings are so small (here below $\pm 0.1\,nm$ which is less than the FSR of the intra cavity heat spreaders) and therefore not remarkable in the measurements in this work.

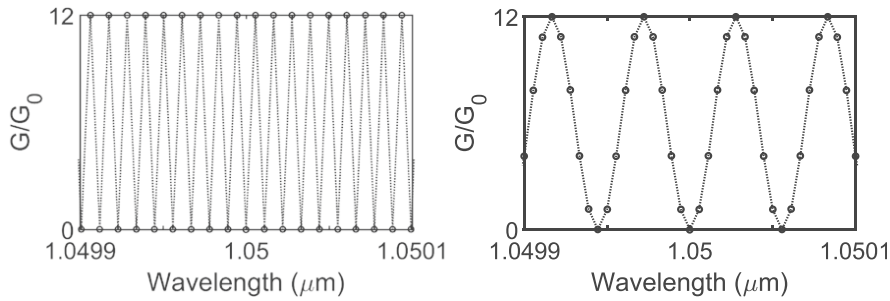

Figure 2.8 Calculated integrated gain near λ_0 = 1.05 µm for (a) z = L/2 and (b) z = L/10 [38]. The circles indicate the allowed longitudinal modes while the dashed lines are a guide for the eye.

3 EXPERIMENTAL METHODS

This chapter outlines the development methods starting from growth of the MECSEL structure. It follows a set of pre-characterizations, such as photoluminescence, and Omega/2Theta-measurements using X-ray diffraction to examine the crystal quality of the MECSEL structure. Scanning electron microscopy is used to check to layer thicknesses. Finally, one of the crucial steps how the substrate is removed wet-chemically is explained here in this chapter.

3.1 Material system

The AlGaInP and the GaInAsP material systems are used in this thesis to fabricate near infra red emitting MECSEL gain structures. The band gap energy with the corresponding wavelength can be traced over the lattice constant in Fig. 3.1 at 300 K.

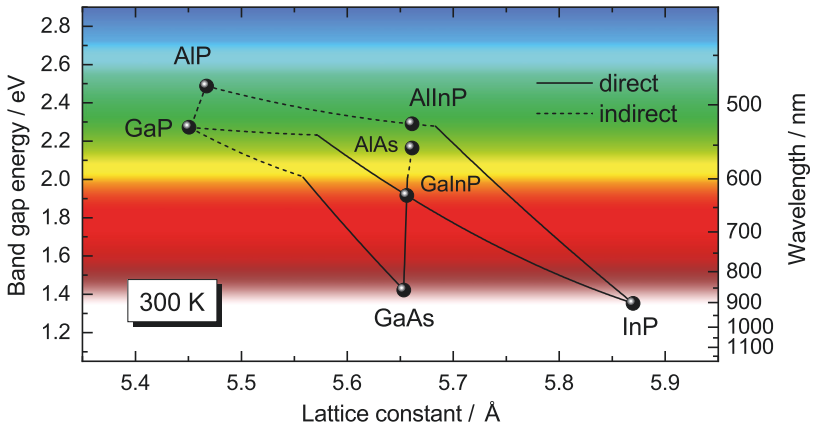

Figure 3.1 Band gap energy with the corresponding wavelength plotted over the lattice constant of the AlGaInP and GaInAsP material systems at 300 K. Direct and indirect band transitions are shown as solid lines and dots, respectively.

For an emission around 760 nm and 780 nm, the MECSEL gain regions in Chapter 5

are fully made of AlGaAs material compounds. As is evident in Fig. 3.1, AlGaAs can be grown without a large lattice mismatch to a GaAs substrate, which is a benefit in terms of practicability. This ternary compound can be expressed in more detail as $Al_xGa_{1-x}As$ with the aluminum mole fraction x. Only by changing the ratio between aluminum and gallium, the band gap can be modified, yet the lattice constant remains nearly unaffected [76]. While AlGaAs QWs have an aluminum fraction of less than $x = 0.12$ only, a higher fractional amount of aluminum in AlGaAs reveals a higher band gap as can be seen in Fig. 3.1 [77]. Thus, cladding layers are made of a higher aluminum mole fraction ($x > 0.49$) than barrier layers ($x \sim 0.4$). In addition, the charge carrier diffusion length and life time increase drastically as the aluminum mole fraction approaches $x \sim 0.4$, which is very close to the point where AlGaAs becomes an indirect semiconductor [78, 79]. However, the incorporation of the highly reactive aluminum in the QWs would generally support the oxygen contamination within the structure [80]. Subsequently, structures made of AlGaAs therefore suffer from degradation and a reduced device life time [81]. For this reason, aluminum is typically not used in the gain regions.

The quarternary material system, $Ga_xIn_{1-x}As_yP_{1-y}$ [82–84] is less susceptible to growth-related defects than AlGaAs. A better reliability in device lifetime can be provided [81, 85–88] which has been tested in long-term measurements of over 30 000 hours in 808 nm emitting laser diodes [89]. It has also been demonstrated that the use of GaInAsP in QWs with GaInP barriers/claddings has lead to a reduced surface recombination velocity and the facet temperature rise, which is about an order of magnitude smaller than in AlGaAs laser diodes [90]. To benefit from this Al-free material system, the MECSEL gain regions emitting around 800 nm- and 825 nm- consist of GaInAsP QWs, surrounded by GaInP barriers. The GaInAsP QWs are compressively strained which splits the heavy-hole and light-hole bands such that the heavy-hole band moves above the light-hole band. In such a valence band configuration, lasing in the TE polarization is generally favored rather than in the TM polarization [87]. A benefit from valence band splitting is that the interband transitions become more effective, leading to a lower laser threshold. To compensate for the overall strain within the structure, the $Ga_xIn_{1-x}P$ barriers are slightly tensile strained, with a gallium mole fraction of $x = 0.52$. Moving to 1.5 µm, the gain structures are made of InAs/InP QDs. 2.5 InAs monolayers are deposited on a $Ga_{0.2}In_{0.8}As_{0.435}P_{0.565}$ alloy, which has a band gap of about 1.18 µm and is nearly

lattice-matched to InP. The formation of the InAs islands occurs spontaneously via the Stranski-Krastanov growth mode. By capping the InAs islands with a thin InP layer, and subsequently by GaInAsP with a growth interrupt for an As/P exchange between these two steps, transforms the InAs islands into QDs [91]. A more detailed information about the growth can be found in [92].

3.2 Molecular beam epitaxy

Metal organic chemical vapor phase epitaxy (MOVPE) or molecular beam epitaxy (MBE) are common methods to grow thin film laser gain structures layer by layer up to an atomic scale. The gain structures in this work are fabricated on either an undoped GaAs (100) $\pm$ 0.5° substrate or on an InP (311)B substrate by gas-source MBE. The substrate diameter corresponds to 50.8 mm. Growth takes place in an ultra-high-vacuum environment and at temperatures of between 500 °C and 650 °C. As shown in Fig. 3.2, cracker effusion cells in the MBE chamber contain arsine AsH_3 and solid phosphorus as primary sources for diarsene As_2 and diphosphorus P_2.

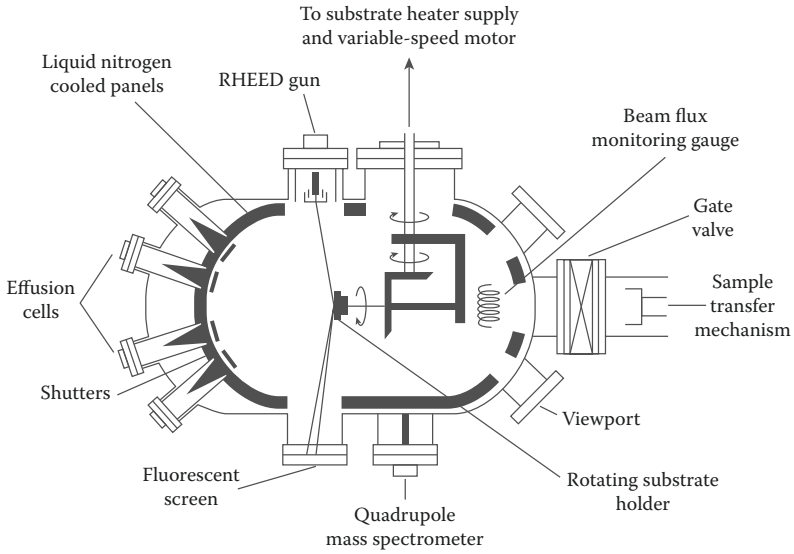

Figure 3.2 Schematic drawing of an MBE chamber [93]. As_2, P_2 provided from the primary sources AsH_3 and PH_3, diffuse as a beam as like Ga, In, and Al onto the substrate at the center of the MBE chamber. RHEED can be performed for an in-situ crystal quality check.

Solid elemental sources Ga, In, and Al are incorporated and heated up in the effusion cells until the sublimation point is reached.
The effusion cells are pointed towards the substrate located in the center of the MBE chamber. By opening the shutters, the atoms or molecules are released as a beam flux and deposited onto the substrate. For a more homogeneous growth, the substrate can be rotated. Furthermore, the substrate is heated up such that the atoms or molecules adsorbed on the substrate have a sufficient high mobility to move and find a proper growth site. Besides beam flux, vacuum chamber temperature, the substrate temperature is a relevant parameter, which affects the incorporation efficiency of the individual elements, and thus the resulting material composition [94]. Reflection high-energy electron diffraction (RHEED) can be performed in-situ to check the crystal quality during the growth. Here, electrons are released from the RHEED gun, and directed onto the sample surface at a small angle. The electrons get diffracted, which yields a diffraction pattern that can be monitored in the fluorescent screen. By this, an assessment of the surface quality of the deposited layer as well as the layer thickness can be made.

3.3 Structure pre-characterization methods after growth

X-ray diffraction

One of the pre-characterization methods after growth is X-ray diffraction (XRD). Here, a Philips X'pert PRO diffractometer is used to quantify several crystalline structural properties, such as material composition, crystal defects, strain, and crystal orientations. Basically, a monochromatic X-ray beam gets scattered under certain incident angles from each lattice planes of the sample. If the scattering process satisfies the Bragg condition, constructive interference occurs, which reveals a maximum in the measured spectrum. With the knowledge of the lattice parameters, as well as the relationship between lattice constant and material composition known as Vegard's law, the structural properties of the samples can be extracted.

Scanning electron microscpy

A common way to check the layer thickness and also the surface quality with a resolution down to the nanometer scale is scanning electron microscopy (SEM) [95]. Here, an electron beam is used to scan over the sample surface. If the electrons strike onto the sample, they are able to penetrate up to a few micrometers into the sample before they interact with the specimen atoms and create signals for the SEM images. Primarily, inelastic scattering leads to the ionization of the specimen atoms which releases a signal of secondary electrons. Due to their small energy around 3-5 eV, secondary electrons are used for topographical imaging to resolve structures down to an order of 10 nm. Elastic scattering generates back scattered electrons. As they have a higher energy around 50 eV, it prevents them from being absorbed over a larger lateral range. Thus, images can be taken more deep beneath the surface but with a reduced contrast compared with secondary electrons. Figure 3.3 shows a cross-section view of a MECSEL structure with a design wavelength of 800 nm taken with an SEM measurement in the back scattered electrons scanning mode. Visible are the four QW packages as slightly brighter stripes. The thickness of the gain region can be determined as ~ 550 nm, and of the bright AlAs process layer on top of the substrate as ~ 110 nm. The purpose of the process layer will be explained in more detail in Sec. 3.5.

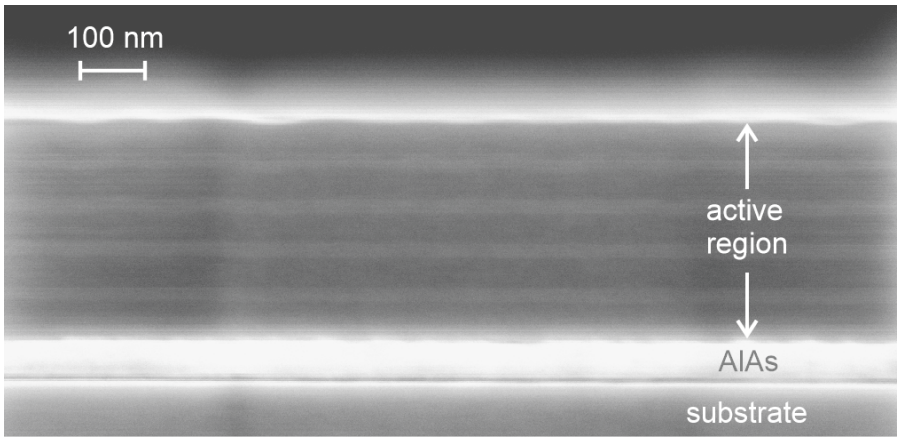

Figure 3.3 SEM image of an as-grown GaInAsP MECSEL structure from Chap. 4 and P4, for an emission around 800 nm taken with the back scattered electron signal. The 4×3 QWs in the gain region with a total thickness of $\sim$ 550 nm are illustrated as white stripes. The AlAs process layer is about 112 nm thick.

Photoluminescence

As a rough pre-check of the emission properties, PL measurements are performed on the as-grown samples. Here, a PL mapping system Accent RPM 2000 is used to examine the PL.

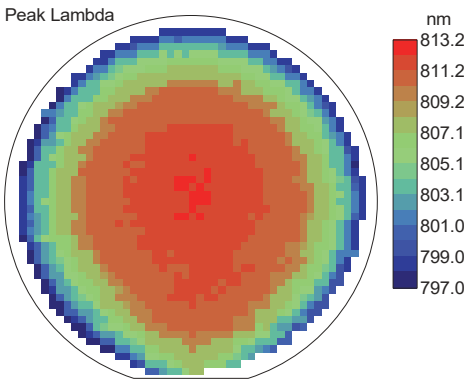

(a) Peak emission wavelength. The plot reveals a spectral shift from ∼ 813 nm towards slightly shorter wavelengths of ∼ 800 nm from the wafer center to the wafer edge.

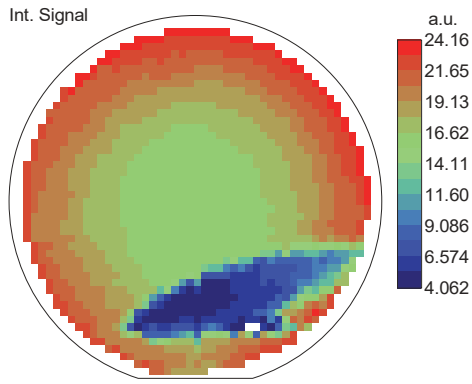

(b) PL intensity. By neglecting measurement on the wafer edges, the plot reveals a high-PL intensity area in the center of the wafer while the right-bottom area has a lower PL-intensity.

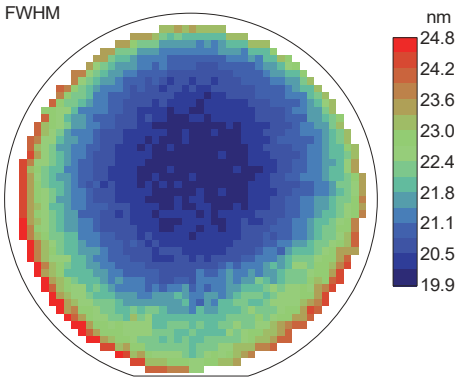

(c) FWHM of the PL signal.

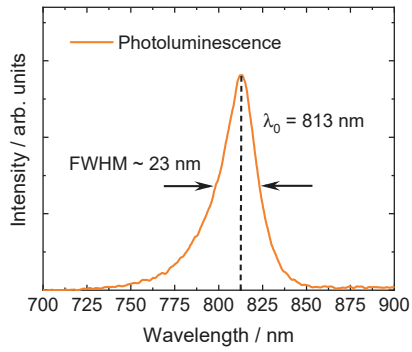

(d) PL measured at 50 mW pump power. The PL with a FWHM ∼ 23 nm has a maximum at ∼ 813 nm.

Figure 3.4 PL measurement performed for the 825 nm GaInAsP MECSEL structure from Chap. 6 and P2, at room temperature with (a)-(c) a PL mapping system Accent RPM 2000 across the whole wafer, and (d) at a separate vertical PL setup where the pump power is manually adjustable. The pump wavelength in both type of measurements is 532 nm.

With this PL mapping system, a distribution of the PL maximum, the intensity, and the FWHM can be measured over the whole wafer with an excitation wavelength of

532 nm as exemplarily shown for the 825 nm MECSEL structure in Fig. 3.4a-3.4c. Alternatively, the PL is investigated manually in a separate setup where the power of the excitation laser can be controlled and set each time a sample is characterized. For comparison purposes among different samples, this method is more precise than using the PL mapping system as the laser driving voltage varies after each measurement session. With an excitation wavelength of either 520 nm from a Nichia NDG7K75T laser diode, or 532 nm from a Coherent Verdi V-18 laser, the excitation beam is focussed under an angle of roughly 45° onto the sample surface. The PL signal is collected by a BLUE-Wave Miniature Spectrometer from StellarNet Inc. For the as-grown 825 nm MECSEL structure, the measured PL signal is plotted in Fig. 3.4d. The PL maximum at $\sim$ 813 nm, and a FWHM of $\sim$ 23 nm in Fig. 3.4 reveals that the results from both measurement methods agree well with each other.

3.4 Assessment of the heat spreader optical quality

Sapphire and SiC are used as a heat spreader material in this work. These are diced from 2 inch and 3 inch diameter wafers by a Disco dicing saw into square pieces with lengths of around 6-10 mm. Besides having smooth edges on the heat spreader pieces, a flat surface, and surface parallelism, the optical birefringence needs to be as low as possible. Otherwise, high birefringence could distort the MECSEL intra cavity beam during operation, leading to optical losses and poor laser performance. Before processing, a pre-check is performed whether optical birefringence is present. A common method is cross-polarization. Here, the heat spreaders are illuminated from the bottom by a linearly polarized white light source. A linear polarizer is positioned between the heat spreader and the camera. If birefringence is present, it is visible by a color pattern on the heat spreader as the refractive index distribution across the heat spreader piece is not homogeneous.

3.5 Processing

To remove the substrate from the as-grown sample, the sample is first bonded onto a carrier substrate which is the heat spreader piece itself. The heat spreaders have a squared area, ranging from $6\times6\,\mathrm{mm}^2$ to $10\times10\,\mathrm{mm}^2$. Before bonding, the surfaces are first cleaned with acetone and then with isopropyl alcohol in an ultrasonic cleaner for about ten minutes in each cleaning step. Afterwards, wet-chemical etching is applied. By immersing the sample into a liquid etching solution, this solution in the ideal case should etch away the substrate layer smoothly, at a reasonable high etch rate, and with a high selectivity of $>$ 100:1. In this case, there is principally no need of an etch stop layer inbetween. A process layer could further improve the surface quality from the etching. If typical etching solutions reveal a small selectivity between the substrate and the laser-active materials, meaning the solutions etch both materials at similar high etch rates, an etch stop layer is usually introduced inbetween.

GaAs substrate wet-chemical process

For MECSEL structures grown on GaAs substrates presented in chapters 4-6 as well as P1, P2, and P4, the process layer is made of AlAs and has a thickness between 100 nm and 200 nm. This enables the use of ammonium hydroxide - hydrogen peroxide (NH_4OH:H_2O_2) as an etchant with a mixing ratio of 1:3 [96, 97]. After dipping the sample into the etchant for 45 ± 5 min, the substrate removal step is completed. This is recognizable by a slight color transition. Still, the membrane surface within the solution is not glossy enough as like a mirror surface but covered by a thin murky film which is most likely residual of the AlAs or GaAs layer. Subsequently, the sample is immersed to diluted hydrofluoric acid (0.5% HF) for about ten seconds. This HF solution is supposed to highly react with layers with a high aluminum content only. Therefore, the gain region surrounded by nearly HF-resistive GaInP capping and AlGaInP window layers with an Al content below 30%, is protected. A top view optical microscope image of the membrane surface after the substrate removal process is shown in Fig. 3.5a. As can be seen, the image reveals a smooth, brilliant, mirror-like surface. Finally, a second heat spreader piece is bonded on top of the membrane. A microscope image surface-view is illustrated in Fig. 3.5b. The used

etching solutions with the total etch time in this work are summarized in Tab. 3.1.

Etch material	Layer thickness	Etching solution	Etch time
GaAs substrate	$\sim 500\,\mu m$	$NH_4OH{:}H_2O_2$ (1:3)	45 ± 5 min
AlAs	(100-150) nm	0.5% HF	10 s

Table 3.1 Etching solutions for GaAs substrates with an AlAs process layer used for the wet-chemical process in this work.

Debonding can take place during laser operation, especially when pumping the gain membrane at too high pump power intensities. Fig. 3.5c and 3.5d examplarily show a surface-view of a debonded and cracked gain membrane.

(a) Bare semiconductor membrane after the substrate-removal, single-side bonded onto SiC.

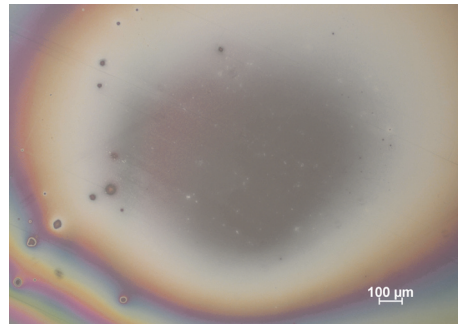

(b) Semiconductor membrane with a SiC heat spreader bonded on top of the surface.

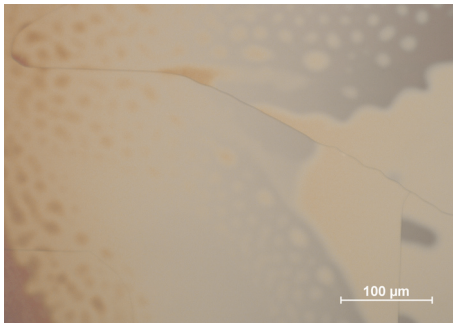

(c) Debonded and cracked gain membrane between two SiC heat spreaders after laser operation.

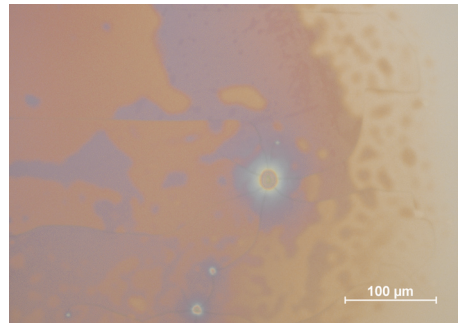

(d) The position of debonding can be seen by the circular spot originating from a Gaussian pump beam.

Figure 3.5 Microscope images of the semiconductor structure from a Nikon Eclipse optical microscope.

InP substrate mechanical polishing and wet-chemical process

In the following, the mechanical polishing and wet-chemical processes applied for the MECSEL structure grown on InP substrates from chapter 7 and P3 are explained. An InGaAs etch stop layer of 100 nm thickness separates the gain region and the InP substrate. This allows to utilize a hydrochloric acid solution (30% HCl:H_2O with a mixing ratio of 5:1) to remove the InP substrate [98]. The etchant is suitable for this process, since it has a selectivity ratio of up to 500 between InP and InGaAs. Although the etch rate at room temperature is as high as $\sim 15\,\mu m$ while the InP substrate thickness is here about $\sim 300\,\mu m$, the chemical reaction between HCl and InP leads to the formation of PH_3 bubbles [99]. The bubbles accumulate on the substrate surface which prevents the chemical etching. For a more uniform etching, the etch time should be kept as short as possible.
Hence, the substrate is mechanically thinned down to a thickness of $\sim$60-80 µm before wet-chemical etching. A Logitech Lapping System PM5 is utilized where the etch rate can be adjusted by the rotation speed and pressure. For InP, sapphire polishing powder with a grain size of 9 µm in diameter is applied.
After mechanical thinning is completed, the sample is held in the HCl solution in such a way that the bubbles formed by the chemical reaction with InP can move upwards to the top surface. Thus, the substrate surface is pointing vertically to the top, and the solution is stirred with a magnetic stirrer at a rotation speed of $\sim$ 300-400 RPM. With this method, the residual InP substrate is removed within $\sim$ 4-5 minutes. This step is completed, as soon as the sample surface becomes brilliant similar to a mirror surface. To remove the InGaAs etch stop layer, the sample is immersed into a phosphoric acid-hydrogen peroxide solution H_3PO_4:H_2O_2:H_2O, with a mixing ratio of 1:1:8 for about one minute [100].

Etch material	Layer thickness	Etching solution	Etch time
InP substrate	$65 \pm 15\,\mu m$	HCl:H_2O (5:1)	4 ± 1 min
InGaAs	~ 100 nm	H_3PO_4:H_2O_2:H_2O (1:1:8)	~ 1 min

Table 3.2 Etching solutions for InP substrates with an InGaAs etch stop layer used in this work. Before wet-chemical etching, the InP substrate is mechanically polished down to a thickness of $65 \pm 15\,\mu m$.

4 SIMULATION OF THERMAL BEHAVIOR

Like in all lasers, optical pumping is associated with heat generation in the gain region. Owing to the quantum defect, a fraction of about 20% to 40% of the pump energy from barrier pumping remains as heat in the semiconductor crystal lattice, leading to a temperature rise. Up to a certain pump power limit, heat can be sufficiently dissipated from the gain region. Hereby, the conversion of the absorbed pump power to lasing power occurs nearly linearly. When exceeding the critical limit, a higher pump power does not further increase the output power but only creates too much heat in the gain region. The conversion efficiency drops until the laser finally shuts off. This effect in the semiconductor disk laser literature is commonly called "thermal-rollover".

In order to push the semiconductor disk laser technology further to higher output power operation, several heat extraction strategies from the thin device or flip-chip approach [67] to the intra cavity heat spreader approach [16] have been developed, simulated [12, 101] and implemented until the MECSEL concept to cool the gain region from both sides has emerged [28, 29, 34, 35].

In this chapter, thermal simulations for a MECSEL at various cooling and pumping conditions are conducted which was submitted as P4. The temperature increase of the gain membrane is investigated for different heat spreader materials, such as sapphire, SiC, and diamond at varying thicknesses. To explore the potential of power scaling, the simulations, conducted via the finite-element method (FEM) includes various pump beam diameters and pump beam profiles. The simulations are based on experimental results and are also compared with experimental results from the literature.

4.1 Finite-element modeling

For thermal modeling, the finite-element method (FEM) in COMSOL Multiphysics® was applied. The amount and size of the meshes were individually adjusted to the gain membrane and the heat spreaders regions as illustrated in Fig. 4.1. As can be seen, the simulation was simplified by making use of the rotational symmetry. Thus, the simulations were conducted in the cylindrical coordinate system with the radial coordinate r and the axial coordinate z. A rectangular excerpt as shown in Fig. 4.1 with the gain membrane at $z = 0$ surrounded by two SiC heat spreaders was considered from the radial center $r = 0$ to $r = 0.75\,\mathrm{mm}$. Thus, the radius of the excerpt was about five times larger than the pump beam diameter as used in the experiments.

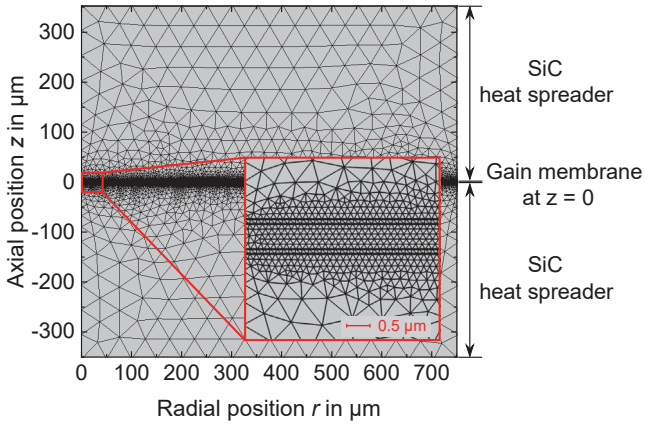

Figure 4.1 FEM mesh for the MECSEL gain sandwich. A gain membrane is sandwiched by two 350 µm SiC heat spreaders with a bonding layer inbetween.

Furthermore, the individual QWs, barrier, and cladding layers were not separately implemented. Since the major component of the gain membrane (see Sec. 4.2) was made of barrier/cladding layer material, the gain membrane was approximated by a single layer of a thickness z_0 with a thermal conductivity of the barrier/cladding material. For further simplicity, the indium foil and the heat sink mount were neglected in the simulations. Thermal insulation was taken into consideration at the outer surfaces from the top and bottom of the heat spreaders. The outer surface at $r = 0.75\,\mathrm{mm}$ was fixed to the heat sink temperature of 20°C. As an initial starting

condition for the temperature was set to 20°C. Thermal radiation and convection were neglected.

To obtain the temperature distribution within the gain membrane sandwich, Fourier heat equation (see Eq. 2.2) was solved with the FEM using COMSOL Multiphysics®. The thermal conductivity k can vary along the radial and the axial axis. However, this anisotropy aspect makes a difference of about 2% in VECSELs according to the simulations of Kemp et al. [12] and was therefore neglected in the simulations.

According to the experiments, a pump beam with a Gaussian beam profile was considered as a heat source. The heat load originating from the quantum defect can be expressed as

$$Q_{\text{Gauss}}(r,z) = \frac{2\cdot\eta_{\text{Q}}\cdot P_0}{\pi w^2}\cdot\alpha\cdot\exp\left(-\frac{2r^2}{w^2}-\alpha(z_0-z)\right), \tag{4.1}$$

where P_0 denotes the pump power that reaches the gain region, w the $1/e^2$ pump beam diameter, and α the pump absorption coefficient. The quantum defect η_{Q} was calculated as $\eta_{\text{Q}} = 1-\lambda_{\text{P}}/\lambda_{\text{MECSEL}}$ by the pump wavelength λ_{P} and the MECSEL emission wavelength λ_{MECSEL}. Additional heating effects from non-radiative processes were not included.

4.2 Simulation parameters

The simulations were based on a 550 nm-thick MECSEL gain membrane emitting at 800 nm. The gain membrane incorporated twelve GaInAsP QWs in gaps of three QWs in each QW package, GaInP barriers/claddings, and 20 nm thick AlGaInP window layers. The gain membrane consisted of 80% GaInP. For simplification, the gain membrane was described by a single bulk layer made of $Ga_{0.48}In_{0.52}P$ barriers/claddings. As the thermal conductivity is inversely proportional to the thermal resistivity, the Vegard's law for the thermal resistivity was used to calculate the thermal conductivity of GaInP. With the thermal conductivity $k_{\text{GaP}} = 77\,\text{W/m·K}$ of GaP, $k_{\text{InP}} = 68\,\text{W/m·K}$ of InP, and the bowing factor $C_{\text{GaInP}} = 1.4\,\text{W/m·K}$, the thermal conductivity for GaInP resulted as 5.2 W/m·K [102, 103]. The gain membrane was optically pumped by a 532 nm laser with a Gaussian beam profile. The pump absorption coefficient of the gain membrane was obtained by measuring the incident, reflected, and transmitted pump power. As the pump beam propagated through the

Table 4.1 Simulation parameters for the FEM thermal model

	Parameter of the gain membrane or pump	Value
z_0	Gain membrane thickness	550 nm
k_{GaInP}	Membrane thermal conductivity	5.2 W/m·K
α	Pump absorption coefficient	$5.7 \cdot 10^4$ cm^{-1}
$\lambda_{\mathrm{MECSEL}}$	MECSEL emission wavelength	800 nm
λ_{P}	Pump wavelength	532 nm
η_{Q}	Quantum defect	0.335
$d_{\mathrm{P}} = 2w$	Pump beam diameter	(50…500) µm
P_0	Pump power at $z = z_0$	(1…10) W
T_{hs}	Heat sink temperature	20°C
	Parameter of the heat spreaders	**Value**
k_{Sa}	Thermal conductivity of sapphire	(30…46) W/m·K [68]
k_{SiC}	Thermal conductivity of SiC	490 W/m·K [69, 70]
k_{D}	Thermal conductivity of diamond	2000 W/m·K [71]
	Parameter of the bonding layer	**Value**
k_{B}	Thermal conductivity	0.4 W/m·K
t_{B}	Thickness	100 nm

SiC heat spreaders, the measured value of $\alpha = 5.7 \cdot 10^4 \mathrm{cm}^{-1}$ included the absorption from the heat spreaders as well. This is justified because the absorption from SiC has been measured to be as small as 0.25 cm^{-1} [41]. With high optical quality sapphire, which typically does not have large absorption, a nearly identical value for α as like with SiC has been measured. Therefore, the simulations with SiC, sapphire, and diamond heat spreaders as well as with the super-Gaussian pump beam profile were carried out with the same pump absorption coefficients. Further simulation parameters of the gain membrane, pump and heat spreader properties are summarized in Tab. 4.1.

To verify the simulations, the thermal resistance of the MECSEL was determined by spectral shift measurements at a pump beam diameter of $d_{\mathrm{P}} = 180$ µm [104]. For the SiC-cooled MECSEL, the emission wavelength shifted at a rate of 0.85 nm/W with the dissipated power and at a rate of 0.20 nm/K with the heat sink temperature as il-

lustrated in Fig. 4.2a. The spectral shift with the heat sink temperature was measured at 5% duty cycle at $P_{abs} = 0.8\,\mathrm{W}$. Correspondingly, the thermal resistance resulted as $\sim 4.25\,\mathrm{K/W}$. This value enabled us to validate the FEM thermal model, which was used to simulate other heat spreader and pumping configurations. In addition, the thermal resistance of the MECSEL with sapphire heat spreaders was measured at a pump beam diameter of $d_P = 110\,\mu\mathrm{m}$ in Fig. 4.2b. The spectral shift with the dissipated power was about 6.45 nm/W. In contrast, the emission wavelength shifted with the heat sink temperature at a rate of $\sim 0.23\,\mathrm{nm/K}$, which should not depend on the heat spreader material and was close to the value measured with SiC.

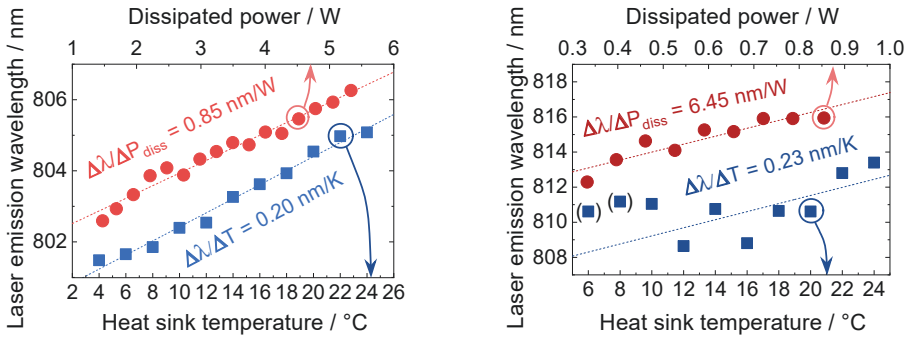

(a) SiC-cooled 800 nm MECSEL at $d_P = 180\,\mu\mathrm{m}$. The spectral shift with the heat sink temperature (blue squares) have been performed at 5% duty cycle at $P_{abs} = 3.4\,\mathrm{W}$. A thermal resistance of $R_{th} \sim 4.25\,\mathrm{K/W}$ can be calculated.

(b) Sapphire-cooled 800 nm MECSEL at $d_P = 110\,\mu\mathrm{m}$. The spectral shift with the heat sink temperature (blue squares) have been performed at 5% duty cycle at $P_{abs} = 0.8\,\mathrm{W}$. A thermal resistance of $R_{th} \sim 28\,\mathrm{K/W}$ can be calculated.

Figure 4.2 Spectral shift measurements with the dissipated power (red dots) and heat sink temperature (blue squares) of the 800 nm MECSEL. Measurements performed by Aaron Rogers.

In the thermal simulations, the highest temperature within the gain membrane was obtained for a pump power P_0 from 1 W to 10 W. The rate of temperature rise with the pump power was denoted as maximum temperature rise. Fig. 4.3a illustrates a temperature distribution cross-section view of the MECSEL gain sandwich at $P_0 = 6\,\mathrm{W}$. The maximum temperature at the center ($r = 0$) of the pump beam already was about 77.3°C, which exceeded the typical operation temperature of semiconductor lasers. Since no thermal-rollover was observed in the experiments and lasing under these pumping conditions was still possible, we did not only consider the maximum value near the center of the pump beam only but in a larger spatial region. The radial temperature average over the pump beam diameter was included to have more accurate comparison to the experimental results.

4.3 Relevance of the contact surfaces

For efficient heat dissipation, the gain membrane should be in the ideal case in close contact to the heat spreader surfaces. In reality, it is likely that the contact is neither perfectly smooth nor in direct contact. Between the surfaces an air gap or an liquid bonding layer can potentially hamper the heat flow as earlier described in VECSELs [12]. How such an imperfect contact, described as a bonding layer between the gain membrane and the heat spreaders, affects the heat flow in MECSELs is investigated in this section. Therefore, a bonding layer is included in the thermal model as shown in Fig. 4.3b.

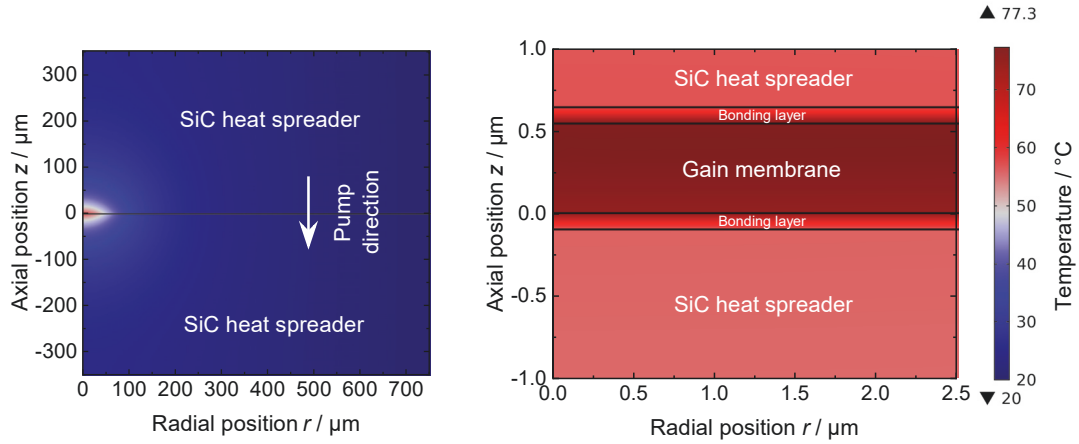

(a) Full cross-section view of the MECSEL gain sandwich. The temperature scale is the same as in Fig. 4.3b.

(b) Enlarged cross-section view. Visible is the gain membrane at $z = 0$ surrounded by a 100 nm thick bonding layer on each side.

Figure 4.3 FEM simulation of the 800 nm MECSEL with two 350 µm thick SiC heat spreaders cooled to a heat sink temperature of $T_{hs} = 20°C$. The gain membrane is optically pumped by a Gaussian pump beam from the positive z-direction. $P_0 = 6$ W reaches the gain membrane.

The bonding layer thickness and thermal conductivity were varied. Fig. 4.4a shows that an optimal contact without any bonding layer would lead to a temperature increase of 6.4 K/W when considering the maximum. At an optimal contact the radial average temperature rise would be as low as 4.2 K/W. Both, the maximum and radial average temperature increases linearly with the bonding layer thickness. The maximum temperature rises by 3 K/W per 100 nm, while the radial average temperature by 1.4 K/W. A conservative assumption was made for the thermal conductivity. A

thermal conductivity of $k_B = 0.4\,W/m{\cdot}K$ was assumed for the bonding layer, which was a slightly worse heat conductor than water ($k_{H_2O} = 0.6\,W/m{\cdot}K$).
To investigate the dependency on the thermal conductivity, a bonding layer thickness of 100 nm was assumed. 100 nm were chosen, as it corresponds to the upper limit where no interference of the visible light occurs. According to the thermal model, the temperature is inversely proportional to the thermal conductivity of the bonding layer as shown in Fig. 4.4b. At $\sim 2\,W/m{\cdot}K$, the rate of temperature increase reaches a saturation point. If the thermal conductivity is further increased to $10\,W/m{\cdot}K$ it does not further lower the maximum and the radial average temperature rise value, which remains at 7 K/W and 4.5 K/W, respectively.

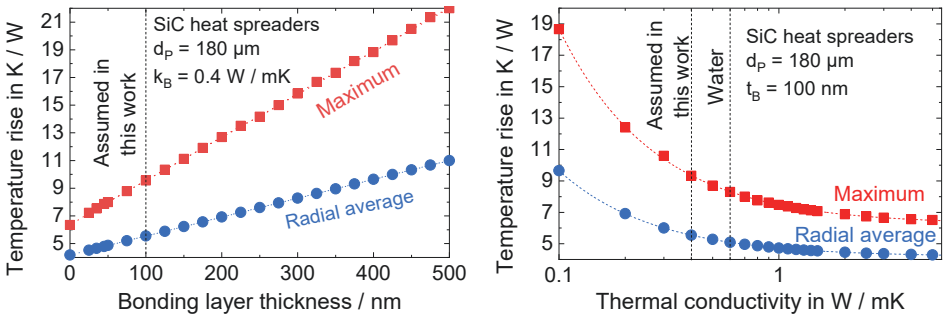

(a) Effect of the bonding layer thickness.

(b) Effect of the bonding layer thermal conductivity.

Figure 4.4 Relevance of the bonding layer property.

4.4 Heat spreader materials and configurations

4.4.1 Power scalability with various types of heat spreaders

In this section, the temperature increase was calculated from the FEM model for various types of heat spreader materials, such as SiC, sapphire, and diamond. This information can be used to estimate the lower limit of the heat spreader thickness that is necessary at pump beam diameters of 90 µm, 180 µm, 270 µm, and 360 µm.

1. For SiC, the simulations suggest that the temperature inversely decreases with the heat spreader thickness between 50 µm and 250 µm for all four pump diameters. This behavior can be seen in Fig. 4.5a and 4.5b. For heat spreaders thicker than 250 µm, the temperature does not change significantly. At this

point, it needs to be considered that thicker heat spreaders could induce higher optical losses without providing a significant thermal benefit as the intra cavity beam needs to propagate through a larger heat spreader volume. Furthermore, it has been found that the temperature rise at a pump diameter of $d_P = 180\,\mu m$ is nearly two times lower than with $d_P = 90\,\mu m$.

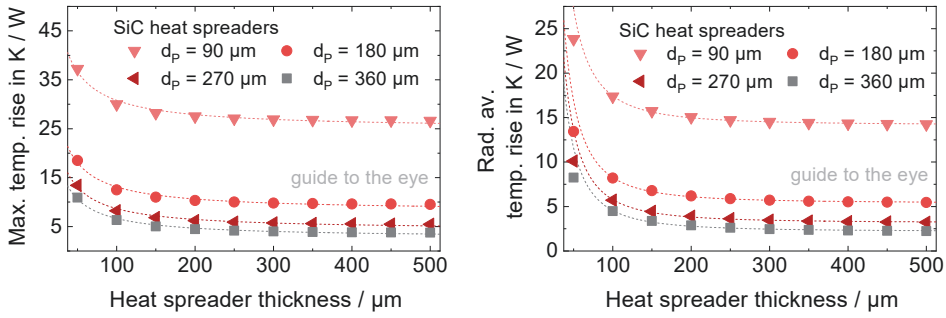

(a) Maximum temperature rise.

(b) Average over the pump beam diameter.

Figure 4.5 Temperature rise plotted over the heat spreader thickness for SiC at various d_P.

2. Compared with SiC, sapphire has an about ten times lower thermal conductivity. Thus, it needs to be considered that thermal roll-over sets in at a lower pump power. According to the experiments [105], thermal roll-over occurs at about $P_0 = 2$ and the temperature rise is simulated up to a pump power P_0 of 2 W at which the temperature to pump power behavior is still linear. In Fig. 4.6a and 4.6b the maximum and radial average temperature rise are plotted over the heat spreader thickness for all four pump beam diameters.

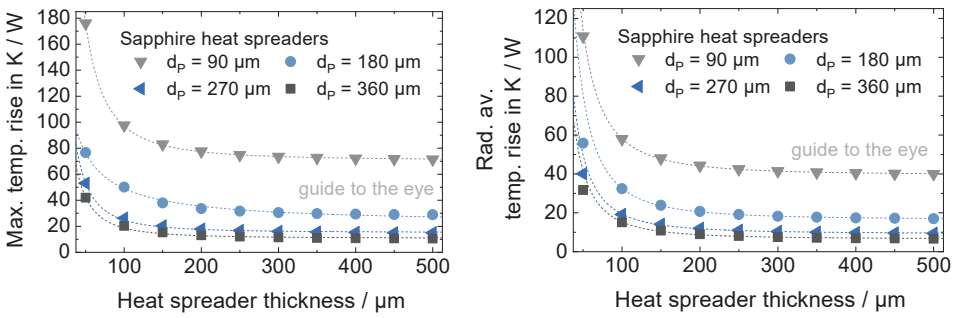

(a) Maximum temperature rise.

(b) Average over the pump beam diameter.

Figure 4.6 Temperature rise plotted over the heat spreader thickness for sapphire at various d_P.

The thermal model suggested a heat spreader thickness of about 300 µm for

all four cases. At low pump power, the MECSEL typically requires a smaller pump beam diameter near 90 µm to reach the laser threshold. For instance, the radially averaged temperature rise corresponds to 41 K/W at d_P with a 300 µm thick heat spreader. By this, we can estimate that the gain membrane heats up by $\sim 61.5°C$ at $P_0 = 1.5$ W.

3. As diamond is a good thermal conductor, the temperature rise of the gain membrane with diamond heat spreaders is not as large as with SiC or sapphire heat spreaders. Fig. 4.7a and 4.7b show the maximum and radial average temperature rise obtained from a thermal model of up to $P_0 = 10$ W. For heat spreader thicknesses larger than 150 µm, the thermal model suggests that the temperature increases by 1.7 K/W at $d_P = 180$ µm on radial average. For larger pump beam diameters of $d_P = 270$ µm and $d_P = 360$ µm, the temperature rise is found to be below 1 K/W.

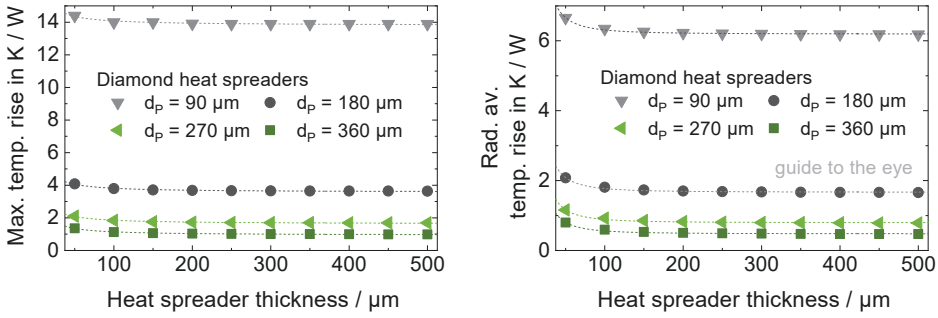

(a) Maximum temperature rise.

(b) Average over the pump beam diameter.

Figure 4.7 Temperature rise plotted over the heat spreader thickness for diamond at various d_P.

4.4.2 Significance of double-side cooling

The significance of double-side cooling (DSC) with diamond heat spreaders was proposed and simulated by Yang et al. [28]. Subsequently, an experimental investigation with SiC heat spreaders was demonstrated [41]. The DSC gain membrane could be optically pumped at twice pump power than a single-side cooled gain membrane. Consequently, the output power was about 2.5 times higher. As a further investigation, the temperature behavior for a single-side cooled (SSC) and DSC gain membrane was simulated for SiC, sapphire, and diamond in this section.

Fig. 4.8 shows a temperature distribution cross-section view of a single-side cooled gain membrane using a 350 µm SiC heat spreader. At P_0 =6 W, the maximum temperature was found to be 136°C. This is about two times higher than the DSC gain membrane in Fig. 4.3b with the same pump power applied.

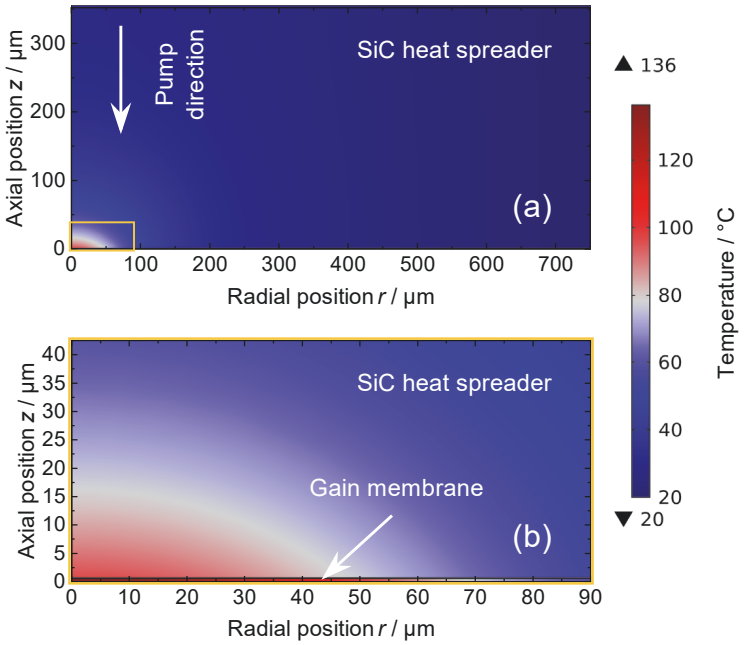

Figure 4.8 Cross-section view of a single-side cooled gain membrane. The gain membrane is positioned at z=0 and cooled to T_{hs}= 20 °C. Above the gain membrane is a 100 nm thick bonding layer and a 350 µm thick SiC heat spreader. The pump beam with P_0 = 6 W impinges from the positive z-direction onto the gain membrane. (a) illustrates the whole MECSEL gain element. (b) shows an enlarged view around the pump beam center and the gain membrane.

For a pump beam diameter of d_p = 180 µm the maximum and radial average temperature rise between SSC and DSC are compared in Fig. 4.9a and 4.9b for various heat spreader thicknesses from 50 µm to 500 µm. Also plotted along is the ratio between SSC to DSC. As can be seen, the temperature rise with DSC is about a factor two lower than with SSC. Thus, the simulations were in good agreement with the power scaling results that had been demonstrated by Yang et al. [41]. For diamond, the simulations as shown in Fig. 4.9e and 4.9f suggested a similar large benefit from DSC as for SiC. For other pump diameters d_p =90 µm, 270 µm, and 360 µm, the thermal improvement by DSC compared to SSC lies in the similar order of magnitude of about two. In contrast, the temperature in a sapphire-cooled gain membrane lowered by a

factor between three and four with DSC than with SSC as shown for a smaller pump diameter of d_P =90 µm in Fig. 4.9c and Fig. 4.6b. Most likely the benefit is larger at a smaller pump diameter because the thermal conductivity of sapphire is significantly lower than of SiC or diamond.

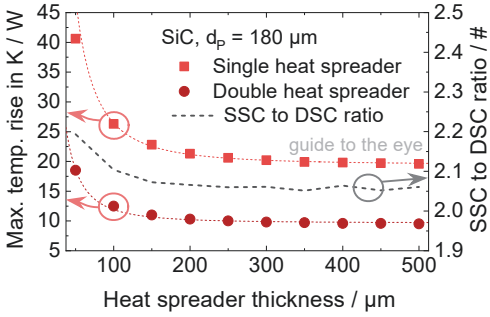

(a) Maximum temperature rise of the SSC and DSC gain membrane with diamond.

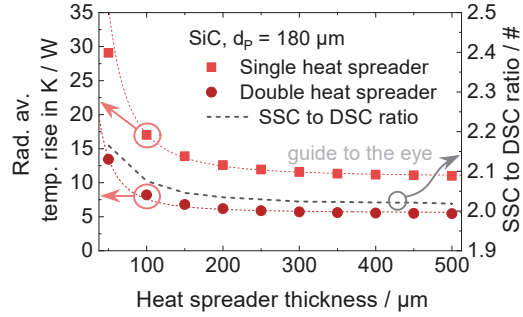

(b) Average temperature rise of the SSC and DSC gain membrane with SiC.

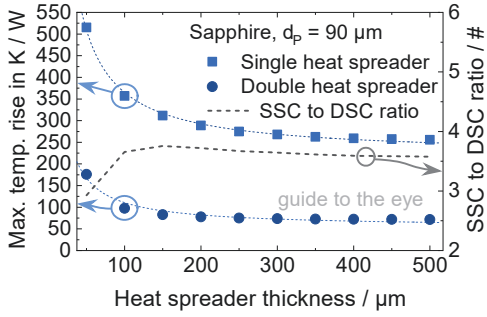

(c) Maximum temperature rise of the SSC and DSC gain membrane with sapphire.

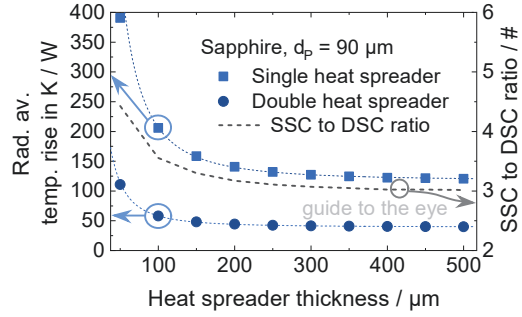

(d) Average temperature rise of the SSC and DSC gain membrane with sapphire.

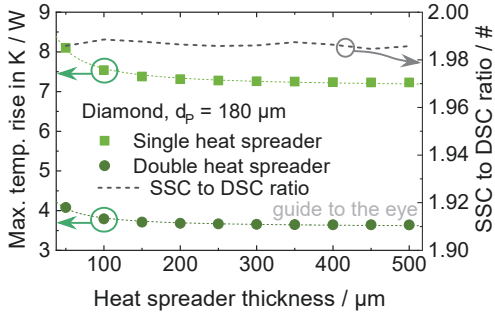

(e) Maximum temperature rise of the SSC and DSC gain membrane with diamond.

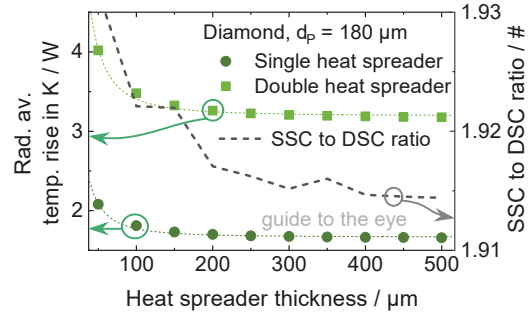

(f) Average temperature rise of the SSC and DSC gain membrane with diamond.

Figure 4.9 Comparison between SSC and DSC for various heat spreaders at varying thicknesses.

4.5 Relevance of the pumping conditions

4.5.1 Lateral power scaling

A common power scaling technique used in semiconductor disk lasers is to pump the gain membrane and distribute heat over a larger area. This technique can be applied as long as the heat flow out from the gain membrane mainly occurs in one dimension. Up to a certain pump beam radius, lateral heat flow from the center of the pump beam to the outer side is nearly negligible. Heat can be considered to flow parallel in axial direction to the heat spreaders. If the pump beam area is scaled up, the temperature increase per area can be lowered. By increasing the pump beam area, the three-dimensional heat flow behavior given by the heat spreader simultaneously becomes more significant to affect the temperature rise of the gain region. Thus, at larger pump beam diameters a further increase of the pump beam area does not necessarily reduce the incorporated heat within the gain region as it has been simulated by Maclean et al. [101] for VECSELs. In a similar manner, a limitation to the power scaling technique is given for MECSELs which is investigated in the following. The radial average temperature rise of the gain membrane was simulated for a set of heat spreaders in Fig. 4.10.

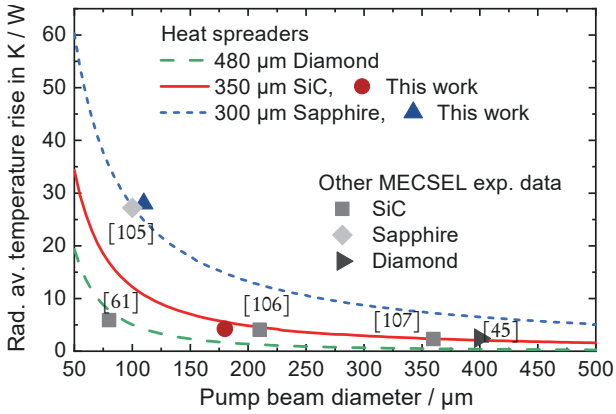

Figure 4.10 Radial average temperature rise plotted over the pump beam diameter for various heat spreaders. For comparison purposes, the thermal resistance of the 800 nm MECSEL in this work and of the previous reported MECSELs are included.

For power scalability and efficient laser operation, following two aspects were taken

into consideration. First, the laser threshold grows proportional to $1/w^2$ by assuming a circular pump beam area. Second, the temperature benefit provided by the larger pump beam area needs to scale down at least in a similar manner by $1/w^2$. The simulations in Fig. 4.10 points out that the $\Delta T/\Delta P \propto 1/w^2$ behavior holds true for SiC and diamond for a pump beam diameter up to 500 µm. However, for sapphire, the temperature dependency is rather closer to $\Delta T/\Delta P \propto 1/w$ than $1/w^2$. At about 110 µm, the temperature curve begins to stagnate. Power scaling has been suggested to become less efficient as soon as the pump beam diameter is larger than 110 µm.

In Fig. 4.11 the temperature contour plots are illustrated at a constant pump power density (PPD) of 23.6 kW/cm^2 and pump beam diameters from 90 µm to 360 µm. As can be seen, the SiC heat spreader temperature next to the gain membrane around the center of the pump beam with $d_\mathrm{P} = 90$ µm was about 40°C. The maximum and radial average gain membrane temperature corresponds to 58.9°C and 40.9°C, respectively. By increasing the pump beam diameter, not only the gain membrane itself but also the heat spreader gets hotter around the pumped region. For a pump beam diameter of $d_\mathrm{P} = 180$ µm, the heat spreader temperature close to the gain membrane (with $T_\mathrm{max} = 78$°C, $T_\mathrm{rad,\,av.} = 53.3$°C) increases to 60°C. The simulations suggest that the limit of power scaling is set by the heat spreaders itself, which are heating up at larger diameters as the radial heat flow becomes more significant.

To compare the simulations with the experiments, the SiC and sapphire thicknesses in Fig. 4.10 are the same as used in the experiments. The thermal resistance was determined by spectral shift measurements. For the SiC-cooled 800 nm MECSEL, the thermal resistance resulted as ~ 4.25 K/W at a pump beam diameter of 180 µm. At this pump beam diameter, lasing with sapphire cooling was not possible. A possible explanation is that the heat extraction does not allow operation with the higher lasing threshold, which is in accordance with our simulations. For this reason, the sapphire-cooled MECSEL was optically pumped at a smaller diameter of ~ 110 µm. A thermal resistance ~ 28 K/W was measured, which was in agreement with the simulations.

Additionally, the thermal resistances of previously demonstrated MECSELs at various wavelengths between 760 nm and 1.77 µm are plotted in Fig. 4.10. The measured thermal resistance of the 825 nm MECSEL [106] with GaInAsP QWs and GaInP barriers/claddings were in good agreement with the simulations, probably because

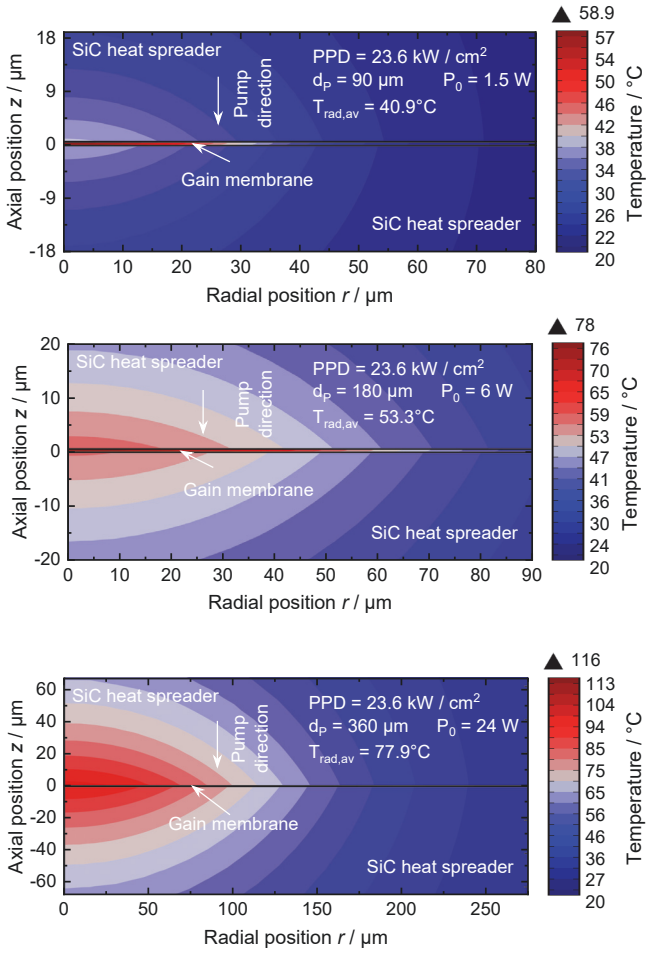

Figure 4.11 Temperature contour plots at various d_P and constant pump power density.

the gain membrane thickness, material composition, and pump absorption were very similar to the 800 nm MECSEL. Also, the thermal resistances of the sapphire-cooled 760 nm MECSEL made of AlGaAs [108], SiC-cooled 1.5 µm MECSEL with InAs/InP QDs [107], and diamond-cooled 1.77 µm MECSEL with InGaAlAs/InP QWs [45] were close to the simulated values. A larger difference can be seen in the 780 nm-emitting MECSEL with AlGaAs QWs [61]. With SiC heat spreaders, the thermal resistance was measured as 5.9 K/W while the simulations suggest a higher temperature increase of about $\sim$ 16.5 K/W. The smaller pump absorption coefficient and quantum defect can lead to a smaller temperature rise. Also, one would

expect a lower temperature increase if the gain membrane itself has a higher thermal conductivity. The simulations in Fig. 4.12a and 4.12b suggest for a SiC-cooled gain membrane that a larger thermal conductivity value of the gain membrane lowers the temperature to a certain limit. If the thermal conductivity is already higher than 5 W/m·K, a further increase does not lead to a significantly lower temperature at a pump beam diameter of 180 µm.

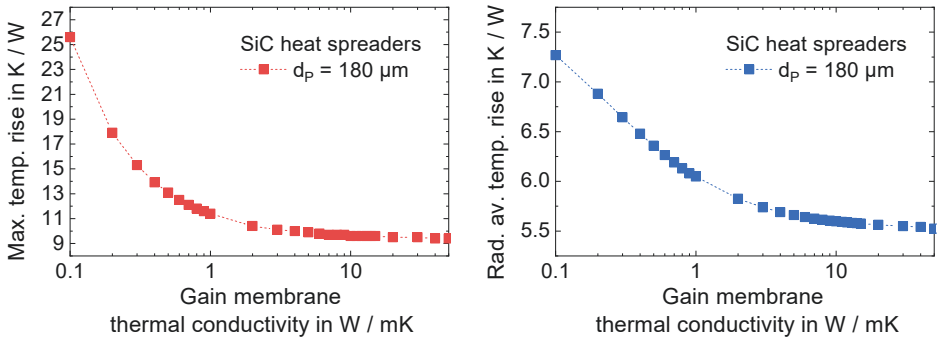

(a) Maximum temperature rise plotted over the gain membrane thermal conductivity.

(b) Radial average temperature rise plotted over the gain membrane thermal conductivity.

Figure 4.12 Relevance of the gain membrane thermal conductivity. The simulations have been performed with 350 µm thick SiC heat spreaders at 20°C heat sink temperature.

4.5.2 Gaussian and super-Gaussian pump beam profile

The incorporation of heat in the gain membrane can be lowered by a super-Gaussian pump beam which has a flatter pump beam profile than a Gaussian beam. Thermal management can get less challenging if there are no drastic peak temperatures near the center of the pump beam. A fiber-coupled diode laser with a 10^{th} order super-Gaussian pump beam profile can be considered for pumping. The heat generated within the gain membrane can be hereby expressed as

$$Q_{\mathrm{SG,\,n=10}}(r,z) \approx \frac{1.15 \cdot \eta_{\mathrm{Q}} \cdot P_0}{\pi w^2} \cdot \alpha \cdot \exp\left(-2\left(\frac{r}{w}\right)^{10} - \alpha\,(z_0 - z)\right). \tag{4.2}$$

According to the simulations in Fig. 4.13, the maximum temperature of the gain membrane can be lowered by a factor three for a pump beam diameter of 200 µm. For the radial average, the temperature with a super-Gaussian pump beam is by a factor of 15 lower than with a Gaussian pump beam. Therefore, power scalability in

MECSELs achieved with a super-Gaussian pump profile is larger than with a Gaussian pump profile.

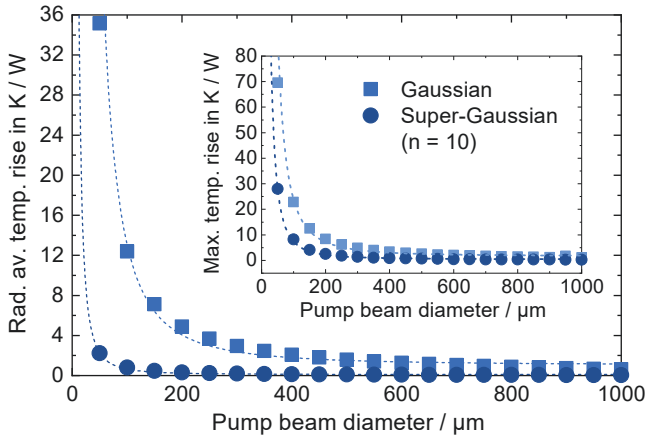

Figure 4.13 Radial average temperature rise of the gain membrane pumped by a Gaussian and a 10^{th} order super-Gaussian pump beam profile. The inset compares the maximum temperature. In this simulation 350 µm thick SiC heat spreaders are used to cool the gain membrane.

4.6 Conclusion

In this chapter, thermal simulations of MECSELs were performed via FEM and supported by experimental results. The double heat spreader approach in MECSELs generally provides a better thermal management than the single heat spreader approach. It has been found that the membrane temperature can be lowered by up to a factor of two with SiC and diamond heat spreaders with the double heat spreader approach whereas the benefit with sapphire heat spreaders is a factor of up to four. Furthermore, the maximum and radial average temperature can be lowered by a larger pump beam area. As simultaneously the threshold increases and the three-dimensional heat flow within the heat spreader becomes more significant, power scaling can be conducted up to a certain limit. For sapphire the pump beam diameter is limited within the hundred micrometer region. With SiC, the MECSEL can be operated at more than twice the pump beam diameter than with sapphire. This has been experimentally confirmed. Also, the membrane temperature does not vary much for a membrane thermal conductivity between 5 W/m·K and 50 W/m·K. The maximum membrane temperature with a super-Gaussian pump beam at a pump

beam diameter of 200 µm is about three times lower than with a Gaussian pump beam. The thermal benefit comes from the flat super-Gaussian pump beam profile, which can be applied for further power scaling of membrane lasers.

5 FROM SINGLE-SIDE TO DOUBLE-SIDE PUMPING

The fact that MECSELs operate in transmission mode is a huge benefit because the pump light can be injected into the semiconductor membrane from both sides, as it is shown in the photograph in Fig. 5.1.

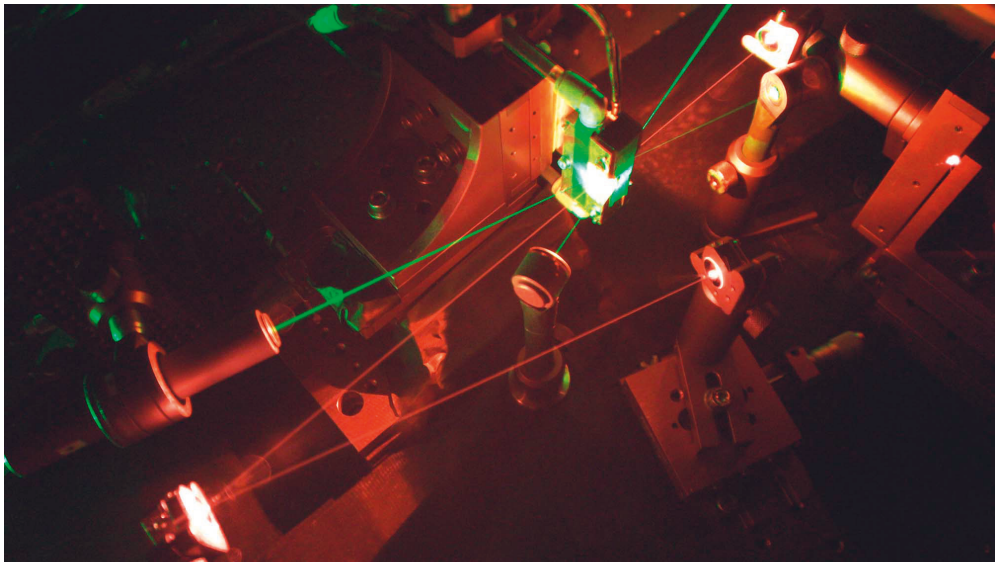

Figure 5.1 A photograph of the 780 nm emitting MECSEL with a double-side pump arrangement. The MECSEL near-infrared intra cavity beam within the V-cavity is captured by setting a long exposure time of eleven minutes. Photograph taken by Hermann Kahle from [105].

This allows the creation of a more homogeneous carrier distribution even in thick gain membranes compared to single-side pumping (SSP), at which the QW packages positioned on the backside experience less of the exponentially absorbing pump light. In this chapter, we reveal how the double-side pumping (DSP) improves the power performance in AlGaAs 780 nm-emitting MECSELs (gain membrane #1) in contrast to SSP. A comparison between SSP and DSP will be presented with SiC

heat spreaders (P1). In addition, the performance of another, thinner MECSEL gain membrane #2 emitting around 760 nm and cooled by sapphire intra cavity heat spreaders was investigated with DSP.

5.1 SSP vs. DSP with SiC

5.1.1 Gain membrane #1

The SSP and DSP investigations were compared with an MBE grown 577 nm thick MECSEL structure #1. After the substrate removal process as described in Sec. 3.5, the gain membrane #1 was attached between two uncoated 4H-SiC heat spreaders with a thickness of about 350 µm each. Designed for an emission wavelength of 780 nm, the gain membrane consisted of 4×3, $Al_{0.09}GaAs$ QWs, 7 nm thick, that were arranged between $Al_{0.39}GaAs$ barriers. $Al_{0.58}GaAs$ spacers separated the QW groups to the antinode positions of the electric standing-wave field in a 2.5λ sub-cavity (see Fig. 5.2). Furthermore, 10 nm AlInP and 10 nm GaInP layers around the gain region served as electron blocking and window layers at the semiconductor heat spreader interface. An SEM image of the unprocessed MECSEL structure can be seen in the inset in Figure 5.3. The QW packages can be identified as single stripes with a higher brightness.

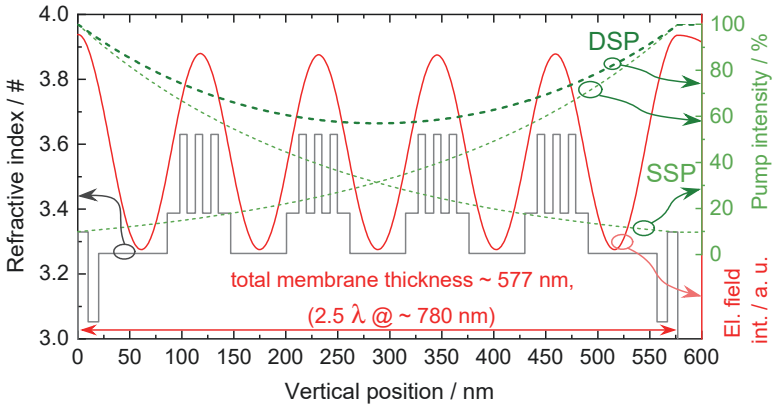

Figure 5.2 T-matrix simulation of the electric field distribution (red lines) and refractive index (grey lines) along the 780 nm gain membrane. Visualized is the pump intensity distribution using DSP (green bold short dashes) or SSP from each side (green short dashes). Reproduced from [105].

5.1.2 Experimental setup

The gain membrane-heat spreader sandwich was assembled into a copper heat sink mount, which was temperature stabilized to 20 °C via thermo-electric cooling. Indium foil was applied to improve the thermal contact between the surfaces. The conical aperture of the heat sink plates had a diameter about 1.5 mm (see inset photograph in Fig. 5.3), which was large enough for vertical laser emission and double-side pumping.

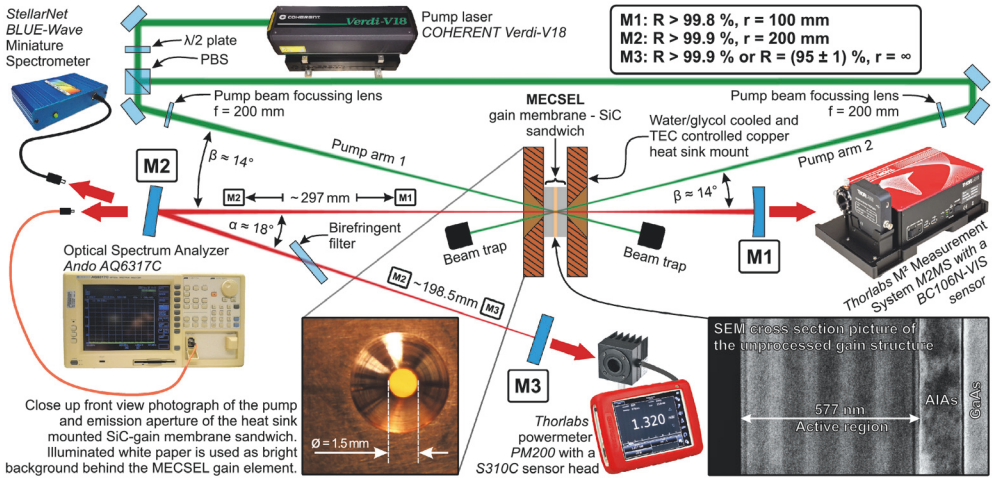

Figure 5.3 Schematic drawing of the MECSEL setup with the used laser mirrors M1, M2, and M3 for the V-cavity, and the measurement devices for the characterization of single-side and double-side pumping. Reproduced from [P1], with the permission of OSA Publishing.

Mounted to a tilt/jar stage and three linear axis stages, it was possible to adjust the gain element along all directions of space. A schematic drawing of the experimental setup with all the devices used in the characterization is shown in Fig. 5.3. The gain membrane was optically pumped at 532 nm by a Coherent Verdi-V18, which was a high-beam quality frequency doubled solid-state laser with 18.5 W maximum output power. The pump beam was focused by a 200 mm plano-convex lens. To have comparable results from the SSP and DSP measurements, the output power is plotted as a function of the absorbed pump power P_{abs}. The incident pump power P_{inc}, the

reflected pump power P_{refl}, and the transmitted pump power P_{trans} were measured directly before and after the gain element in order to calculate P_{abs}. For DSP, the polarization of the pump beam was adjusted by a $\lambda/2$ waveplate and the beam was split into two beams by a polarizing beam splitter (PBS). The pump absorption was nearly symmetrical.

For gain membrane #1, a V-cavity was formed by two HR plano-concave laser mirrors M1 and M2, and a plane outcoupling mirror M3. This allowed high output power transmission from one direction. The gain element was positioned in the intra cavity beam waist with diameters of $D_{\text{m, tan}} \sim 80\,\mu\text{m}$ and $D_{\text{m, sag}} \sim 155\,\mu\text{m}$ in tangential and sagittal planes. Due to the angle of incidence, the pump beam had a slight ellipticity with diameters of $D_{\text{p, sag}} = (88 \pm 8)\,\mu\text{m}$ in sagittal and $D_{\text{p, tan}} = (91 \pm 8)\,\mu\text{m}$ in tangential plane. 50% of the total absorbed pump light (100%) within the gain membrane was attributable from the absorption from pump arm 1 and 50% from pump arm 2. According to Beer-Lambert law, the pump light was absorbed within the gain membrane and the intensity decayed exponentially as simulated in Figure 5.2. The average absorption coefficient $\alpha_{532\text{nm}} \sim 4 \cdot 10^4\,\text{cm}^{-1}$ was determined from the pump power absorption measurements. If SSP was applied, less than 15% of the initial pump light remained for the last QW on the backside. This should not be very problematic in our case. Only for even thicker gain membranes, it can occur that the pump light is not any more high enough at the backside QWs for SSP. The unpumped QWs in that sense become a lossy element that only absorbs without contributing to lasing. With DSP, a more homogeneous pump light distribution within the gain membrane is expected than with SSP.

5.1.3 Comparison of the output power performance

The SSP1 and DSP power performance using $R_{\text{M3}} = 95\%$ at $T_{\text{hs}} = 20°\text{C}$ are compared in Fig. 5.4. To obtain all the power from the pump laser, the PBS was removed from the setup in the SSP1 configuration. Three positive effects on the output power can be clearly seen if DSP was applied: a lower threshold, a higher differential efficiency, and maximum output power. DSP contributed to a lower threshold of 0.69 W, which was initially about 0.79 W for SSP1. Furthermore, DSP enabled the MECSEL to increase the differential efficiency slightly from 31.9% to 34.4%. The higher maximum output power of 3.22 W required a smaller P_{abs}. In both pump

configurations, the power curve started to deviate from its initial linear behavior at $P_{abs} = 8$ W. This could be a sign of thermal roll-over setting in [41].

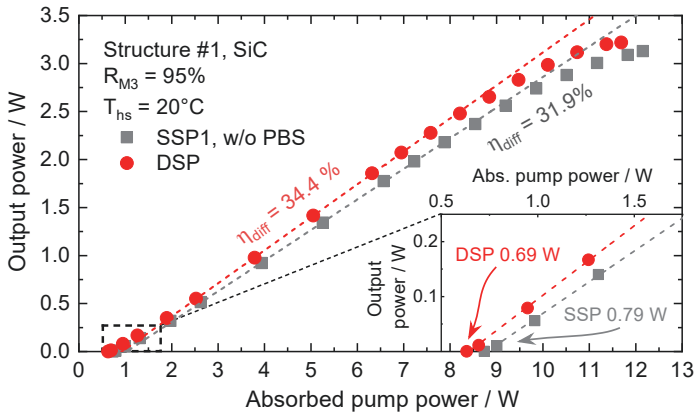

Figure 5.4 Output power comparison in SSP (pump arm 1) and DSP configurations at 20°C. An enlarged view to the threshold region is given by the inset. Reproduced from [P1].

5.1.4 Spectral characteristics

To check the emission wavelength, an HR spectrum of the free-running MECSEL was measured and plotted in Fig. 5.5.

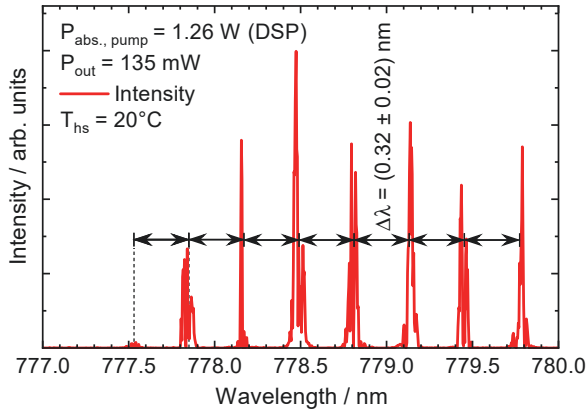

Figure 5.5 HR spectrum of the free-running 780 nm MECSEL measured with an Ando AQ6317C OSA with an average time of 20 s. Reproduced from [P1], with the permission of OSA Publishing.

Matching to the design wavelength, the MECSEL operated at around (778 ± 1) nm. It should be mentioned here that the spectrum contained the typical longitudinal

laser modes. Spectral filtering was given by the uncoated SiC pieces. They acted like a Fabry-Pérot etalon and multi-beam interference occured at the nearly plane parallel surfaces when the intra cavity beam propagated through. This can be confirmed by the measured mode spacing of (0.32±0.02) nm which is nearly equal to the calculated FSR of the SiC pieces. As a further investigation, wavelength tuning measurements were performed by rotating a thick birefringent filter inside the cavity (see Fig. 5.3). A 0.5 mm birefringent filter with a FSR of $\Delta\lambda_{780\,\mathrm{nm}} = 136.6\,\mathrm{nm}$ was incorporated that allows a wide continuous tunability. With an HR outcoupler, a tuning range of 44.5 nm was measured from 767.0 nm to 811.5 nm as plotted in Fig. 5.6. Because the 0.5 mm birefringent filter did not introduce high enough losses to tune the MECSEL with the 5 % outcoupling mirror, a 2 mm birefringent filter was applied. By this, the output exceeded 1.6 W at 781 nm and was tunable over a range of 22.5 nm. Both measured tuning curves revealed a typical output power distribution centered around the gain maximum.

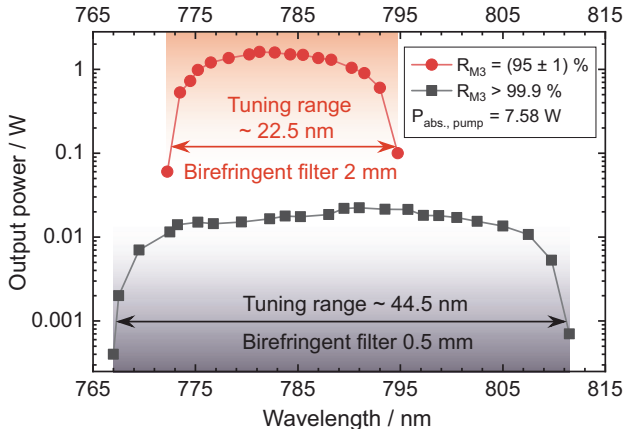

Figure 5.6 Wavelength tuning results of the 780 nm MECSEL. Reproduced from [P1].

5.1.5 Thermal investigations

Since the temperature inside the gain membrane or near its surface cannot be directly measured, an alternative, indirect method was applied to determine the thermal resistance. This practical method [104, 109] was based on spectral shift measurements. It involved the monitoring of the MECSEL emission wavelength when either the pump power or the heat sink temperature T_{hs} was modified. The heat flow was as-

sumed to have a constant distribution. Correspondingly, the temperature inside the gain membrane was a linear function of the dissipated power with $P_{\mathrm{diss}} = P_{\mathrm{abs}} - P_{\mathrm{out}}$, where P_{abs} was the absorbed pump power and P_{out} the MECSEL output power. The thermal resistance R_{th} corresponded to the slope and could be expressed in units of K/W and derived as follows:

$$R_{\mathrm{th}}\,[\mathrm{K/W}] = \frac{\partial\lambda/\partial P_{\mathrm{diss}}}{\partial\lambda/\partial T} \;\text{ in }\; \left[\frac{\mathrm{nm/W}}{\mathrm{nm/K}}\right]. \tag{5.1}$$

Figure 5.7 shows how the MECSEL center emission wavelength varies with P_{diss} as well as with T_{hs}. Although the emission wavelength near the lasing threshold is similar for all configurations, the MECSEL operated on average at a slightly shorter emission wavelength with DSP. On the one hand, this could indicate that the thermal situation in the gain membrane near the threshold is similar in all three pump configurations. Secondly, the shorter emission wavelength in the DSP configuration could mean a slightly lower temperature within the gain membrane.

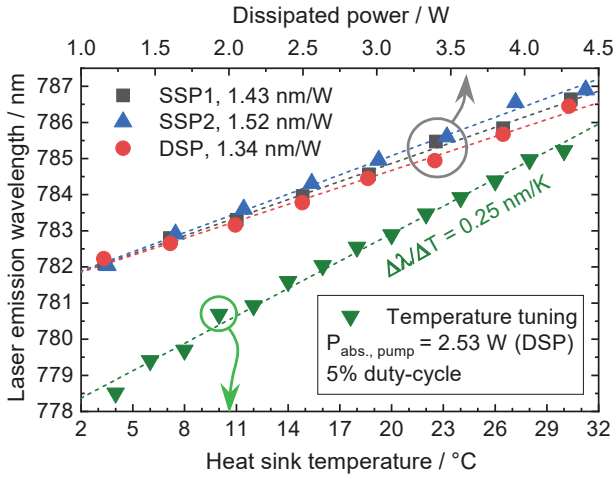

Figure 5.7 Spectral shift of the MECSEL in relation to the dissipated power (upwards pointing triangles, full squares, and circles) and the heat sink temperature (full downwards pointing triangles). Reproduced from [P1], with the permission of OSA Publishing.

Furthermore, the measurements revealed a smaller spectral shift of 1.34 nm/W for DSP while for SSP1 and SSP2 the spectral shift was equal to 1.43 nm/W and 1.52 nm/W, respectively. It can be seen that the spectral shift was not the same for SSP1 and SSP2. One possible reason is that the pump spot size for each pump arm side is slightly dif-

ferent. A smaller pump spot size at the same pump power could cause a stronger heating effect, and induced therefore a larger spectral shift. On the other hand, by increasing up T_{hs}, emission wavelength red shifted with a rate of 0.25 nm/K with DSP at a fixed $P_{abs} = 2.53$ W. On both pump beams, a duty-cycle of 5% was applied to avoid heat from the pump laser that causes any wavelength shift. Finally, Eq. 5.1 yielded a thermal resistance of $R_{th,\,DSP} = 5.36$ K/W for DSP and $R_{th,\,SSP12} = 5.9$ K/W on average for SSP. Although the results indicated a similar thermal situation in the gain membrane, one obtained a slightly lower thermal resistance value for DSP.

5.1.6 COMSOL Multiphysics® simulations

As can be analyzed from the previous measurements in Sec. 5.1.5, the gain membrane was obviously too thin to be much affected by the pump configuration. However, DSP was expected to be more effective for gain membranes with larger thicknesses. To further investigate this, heat transfer simulations were conducted in COMSOL Multiphysics® and presented here in the following.
It was assumed that the Gaussian pump beam penetrates perpendicularly into the structure. Here, the pump was absorbed within the whole membrane but mostly in the AlGaAs spacer layers. Correspondingly, a simplification was made by using the absorption coefficient of AlGaAs spacer material only as listed in Tab. 5.1.

Fig. 5.8 points out that the maximum temperature in the 577 nm thick gain membrane could exceed 140 °C at 10 W absorbed pump power. Although the simulated maximum temperature at 10 W pump power is fairly high, the MECSEL does not switch off. Here, it needs to be considered that the spatially temperature distribution adapts the Gaussian power distribution from the pump laser. This directly means that the temperature decreases with the radial distance. In that sense, these high temperatures at the center of the pumped region are tolerated as long as the cooler temperature regions within the pumped structure are able to sustain the lasing process. This could mean that lasing is not much affected by the maximum temperature but more by the temperature averaged over the radial distance. These assumptions are underlined by the simulated values. A linear fit to the averaged temperature yields a slope of 5.83 K/W for DSP. The temperature increase is again slightly lower than the value obtained from a SSP configuration and therefore agrees well with the mea-

surement data presented in Fig. 5.7.
As already discussed, DSP can be especially beneficial for thick gain structures. However, for thin structures, this pumping scheme is not crucial.

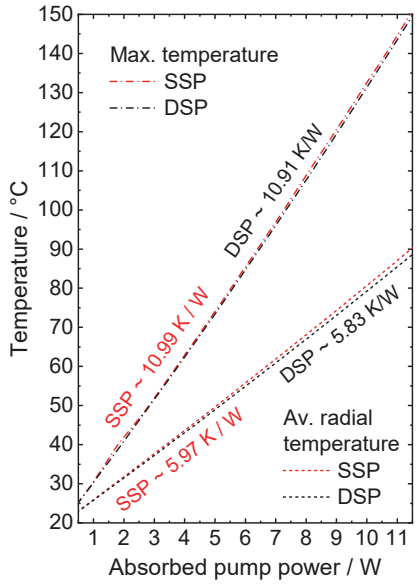

Figure 5.8 Simulated maximum temperature (dash dots) and radial average temperature (short dashes) within the 577 nm thick gain membrane using SSP (red) and DSP (black).

Cooling conditions	
T_{hs}	20°C
t_{SiC}	350 µm
$k_{z,\mathrm{SiC}} = k_{r,\mathrm{SiC}}$	490 K/mW
Gaussian pump laser	
D_{p}	88 µm
λ_{p}	532 nm
Gain membrane	
t_{MECSEL}	577 nm
$\alpha_{532\mathrm{nm}}$	$4 \cdot 10^4$/cm
$k_z = k_r$	12 K/m·W [110]

Table 5.1 Parameters used in the simulation.

To figure out at which thicknesses DSP becomes important, the maximum as well as the radially averaged temperature increase are plotted in Fig. 5.9 and Fig. 5.10. Both figures illustrate that DSP principally contributes to a smaller temperature increase. Starting from membrane thicknesses over 625 nm, the simulations propose that DSP can be beneficial. The average radial temperature for DSP begins to saturate for structures thicker than 1 µm and remains below 6.4 K/W. On the other hand, the averaged radial temperature increase of a SSP structure arrives almost at 7.1 K/W because the maximum temperature strongly rises.
As a further investigation, the temperature is plotted over the vertical structure position. Fig. 5.11 shows the relationship for a thin structure with 500 nm thickness at 9 W absorbed pump power at the radial center. While the DSP structure owns a more homogeneous temperature distribution, the maximum temperature for the

SSP structure is closer to the heat spreader which is facing towards the pump beam side.

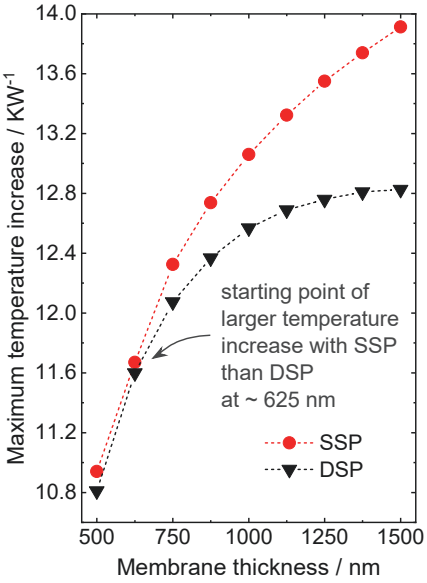

Figure 5.9 Maximum temperature increase plotted versus the membrane thickness. DSP can be advantageous for structures thicker than ~ 625 nm.

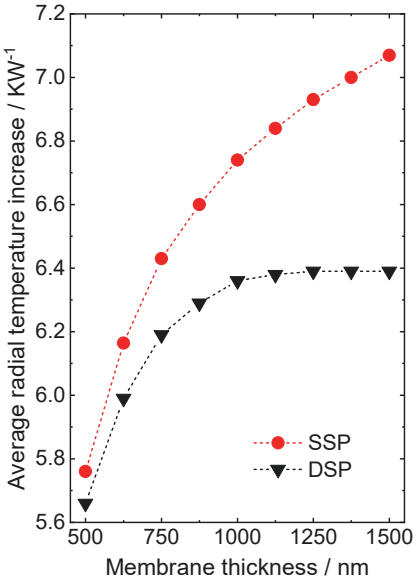

Figure 5.10 Temperature increase averaged over the radial distance from the center of the membrane plotted versus the membrane thickness.

Due to the close contact to the heat spreader, heat is directly dissipated away from the structure surface. The hottest region in a SSP structure is therefore not at the surface, where the pump beam intensity is the highest but at distance of 135 nm. Furthermore, the temperature difference between the minimum and the maximum in the SSP structure is only about 7°C.

This is different for a 1.5 µm thick SSP structure as can be seen in Fig. 5.12. Here, the maximum temperature is ~ 30°C hotter than the much less pumped region on the backside of the structure. On the other hand, the DSP structure obtains a flat temperature distribution. The lower temperature is therefore a direct result of a better heat conduction from the combination of the double-side pumping with the double-side cooling configuration.

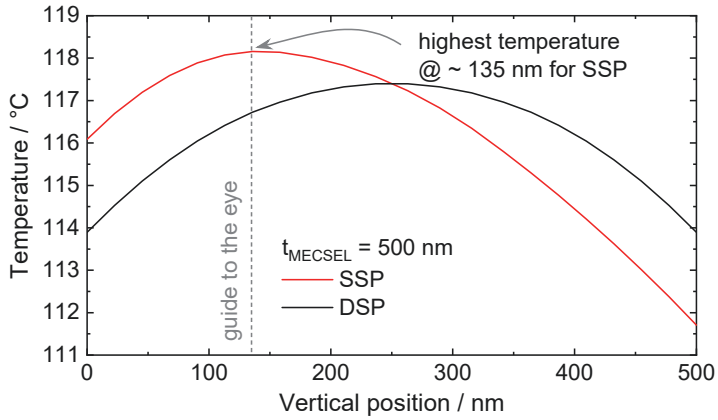

Figure 5.11 Vertical temperature distribution across a 500 nm thin membrane. In both SSP (red lines) and DSP (black lines) the total absorbed pump power is 9 W. For SSP, the pump light penetrates from the position at the 0 nm side.

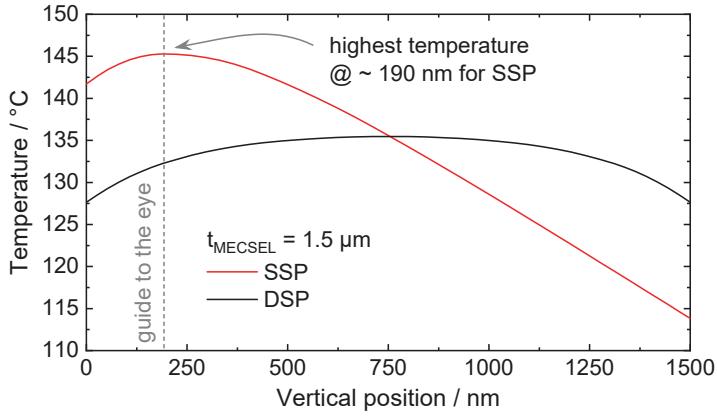

Figure 5.12 Vertical temperature distribution across a 1.5 µm thick membrane compared between SSP (red lines) and DSP (black lines) at 9 W absorbed pump power.

5.2 DSP with sapphire heat spreaders

5.2.1 Gain membrane #2

Gain membrane #2 employed 2×3 $Al_{0.12}GaAs$ QWs with $Al_{0.4}GaAs$ barriers and $Al_{0.49}GaAs$ claddings. While each QW was 7 nm thick, the thickness of the barriers corresponded to 8 nm between the QWs, and 12 nm next to the QW packages. Thus, the gain membrane thickness in structure #2 resulted to about 335 nm which

conformed to a 1.5 λ sub-cavity. As like gain membrane #1, the gain membrane #2 was surrounded from both sides by 10 nm thick AlInP electron blocking, and 10 nm thick GaInP capping layers. Gain membrane #2 was bonded between two sapphire heat spreader pieces, each 500 µm thick.

Transmission measurements

Before the gain membrane - heat spreader sandwich was built into the laser cavity, transmission measurements of the sapphire - gain membrane #2 - sapphire sandwich were performed with a white light LS-1 tungsten halogen lamp from Ocean Optics as plotted in Fig. 5.13. Since the gain membrane was designed to absorb the pump light at 532 nm in all layers, the transmission was expected to be small around 532 nm which is here the case.

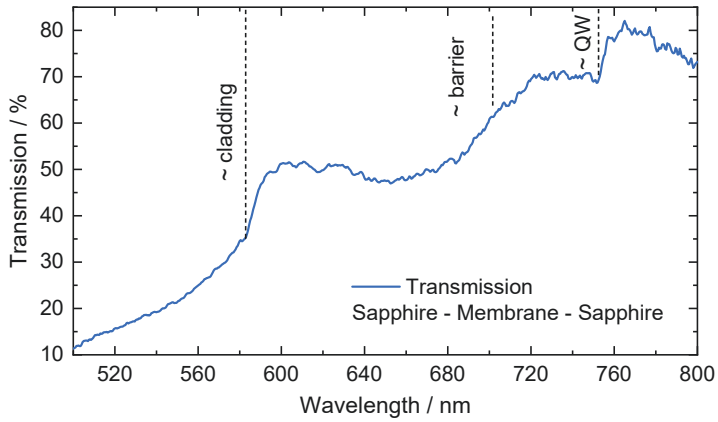

Figure 5.13 Transmission measurements through the sapphire - 760 nm membrane - sapphire sandwich.

If the incident wavelength increases until its corresponding photon energy becomes smaller than the absorption edge of the cladding material, and subsequently the barrier and QW material, the absorption drops. Accordingly, the transmission increases progressively near the absorption edges as can be seen in Fig. 5.13. In total, three local maxima can be identified around $\sim$ 570 nm, $\sim$ 700 nm, and $\sim$ 750 nm which correspond to the absorption edges of the cladding material $Al_{0.49}GaAs$, barrier material $Al_{0.4}GaAs$, and $Al_{0.12}GaAs$ QWs [111]. A maximum transmission was achieved around 80% at longer wavelengths than the corresponding QW band gap energy because 20% of the incident pump light was attributable to reflection losses at the

air-sapphire interface.

5.2.2 Cavity and pump configurations for gain membrane #2

The 760 nm emitting gain membrane #2 was characterized in a ~ 172 mm long linear cavity, which consisted of M1 ($r_{M1} = 100$ mm, $R_{M1} = (97 \pm 1)\%$) and M2 ($r_{M2} = 75$ mm, $R_{M1} > 99.9\%$). With the gain element placed very close to the cavity beam waist, the operating cavity mode diameter corresponded to $\sim 100\,\mu$m. The pump mode to a diameter of $(97 \pm 8)\,\mu$m in tangential and $(100 \pm 8)\,\mu$m in sagittal plane, and thus mode matching was approximately achieved. It also has to be noted that only DSP was applied for the characterization of gain membrane #2. From the total absorbed pump light, about 51% originated from the absorption via pump arm 1, and 49% via pump arm 2. Thus, gain membrane #2 absorbed the pump light as like gain membrane #1 very homogeneously from both sides.

5.2.3 Power performance

The output power performance of the 760 nm MECSEL (gain membrane #2) at a heat sink temperature of 21.5°C is plotted against the absorbed pump power in Fig. 5.14.

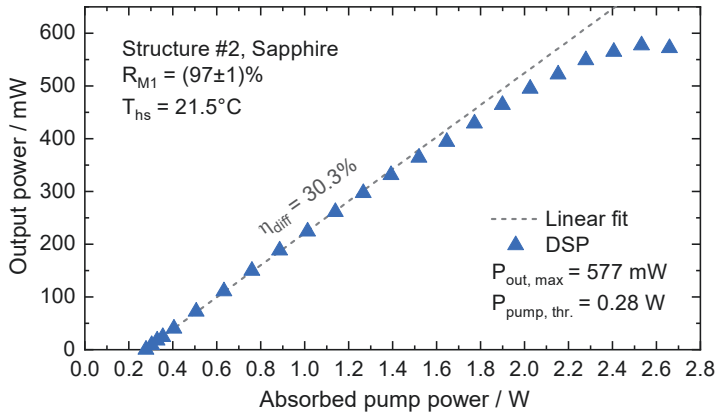

Figure 5.14 Power performance of a 760 nm sapphire MECSEL, gain membrane #2. At about half of the maximum absorbed pump power, the output curve starts to deviate from its linear behavior. Reproduced from [105].

With an outcoupling reflectivity of $R_{M1} = (97 \pm 1)\%$, the lasing threshold was reached

at $P_{abs} = 0.28\,W$. The differential efficiency obtained from a linear fit to the measurement data from P_{abs} in the range of 0.2 W to 1.2 W, was about $\eta_{diff} = 30.3\%$. Although gain membrane #2 owned half of the amount of QWs compared with gain membrane #1, the differential efficiency values from both were nearly similar. Since gain membrane #2 could be only pumped up to 1/5 of the maximum pump power that gain membrane #1 thermally endured using SiC, the maximum output power obtained here with sapphire was correspondingly 577 mW, which was about five times lower.

To determine the thermal resistance, the spectral shift is plotted as a function of the dissipated power in Fig. 5.15a.

A laser emission spectrum centered at 770 nm was measured at $P_{abs} = 1.65\,W$ as plotted in Fig. 5.15b.

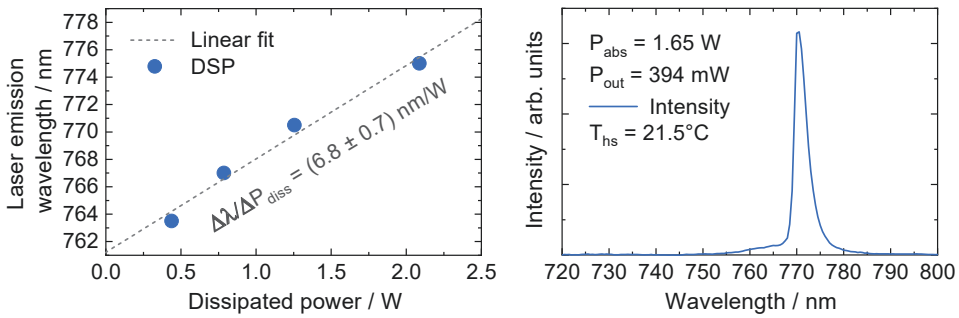

(a) Spectral shift measurements of the sapphire MECSEL plotted against the dissipated power.

(b) MECSEL emission spectrum taken during the spectral shift measurements.

Figure 5.15 Spectral characteristics of the 760 nm sapphire-cooled MECSEL. Reproduced from [105].

By assuming that the spectral shift with the heat sink temperature was similar to gain membrane #1 as the material compositions are not much different, the thermal resistance was calculated as $R_{th} = (27.2 \pm 2.8)\,K/W$. This is about five times larger than the value obtained with the SiC-cooled gain membrane #1.

5.3 Conclusion

In this chapter, we have investigated the potential benefits of DSP in a MECSEL to introduce a more uniform heating. Compared with SSP, the lasing threshold was lowered from 0.79 W to 0.69 W in a 780 nm-emitting 4×3 AlGaAs QWs MECSEL. The analysis revealed a differential efficiency increase from 31.9% to 34.4%. Limited

by thermal roll-over, the maximum output power exceeded 3.22 W. With SiC heat spreaders and at 20°C heat sink temperature, these are excellent values [20, 112–114]. Furthermore, the thermal resistance for SSP was measured as 5.36 K/W; and 5.9 K/W for DSP. At this point, the difference was not significant. A possible reason is that the membrane was relatively thin, only about 577 nm. This presumption was confirmed by heat transfer simulations which showed that the thermal situation was in general good for such a thin membrane. If heat is introduced to such a thin membrane, the temperature does not vary much along the pump direction in both SSP and DSP. Hence, the laser performance was not influenced much by the pumping scheme as observed in our experiments. However, for gain membranes thicker than $\sim$ 625 nm, DSP was expected to become more relevant. The access of two pump beams from two sides could create a more evenly distributed temperature along the pump direction at a lower maximum temperature. Since this could lead to a lower thermal resistance, DSP is a promising approach in the future to pump thick or stacked gain membranes for high-power operation.

Besides using SiC as an intra cavity heat spreader material for the 780 nm gain membrane, a power and thermal investigation was performed here with sapphire to cool a second gain membrane which was designed for an emission wavelength of 760 nm. Although the 760 nm gain membrane had less gain material (2×3 AlGaAs QWs only), and the thermal conductivity of sapphire was about ten times lower than SiC, the differential efficiency of 30.3% was very close to the value obtained with the 780 nm SiC cooled MECSEL. Owing to the high optical quality of sapphire, the 760 nm MECSEL output power exceeded > 0.5 W. Since the laser threshold was about 0.28 W absorbed pump power, and the maximum output power was achieved at about 2.5 W absorbed pump power, the sapphire MECSEL did not consume much pump power. If high output power performance is not very important, a way to further make this MECSEL more cost-efficient is to use green 525 nm emitting laser diodes which are commercially available at 1 W output power [115] instead of the solid state Verdi-V18 pump laser in the future.

6 HIGH-POWER 8XX NM MECSELS

The accumulation of heat in the gain structure leads to thermal roll-over and ultimately limits the output power [116]. For this reason, power scaling techniques presented in semiconductor disk lasers [117] have one thing in common, which is to distribute the heat over a larger area. Kuznetsov et al. suggested to optically pump multiple spots on a large gain element [47, 118]. The individual emission from each spot can be combined together to a high power array. Another technique involves multiple separate gain elements which shares the same cavity [119, 120]. The benefit here is that excessive heating can be further avoided since the gain elements are individually cooled by their own heat sink. With this method, Yb:YAG lasers using four laser crystals provided over 1 kW output power [121].

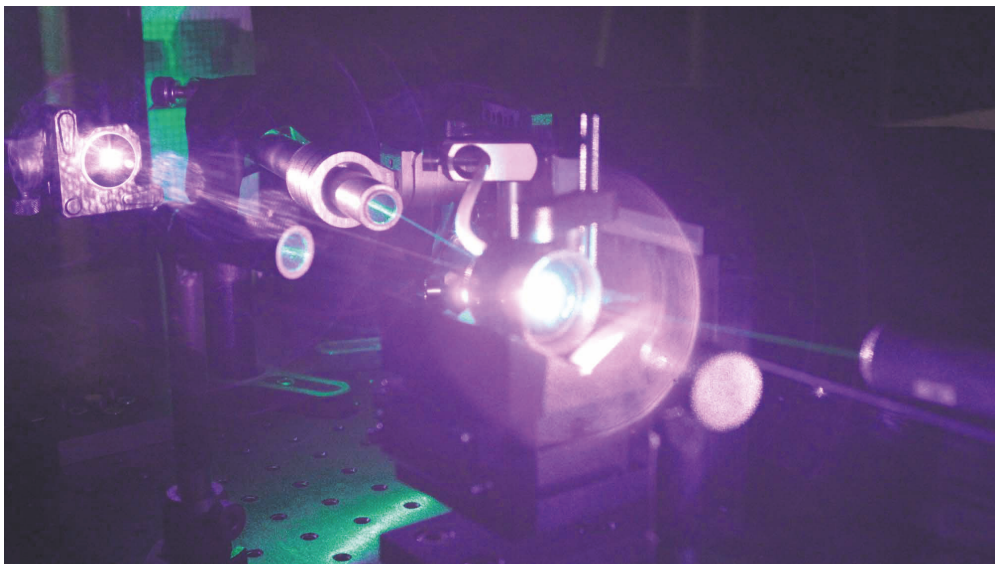

Figure 6.1 A photograph of the 825 nm emitting MECSEL during operation. The infra red filter was removed from the camera. So it was possible to capture the intra cavity MECSEL beam that is illustrated here in purple. In addition, the green pump beam impinging from two sides onto the MECSEL sample is visible.

In this chapter, power scaling in a single MECSEL gain element is demonstrated. A more traditional way of power scaling known from semiconductor disk lasers is applied by increasing the pump spot size [13, 122, 123]. The experiments are performed in a MECSEL with an emission wavelength of 825 nm as illustrated in Fig. 6.1. In the short 8XX nm region, neither a VECSEL nor a MECSEL has been reported so far. At the moment, laser diodes are commercially available at this wavelength. The wavelength is also covered by Ti:sapphire lasers that have already been used for example in differential absorption lidar (DIAL) research for atmospheric sensing [124, 125]. Just as the Ti:sapphire laser, the MECSEL can serve as a probe laser in the future at much lower cost to scan ground-based water-vapor at 820 nm, for instance. Furthermore, thermal lensing is investigated how it affects the beam quality of a MECSEL. The results have been published as a peer-reviewed article P2 and conference proceeding [106].

6.1 Gain membrane

The MECSEL structure was fabricated on an undoped (100) $\pm$ 0.5° GaAs substrate wafer in a V80H-10 VG Semicon solid source MBE reactor. An AlAs layer served as a process layer as described earlier in Sec. 3.5. Illustrated in Fig. 6.2 is the T-matrix simulation of the refractive index and electric field intensity distribution along the MECSEL structure.

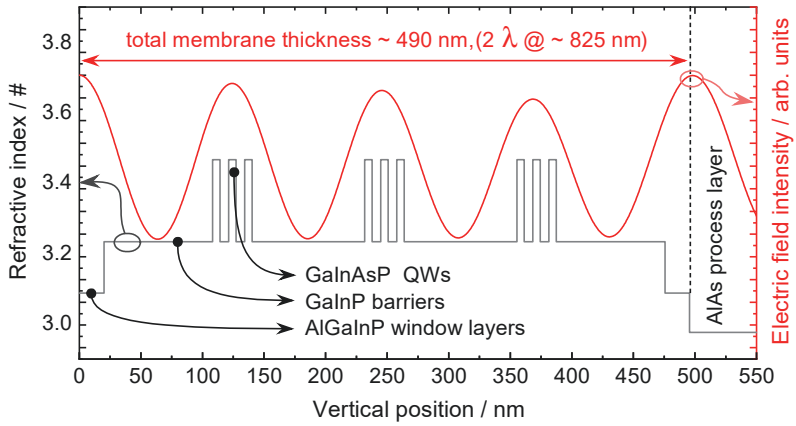

Figure 6.2 T-matrix simulation of the electric field distribution (red) and refractive index (black) plotted along the vertical position in the MECSEL structure.

Nine GaInAsP QWs were equally arranged according to an RPG structure design into three groups with half a wavelength spacing to each other. The QW groups were located near the antinodes of the electric standing wave field that was formed in the membrane sub-cavity. The structure was optimized to be resonant. For barrier pumping at 532 nm, GaInP was used in the barriers/spacers to absorb the pump light and to provide a sufficient charge carrier confinement preventing the charge carriers from a too early thermal escape. The gain region was additionally surrounded by higher band gap energy AlGaInP window layers from both sides.

6.2 Experimental setup

The gain membrane was bonded between two transparent, uncoated 350 µm thick, 4H-SiC heat spreader pieces. The membrane-heat spreader sandwich was assembled in a copper heat sink similar to Sec. 5.1.2. Two different V-cavities, which are denoted here as cavity 1 and cavity 2 with a schematic drawing illustrated in Fig. 6.3, were used to compare how the cavity mode area on the MECSEL gain membrane affects the overall power performance.

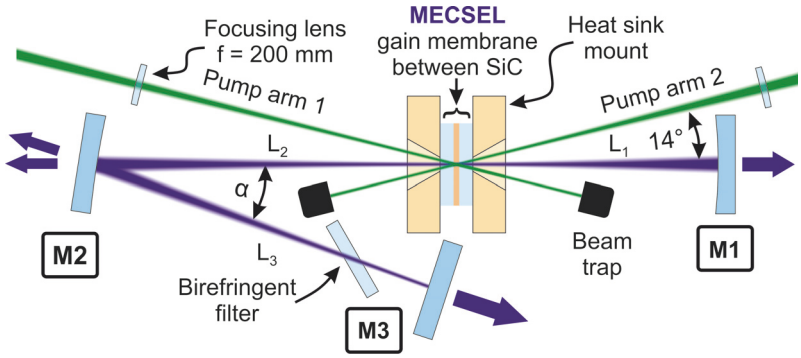

Figure 6.3 Schematic drawing of the 825 nm emitting MECSEL setup with the double-side pump arrangement. The setup was used for all characterization measurements. The membrane was placed at a distance to M1 and M2 of L_1 and L_2. L_3 denotes the distance between M2 and M3, here. Reproduced from [P2], with the permission of OSA Publishing.

For a smaller, elliptical cavity mode area with $D_{\mathrm{m,tan}} = (87 \pm 18)$ µm and $D_{\mathrm{m,sag}} = (162 \pm 6)$ µm in diameter along the tangential and sagittal planes, the measurements were performed in cavity 1. A larger cavity mode area with $D_{\mathrm{m,tan}} = (127 \pm 16)$ µm

and $D_{\mathrm{m,sag}} = (173 \pm 8)$ µm in diameter was provided by cavity 2. The used laser mirror curvatures, mirror distances L_1, L_2, and L_3, and the folding angles α for the two different configurations can be found in the publication P2. The gain membrane was optically pumped from two sides under an incident angle of about 14° at 532 nm from a Coherent Verdi V-18 laser. The collimated pump beam was focused down onto the membrane by a plano-convex lens with a focal length of 200 mm. The pump area was individually re-adjusted for each cavity. By measuring the power of both reflected pump beams without laser operation, the reflection losses at the front surfaces of the uncoated SiC heat spreaders were estimated to be about 26%. The power of the transmitted pump beams were measured to find out the approximate absorption. About 70% of the incident pump beam got absorbed in the gain membrane.

6.3 Results

6.3.1 Power characteristics

The input-output power characteristics measured in both cavities under laboratory and room temperature conditions of 20 °C are plotted in Fig. 6.4.

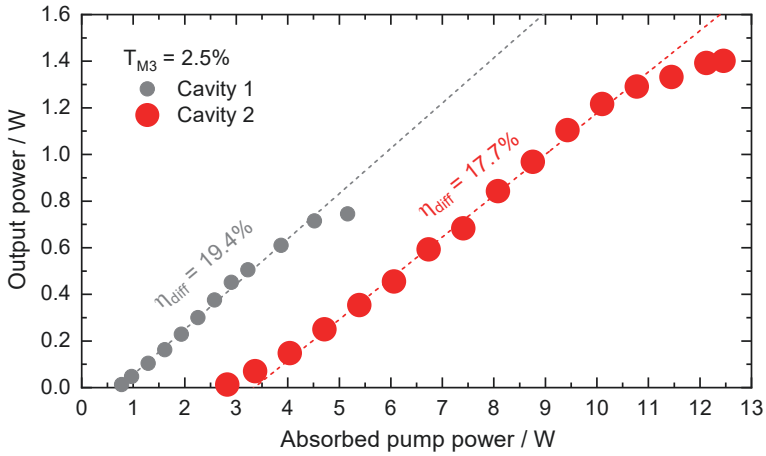

Figure 6.4 Power scaling results in an 825 nm MECSEL. By increasing both, the cavity mode and pump mode area, the MECSEL output power is doubled from 0.7 W (with cavity 1) to 1.4 W (with cavity 2) at a heat sink temperature of 20 °C. Reproduced from [P2], with the permission of OSA Publishing.

Clearly distinguishable are the threshold and the maximum output power. When the MECSEL operated in cavity 1, lasing was achieved at 0.77 W. By assuming that the pump diameters $D_{p,tan} = (88 \pm 4)$ µm and $D_{p,sag} = (98 \pm 5)$ µm along both propagation axis, the pump threshold density would correspond to approximately $\sim 11\,kW/cm^2$. This is comparable to earlier VECSEL results [50]. The output power, only measurable behind the outcoupling mirror M3 with a transmission of 2.5%, reached its maximum at 0.72 W with a differential efficiency of 19.4% before thermal rollover. Finally, to scale up the power, the MECSEL was set up in cavity 2. The pump area was re-adjusted to maximize the output power at the highest pump power level. As predicted by the simulations of Laurain et al. [59], a maximum yield was obtainable at $\sim$ 14 W pump power provided by the Gaussian pump beam. Here, the given cavity mode to pump mode diameter ratio D_m/D_p was in the range between 0.55 and 0.75, meaning that the overall pump area was larger than the cavity mode area. Our configurations perfectly matched to these simulations, with a mode ratio $D_m/D_p = 0.66 \pm 0.14$.

Due to the larger pump area, the lasing threshold increased to 2.83 W absorbed pump power which corresponded to a slightly lower pump power density of about $7\,kW/cm^2$. With a barely changing differential efficiency of 17.7%, thermal rollover was setting in at higher pump power, and the maximum output power was doubled to 1.4 W, including the transmission from M1 (cavity 2). In principle, the output power can be further increased by a larger pump area with thicker SiC heat spreaders [65] since the used pump spot diameter of about 209 µm here was not very large. Pump spot diameters as large as $\sim$ 950 µm had been applied in high power VECSELs, which had lead to 72 W in 1180 nm-emitting VECSELs [14] and 106 W in 1028 nm-emitting VECSELs with InGaAs QWs [26]. It should be considered that diamond heat spreaders had been used in the high-power VECSELs, and the high thermal conductivity of diamond had enabled such large mode areas and pump powers. This power scaling approach has a certain limit which is due to the three dimensional heat flow taking place in the heat spreader [101]. If one considers that heat in the gain membrane is mainly transported from the surface through the heat spreaders, heat does not only flow in the axial but also in the lateral direction through the heat spreaders and then to the heat sink. Once the pump area gets larger, the lateral heat component is getting more important, i.e. heat needs to be transported away from the center to the edge of the pump spot area or otherwise the thermal resistance rises.

6.3.2 Optimal outcoupling value

Each oscillating mode propagating within a laser cavity faces two different kind of losses during a single cavity pass [126]. First, losses occur from outcoupling. Second, non-radiative absorption, scattering, diffraction can take place inside the gain material or at the laser mirror surfaces. These losses are considered as internal or resonator losses. The internal losses for VECSELs were commonly estimated by the Findlay-Clay method [127]. Typical values measured in VECSELs are between 2% and 6% [48, 128, 129]. To enable lasing, the single-pass gain needs to overcompensate all the losses. The relation between the output power P_{out} and the total outcoupling transmission T can be formulated as

$$P_{\mathrm{out}} = C \cdot T \left[\frac{g_0}{L_{\mathrm{i}} + T} - 1 \right], \tag{6.1}$$

where C is a saturation power related fit parameter, L_{i} the internal losses, and g_0 the unsaturated gain. Without going into much deep investigation what the internal losses and the unsaturated gain values are, Eq. 6.1 was used here to make a relative comparison and to verify the optimal outcoupling transmission for this kind of small amount of QWs gain membrane. The power performance was measured in cavity 2 with a set of different outcoupling transmission at the same pump conditions and plotted in Fig. 6.5a. As can be seen, the power curves at $T_{\mathrm{M1+M3}} = 2.9\%$ and $T_{\mathrm{M1+M3}} = 1.4\%$ are similar in differential efficiency and maximum output power, possibly because the optimum transmission value is inbetween. To have a closer look, the output power at 8 W absorbed pump power measured at all available combinations giving $T_{\mathrm{M1+M3}}$ is visualized in Fig. 6.5. It was experimentally tested out that there was no lasing with the available 5.4% outcoupling mirror most likely because the gain from the relative small amount of QWs was not high enough. To obtain the optimum transmission value, the fit function requires a threshold value. Since the threshold cannot be more exactly determined as between 3% and 5.4%, further presumptions only rely on Eq. 6.1. The resulting fit parameters g_0 and L_{i} need to be considered. A fit to Eq. 6.1 with 5.4% total outcoupling threshold yielded a value for $g_0 = (11.9 \pm 1.8)\%$, as well as for $L_{\mathrm{i}} = (6.6 \pm 1.8)\%$. At the optimal outcoupling transmission around 2.3%, about 5% output power increase can be expected from the maximum of the fit function. On the other hand, the fit revealed very high

values for g_0 and L_i the smaller the threshold value is set. Below 4.7%, both values for $g_0 > 26\%$ and $L_i > 22\%$ are too high to be realistic. For a comparison, fit functions with smaller g_0 values of 6.5% and 7.5% and L_i values of 0.7% and 2% are included.

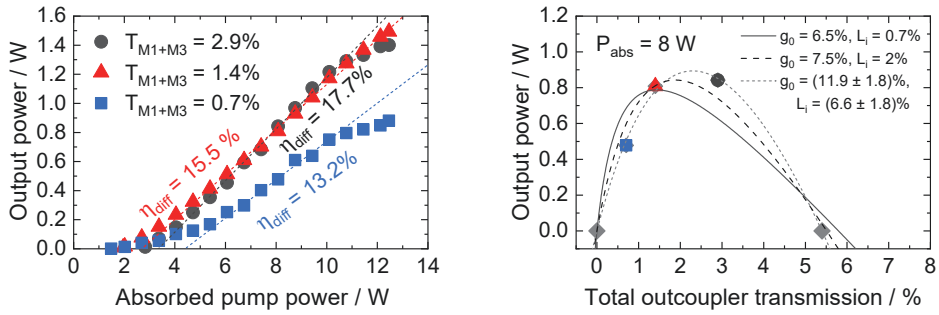

(a) Power curves measured at different outcoupler transmissions

(b) Output power of the MECSEL plotted versus the total transmissions of M1 and M2 at $P_{abs} = 8\ W$.

Figure 6.5 Optimal outcoupling mirror transmission in cavity 2 for the 825 nm MECSEL around 1.2%. Reproduced from [P2], with the permission of OSA Publishing.

6.3.3 Covering a spectral gap in the short 8XX nm region

An HR spectrum was measured at $P_{abs} = 6.7\ W$ with an HR outcoupling mirror in cavity 2. As shown in Fig. 6.6, the lasing wavelength was centered at 829 nm.

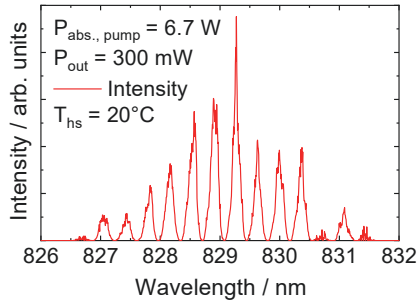

Figure 6.6 HR spectrum of the free-running 825 nm MECSEL measured with an Ando AQ6317C OSA with an average time of 20 s.

Fig. 6.7 outlines the realized VECSELs and MECSELs in the short 8XX nm wavelength region. Although there were no fundamental difficulties to realize VECSELs in the wavelength region between 810 nm and 830 nm as there are suitable material systems to grow a DBR and the gain structure, a spectral gap was left. The 825 nm

MECSEL was able to cover this spectral gap as can be seen in wavelength tuning measurements with a 2 mm thick intra cavity birefringent filter.

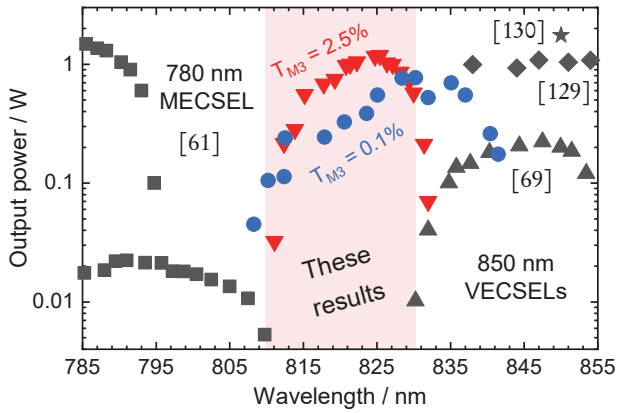

Figure 6.7 Wavelength tuning with a 2 mm thick intra cavity birefringent filter and T_{M3} = 2.5% outcoupling mirror at P_{abs} = 11.5 W. Reproduced from [P2], with the permission of OSA Publishing.

6.3.4 Thermal resistance

The thermal resistance of $R_{th} \sim 4.09\,\mathrm{K/W}$ was determined via spectral shift measurements, $\Delta\lambda/\Delta P_{diss} = 0.45\,\mathrm{nm/W}$ and $\Delta\lambda/\Delta T = 0.11\,\mathrm{nm/K}$ as plotted in Fig. 6.8.

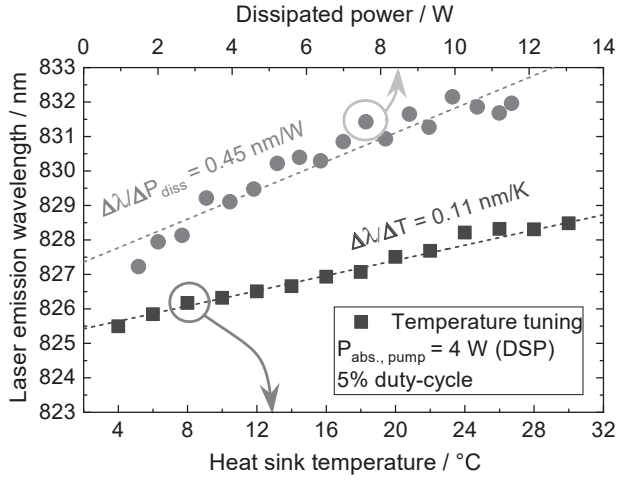

Figure 6.8 Spectral shift measurements with the dissipated power (grey dots) and heat sink temperature (dark grey squares) of the 825 nm MECSEL. Reproduced from [131].

6.3.5 Thermal lensing and its effect on the beam quality

To make a conclusion about the beam quality of the MECSEL, its beam profile and M^2 value was investigated in cavity 2. Here, a Thorlabs CCD beam profile camera BC106N-VIS with a resolution of 1360 x 1024 pixels was positioned behind M1. The camera position, and therefore the distance between the camera and M1 was fixed to make sure not to have any influences on the beam profile that was given by the camera position. Compared with the slightly elliptical beam profile at low pump power $P_{\mathrm{abs}} = 3.4\,W$ in Fig. 6.9, the beam profile became smaller and more circular once a higher pump power was set. Most likely, this is a thermal effect because the change disappears if the gain membrane is optically pumped with a 5% duty cycle. The observed change in size and shape can be at least attributed to the growing pump mode area with higher power as the pump beam owns a Gaussian power distribution.

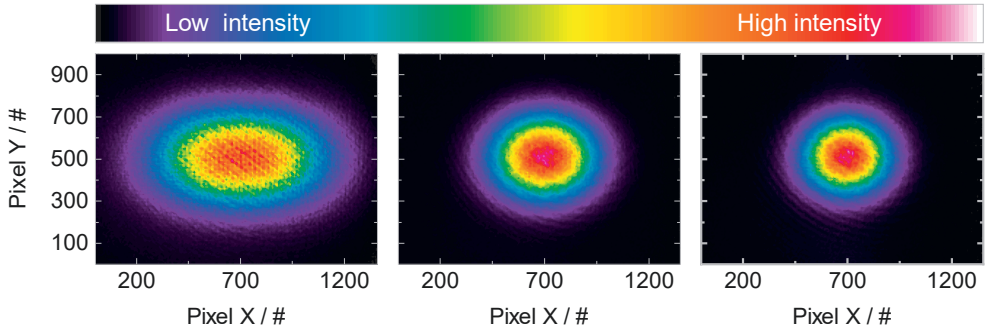

Figure 6.9 Beam profile measured at 3.4 W (left), 6.8 W (center), and 10.2 W (right) absorbed pump power. By increasing the pump power, the beam profile at a fixed position turned into a smaller and more circular spot. Reproduced from [P2], with the permission of OSA Publishing.

On the other hand, a nonuniform pump power distribution leaves a temperature gradient within the MECSEL-heat spreader sandwich behind. Based on the thermo-optical effect, the refractive index changes with the temperature, which creates a refractive index gradient. Hence a thermal lens [64] could be most likely setting in [65, 132]. Although it cannot be discriminated between how much contribution to the thermal lens comes from the heat spreaders and the gain medium, the thermal lens from the gain medium seemed to be dominating as the gain medium was significantly absorbing the pump light in contrast to the heat spreaders [65]. It is also a fact

that semiconductors possess thermo-optical coefficient values of up to two orders of magnitude higher than dielectric materials.

Subsequently, M^2 measurements were performed at varying absorbed pump power as plotted in Fig. 6.10c for both, sagittal and tangential planes. The divergence angle decreases from 2.8° to 1.2° in sagittal, and from 2.3° to 1.0° in tangential plane as shown in Fig. 6.10b. In turn, the beam waist diameter increases by 40 ± 5 µm. Furthermore, the beam waist position shifts by ~ 5 mm probably because the dioptric power of the thermal lens and hence its focal length is changing.

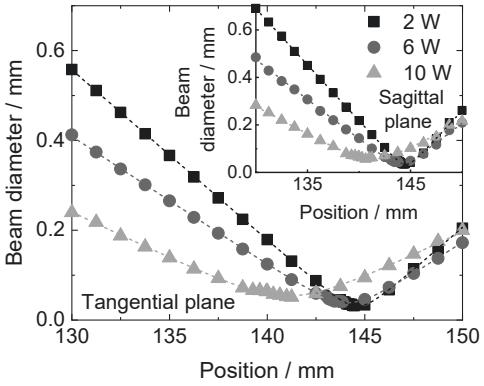

(a) M^2 measurements at varying absorbed pump power from 2 W to 10 W in tangential plane. The inset illustrates the behavior in sagittal plane.

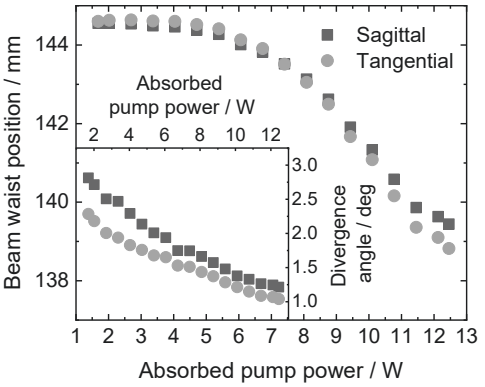

(b) Spatial shift of the beam waist with absorbed pump power. Inset: Divergence angle plotted versus absorbed pump power.

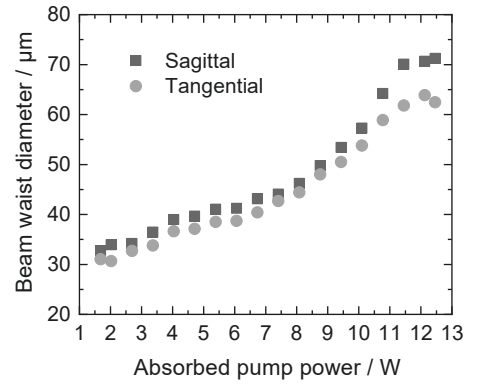

(c) Beam waist diameter at varying absorbed pump power from 2 W to 10 W in tangential and sagittal plane.

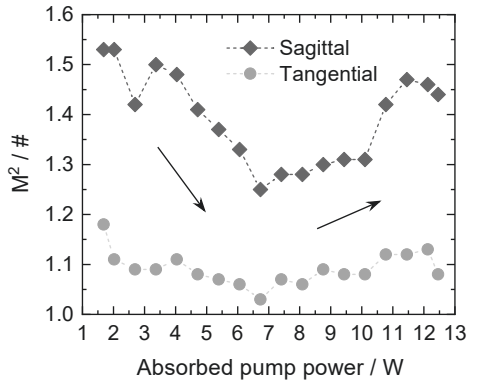

(d) M^2 values. The M^2 value decreases at moderate absorbed pump power < 7 W and increases if the absorbed pump power exceeds 7 W.

Figure 6.10 Beam diameter, beam waist positions, divergence angles, and beam waist diameter obtained from the M^2 measurement in cavity 2. Reproduced from [P2] and [131].

Figure 6.10d illustrates how the M^2 value centered around 1.5, was affected by the superposition of both effects, thermal lensing and the saturation of the pump beam. As expected, rising up the absorbed pump power to ~ 7 W induced a stronger thermal lens and therefore, the M^2 values dropped. At higher pump power level above 7 W, the high temperature area of the gain membrane could grow, which effectively could mean a reduction of the thermal gradient and the M^2 value increased.
In order to estimate the dioptric power of the thermal lens, a ray transfer matrix algorithm [133] for a Gaussian beam was used to simulate the mode diameter within the cavity. It should be additionally considered that our approach did not include any higher-order transversal modes and therefore holds only true for fundamental transversal modes [132]. First, the mode diameter was simulated without a lens inside the cavity. This is exemplarily shown along the tangential plane in Fig. 6.11. By immersing a thin biconvex lens with a given focal length directly behind the membrane-SiC heat spreader sandwich in the simulation, the effect of the lens on the beam divergence angle can be seen. Fig. 6.11 exemplarily shows how the intra cavity beam changes by the focussing effect of the thin lens with a focal length of 200 mm. The beam waist diameter grew from ~ 0.13 mm to $\sim$ 0.15 mm while the beam divergence angle in the cavity position between 250 mm and 500 mm decreased by a factor of ~ 0.85.

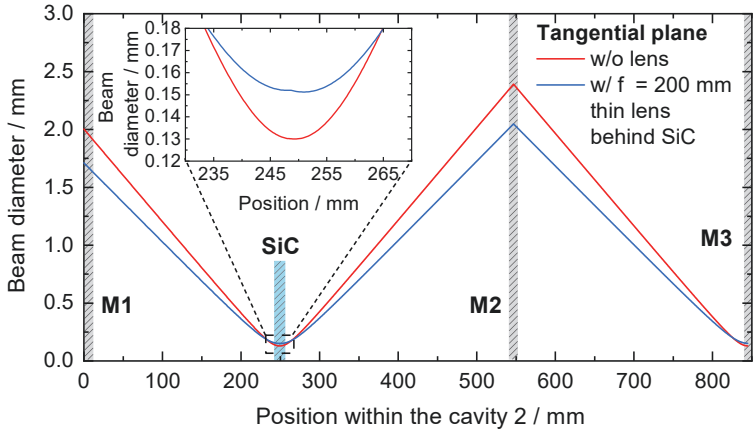

Figure 6.11 Simulated beam diameter within the cavity 2 in tangential plane for a laser emission wavelength of 825 nm. The total thickness of the SiC heat spreaders corresponds to 0.7 mm. The membrane has been neglected in the simulation. An enlarged view around the beam waist position is shown in the inset. It shows how the beam waist diameter grows by the focussing f = 200 mm lens placed behind the SiC heat spreader.

Since the mode diameter is nearly linearly proportional for larger distances to the gain element, it was considered that the beam divergence angle of the internal and the external beam changes in the same way by the same factor. This factor was calculated by the M^2 measurement data, using the beam divergence at threshold as a reference.

Figure 6.12 shows the outcome of the calculation. A trend that the dioptric power of the thermal lens increases with the absorbed pump power can be seen. Saturation to about 11 m^{-1} occured, when the absorbed pump power is set over 10 W. From these observations, it becomes again questionable whether there is a loss of the thermal gradient responsible for this saturation setting in. The values along both propagation planes are almost the same, which could mean that the thermal lens corresponds to a focussing lens with a uniform shape.

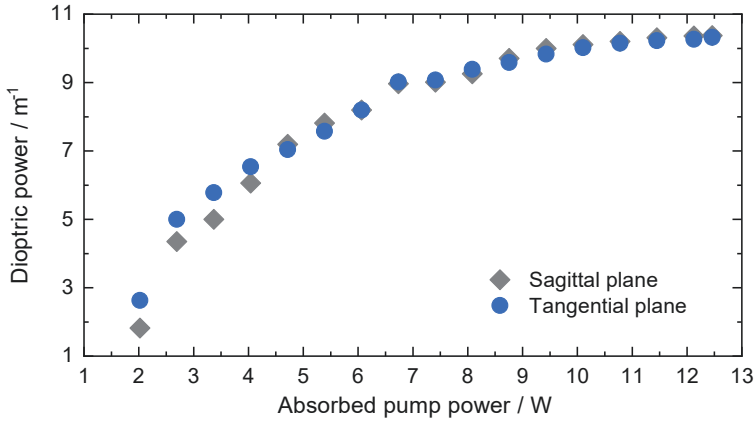

Figure 6.12 Thermal lens dioptric power from the ray matrix calculations based on the experimental data. Reproduced from [P2], with the permission of OSA Publishing.

Although there is an interplay of many various thermal effects, and the origin of the thermal lens cannot be exactly determined, there is at least a way to scrutinize whether the thermal lens is attributable to the refractive index gradient within the membrane. For a Gaussian pump beam, it was assumed that 87% of the heat was within the FWHM as proposed by Gordon et al. and therefore the refractive index variation could be described as a parabolic function around the beam center [64]. The temperature rise was obtained from spectral shift measurements, from the thermal resistance $R_{\mathrm{th}} = 4.09\,\mathrm{K/W}$. Thus, very close to thermal rollover, the temperature rise was approximately equal to $\Delta T = 46.83\,\mathrm{K}$. For simplicity, the thermo-

optical coefficient of GaInP $\mathrm{d}n/\mathrm{d}T \sim (2.0 \pm 0.3) \cdot 10^{-4}\,\mathrm{K}^{-1}$ [134] was taken into account and the dioptric power of the thermal lens was estimated as $(8.4 \pm 2.2)\,\mathrm{m}^{-1}$. This calculated value is in the same order of magnitude as the results plotted in Figure 6.12.

6.4 Conclusion

High-power operation was demonstrated in an 825 nm emitting MECSEL with SiC heat spreaders and at a heat sink temperature of $T_{\mathrm{hs}} = 20°\mathrm{C}$. Here, the cavity and the pump mode diameter was increased which had doubled the output power to 1.4 W. The used pump diameter was about 209 µm. Since this value was low compared to what had been typically used in VECSELs, the pump diameter can be further increased. Also, the gain membrane with nine QWs only, was relatively thin about $\sim 490\,\mathrm{nm}$. A gain membrane with more QWs can be grown at this wavelength in the future to further increase the output power. Also, several membranes can be directly stacked on top of each other to increase the gain volume. A heat spreader inbetween can be supportive for the thermal management.
In addition, investigations on the beam quality were presented. The beam profile became more circular and smaller once the membrane was pumped at higher power at cw operation. Attributable to this effect is the growing Gaussian pump mode area. However, the beam profile change became less prominent when the membrane was pumped at a 5% duty cycle. For this reason, thermal lensing was most likely setting in. This had not much affected the M^2 value, and the beam quality with an M^2 value < 1.6 remained excellent. In the future, it can be investigated how different pump spot diameters, mode ratios, heat spreader materials and thicknesses affects thermal lensing [65].

7 QUANTUM DOT MECSEL AT 1500 NM

The 1.5 µm wavelength region is covered by the InP material system yet lacks of suitable DBR materials with a specific refractive index contrast and thermal conductivity. This considerably makes it difficult to realize VECSELs with a monolithically integrated DBR. The situation becomes even clearer if one compares the refractive index contrast between 1 µm and 1.5 µm DBR materials.
Unlike AlAs/GaAs DBRs near 1 µm with $\sim$ 25 DBR pairs and a refractive index contrast of about 0.7 [135], the refractive index contrast of common DBR materials near 1.5 µm is much lower. To be more specific, between an InAlAs/InGaAlAs pair the refractive index contrast is only 0.3, and between an InP/InGaAsP pair 0.27 [136]. This has lead to at least 40 DBR pairs to achieve a sufficient high reflectivity of over 99.5%. Because the thickness of the DBR and the gain structure typically scale with the design emission wavelength, the VECSEL structures become so thick and tend to be more fragile to crack due to internal structural tensions.
InP VECSELs with a monolithically integrated DBR have been demonstrated earlier [137, 138]. These devices have provided only 140 mW output power at room temperature operation [139]. The thermal resistance has been reported to be as high as 470 K/W. To benefit from the higher refractive index contrast between amorphous silicon and silicon nitride, hybrid metal-dielectric mirrors soldered on different types of heat spreaders such as SiC or diamond have been implemented [140]. A hybrid metal-metamorphic mirror with 15 GaAs/AlAs DBR pairs has been integrated. Although the refractive index contrast is lower than in the hybrid metal-dielectric mirror, its higher thermal conductivity has lead to a better thermal resistance ($R_{\mathrm{th}} =$ 34 K/W) in VECSELs. The output power has been limited to 77 mW with this approach. Furthermore, VECSELs with GaInAsN/GaAs QWs and 29.5 AlAs/GaAs DBR pairs grown on a GaAs substrate has provided 80 mW output power [141].
Only high power ($>$ 3.65 W) [142] 1.5 µm emitting VECSELs could be realized if the gain structure and the DBR have been grown separately on two different substrates,

InP and GaAs; and afterwards combined via wafer-fusion [92, 143–147].
However, the next step of simplification would be to completely avoid the DBR, which can in addition provide a better thermal management and wavelength versatility. By this, it is possible to use more cost-effective heat spreaders such as SiC as is the case in the MECSEL. In this chapter, we demonstrate such a simplification as a MECSEL with InAs/InP QD layers for an emission wavelength of 1.5 µm. The results have been published as P3.

7.1 Gain membrane

The MECSEL structure was fabricated by gas source molecular beam epitaxy (GSMBE) at the University of Rennes. First, a 100 nm thick InGaAs etch stop layer was deposited on a 300 µm thick (311)B InP substrate. Afterwards, the gain structure was grown. It was composed of 20 InAs/InP QD layers with a layer thickness of 5 nm. The InAs/InP QD layers were separated by 15 nm thick GaInAsP barrier layers and equally distributed in four groups with InP cladding layers. Furthermore, the structure was optimized for single-side pumping to have a homogeneous charge carrier distribution such that the back side GaInAsP barrier layers were thicker as can be seen in Fig. 7.1 and Fig. 7.3.

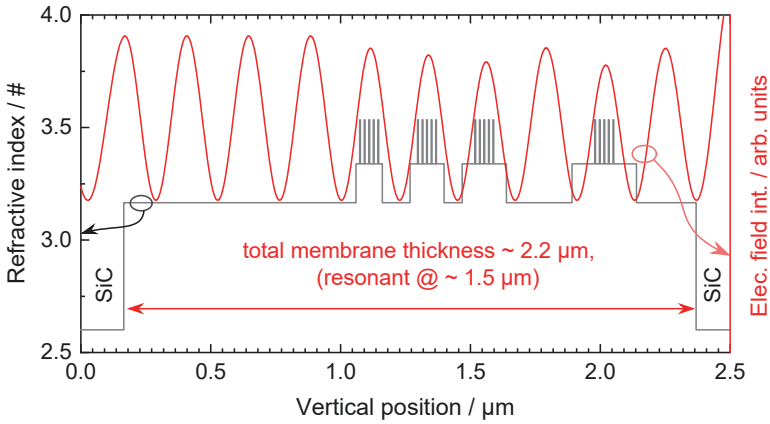

Figure 7.1 T-matrix simulation of the electric field distribution (red lines) and refractive index (grey lines) along the asymmetric QD MECSEL structure.

From the front to the back side of the structure, the total thickness of the absorbing barrier layers were thus, 90 nm, 120 nm, 160 nm, and 240 nm. All the QD layer

groups were arranged near the antinodes of the electric standing wave formed in a resonant 2.5 λ sub-cavity. As mentioned, the InP cladding layer between the two later pumped QD layer packages was about 260 nm thick which was more than two times thicker than the other cladding layers in these structures. The fourth out of five antinodes of the sub-cavity was left out and the fourth QD layer package was positioned to the fifth antinode of the standing wave field as illustrated in Fig. 7.1. The gain region was identical to the 1.5 µm QD VECSEL. More details about the gain region and growth can be found in [92].

7.1.1 Photoluminescence before and after processing

As a pre-characterization, a PL spectrum of the unprocessed structure was measured at room temperature conditions and plotted in Fig. 7.2. The PL maximum was centered at around 1536 nm and a FWHM of ∼ 142 nm. After the substrate was removed, and the gain membrane was bonded between two 350 µm thick 4H SiC heat spreader pieces, the QD layers were most likely less compressively strained than the unprocessed structure, such that the PL maximum shifted towards shorter wavelengths to 1467 nm with a FWHM of ∼ 160 nm. Furthermore, a shoulder on the shorter wavelength side of the PL maximum can be seen at 1300 nm, which can be attributable to the GaInAsP barrier layers that have a band gap energy at 1.18 µm.

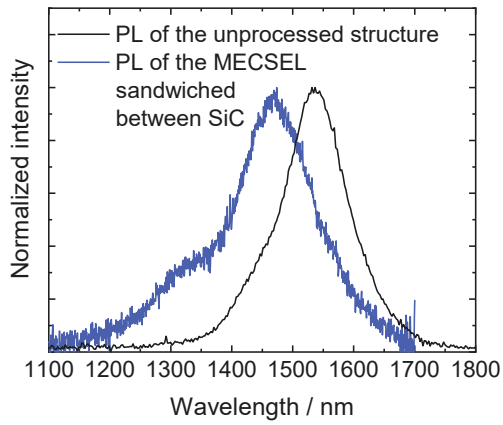

Figure 7.2 PL spectrum of the QD MECSEL structure before and after processing.

7.2 Experimental setup

Figure 7.3 shows a schematic drawing of the setup. The membrane-heat spreader sandwich was mounted into a copper heat sink mount. Water set at 19 °C flowed through the mount, and cooled the membrane. Output power, wavelength tuning,

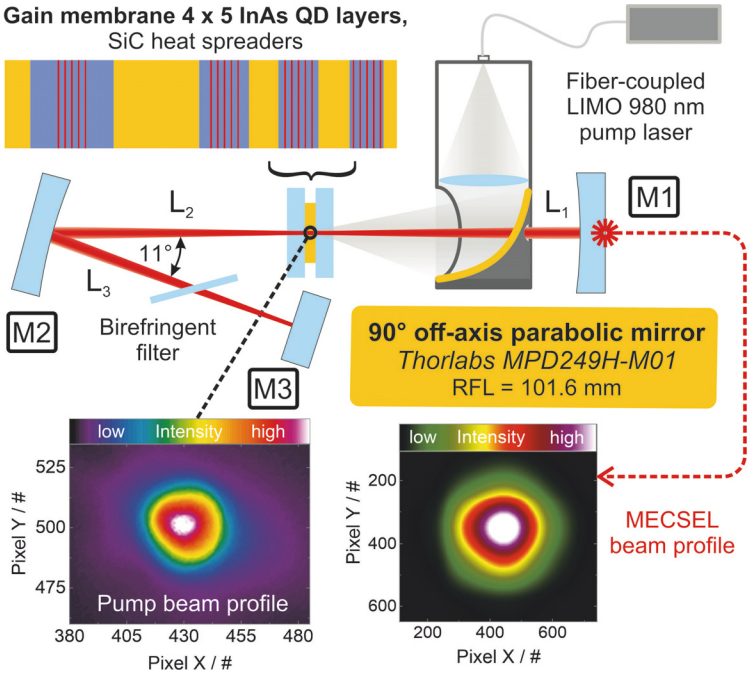

Figure 7.3 Schematic drawing of the 1.5 µm QD MECSEL. Using a 90° off-axis parabolic mirror with a protected gold coating, the beam profile of the pump beam focused onto the membrane is nearly circular as can be seen in the inset. Reproduced from [P3], with the permission of AIP Publishing.

and thermal resistance measurements were performed in a V-cavity. It was formed by two plano-concave mirrors M1 and M2 ($r = 200\,\text{mm}$ and $R > 99.8\%$), and a plane outcoupling mirror M3. The distances of M1 and M2 to the membrane were adjusted to $L_1 = 195\,\text{mm}$ and $L_2 = 199\,\text{mm}$. M3 was aligned under a folding angle of 11° to a distance of $L_3 = 199\,\text{mm}$ to M2. In this cavity configuration, the simulated cavity mode diameter at the membrane resulted to be about 200 µm.

The membrane was barrier-pumped at 980 nm by a LIMO diode laser, which was coupled into a multi-mode fiber with 200 µm core diameter and a numerical aperture of 0.22. The end of the fiber was connected to a set of aluminum tubes which included a plano-convex lens ($f = 100\,\text{mm}$) to collimate the pump beam. After collimation, the beam had a diameter of about 50 mm, and fell onto a 90° off-axis parabolic mirror (from Thorlabs MPD249H-M01) [21, 52] with a diameter of 50.8 mm. The area of the parabolic mirror was nearly fully covered by the beam. With a reflected focal length of 101.6 mm, the pump beam was focused onto a diameter of

360 µm. The main benefit of this pumping scheme was the small pump angle less than 15°. This allowed the creation of a nearly circular pump spot in the focus with $D_{sag}/D_{tan} > 0.96$ as calculated.
A beam profile can be seen in the inset of Fig. 7.3. The parabolic mirror, coated with protected gold, had a reflectivity of $R_{980nm} > 98\%$ at the pump wavelength. Furthermore, the parabolic mirror had a hole with a diameter of 3 mm at the center, oriented towards the MECSEL cavity axis of M1 and M2. Therefore, the parabolic mirror did not cover the MECSEL intra cavity beam, which was narrower than the hole. Pump beam losses introduced by the hole were calculated to be less than 1%; and were thus insignificant.

7.3 Results

7.3.1 Power performance

The total output power from all transmitted beams through M1, M2, and M3 was taken into account and is plotted in Fig. 7.4 with an HR emission spectrum at $P_{abs} = 21\,W$ shown as an inset. Lasing set in at a threshold of $P_{abs} \sim 4.7\,W$. A maximum output power of $\sim 320\,mW$ was achieved with a $R_{M3} = 99\,\%$ outcoupling mirror.

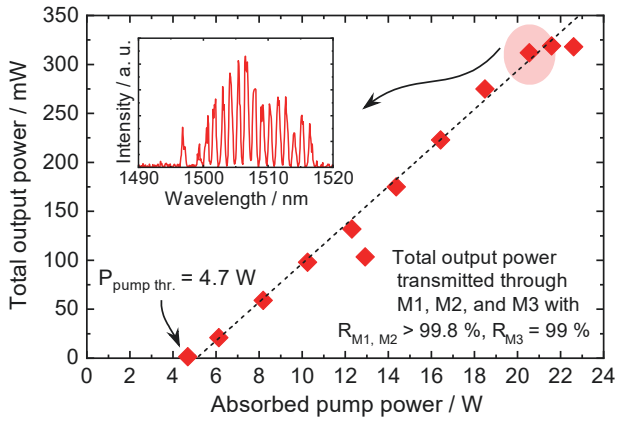

Figure 7.4 Total output power of the 1.5 µm QD MECSEL measured at all transmitted beams through M1, M2, and M3 in the V-cavity. The inset shows an HR spectrum taken at 21 W absorbed pump power. Reproduced from [P3], with the permission of AIP Publishing.

7.3.2 Thermal resistance

To determine the thermal resistance of the QD MECSEL, spectral shift measurements was performed. Here, the laser emission wavelength variation with the dissipated power was obtained as $\sim 0.16\,\mathrm{nm/W}$ as shown in Fig. 7.5. For the spectral shift with the heat sink temperature, the pump power was adjusted to $P_{\mathrm{abs}} = 12.3\,W$. The pump beam was blocked after each measurement step to avoid pump heat introduced to the gain membrane. By this, the spectral shift with the heat sink temperature resulted as $\sim 0.07\,\mathrm{nm/K}$. With Eq. 5.1, the thermal resistance was approximately $2.3\,\mathrm{K/W}$. By assuming that thermal roll-over sets in at $P_{\mathrm{abs}} = 22\,W$, the maximum operational temperature was about 70°C. In comparison with the InGaAlAs/InP QW-based MECSEL [45], the value for the thermal resistance was in the same order of magnitude. A comparison can be also made with earlier VECSELs emitting at 1.5X µm [136, 138, 140]. For a VECSEL with a monolithically integrated DBR, made of 48 InP/InGaAsP pairs, the thermal resistance was reported as $470\,\mathrm{K/W}$. This high value orginated from the small thermal conductivity values of $\sim 68\,\mathrm{W/m{\cdot}K}$ for InP [148], and $\sim 7\,\mathrm{W/m{\cdot}K}$ for InGaAsP [149] as well as the low refractive index contrast of $\Delta n = 0.27$ [136]. Another approach used a hybrid metal-metamorphic mirror with 15 GaAs/AlAs DBR pairs completed with Au. Here, a thermal resistance of $R_{\mathrm{th}} = 34\,\mathrm{K/W}$ was measured [140].

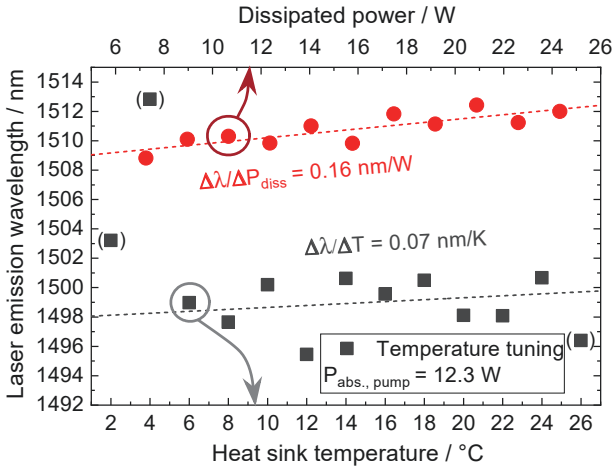

Figure 7.5 Spectral shift of the QD MECSEL with the dissipated power and the heat sink temperature.

7.3.3 Spectral characteristics

Wavelength tuning measurements were conducted by rotating a 1.5 mm thick birefringent filter inside the V-cavity. This birefringent filter had a free spectral range of 180 nm, which was large enough to tune the MECSEL emission wavelength continuously over its bandwidth. As can be seen in Fig. 7.6, the output power measured behind the outcoupling mirror M3 is plotted against the emission wavelength. While a tuning range from 1474 to 1519 nm was obtained with an $R_{\mathrm{M3}} = 99\%$ outcoupling mirror, the MECSEL was tunable over 86 nm (which corresponded to 11.5 THz) with an HR outcoupling mirror. The earlier reported VECSEL with the same gain structure, which was cooled by an intra cavity diamond heat spreader had a tuning range of 80 nm [92, 147]. Here, the QD MECSEL showed a better tuning range which was is most likely attributable to the use of dielectric laser mirrors that typically have a better quality HR band than semiconductor DBRs.

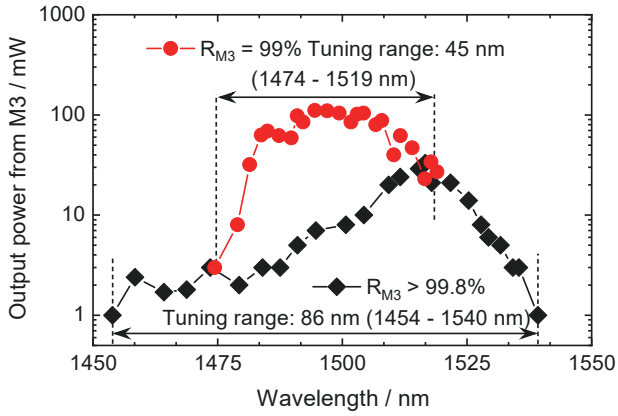

Figure 7.6 Output power plotted versus emission wavelength, which is tuned by rotating a 1.5 mm thick birefringent filter set at Brewster's angle. The measurement is performed at P_{abs} = 16.4 W. Reproduced from [P3], with the permission of AIP Publishing.

7.3.4 Beam quality

The QD MECSEL possessed an excellent beam quality with an M^2 value better than 1.05 in both, tangential and sagittal axis as shown in Fig. 7.7.

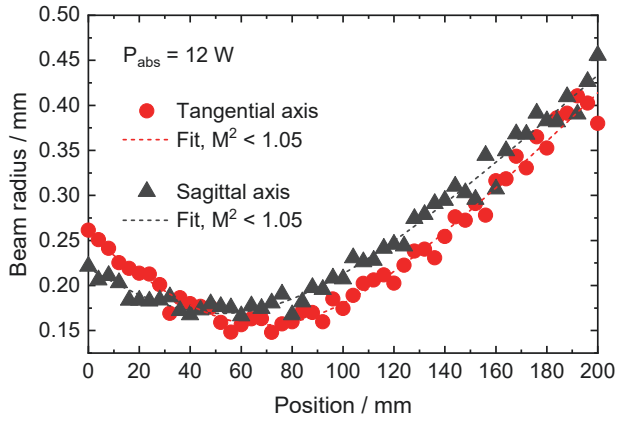

Figure 7.7 M^2 measurement of the QD MECSEL along both tangential and sagittal axis using a dual scanning-slit BP209-IR/M beam profiler and a Thorlabs M2 M2MS measurement system.

7.3.5 Degree of linear polarization

For a V-cavity, the intra cavity beam was not only reflected under normal incidence at the laser mirrors M1 and M3 but was also reflected under half of the folding angle at M2. If one considers the Fresnel law for the reflectance at an incident angle unequal to zero, the reflectance differs between the s- and p-polarized light. Consequently, a V-cavity would favor a dominating polarization axis. To understand this effect, the degree of linear polarization (DOP) of the MECSEL was characterized in a linear cavity as illustrated in the photograph in Fig. 7.8. For the linear cavity consisting of M1 and M2, was used. The mirror distances were about $L_1 = L_2 = 197$ mm. There were no intra cavity elements placed inside the cavity. First, it was tested out whether the polarization of the MECSEL switched between two orthogonally polarization axis while increasing the pump power. For this, an ultra broad band wire grid polarizer from Thorlabs (WP25M-UB) with an extinction ratio of 1000:1 was positioned behind M2. The MECSEL output power transmitted through the wire grid polarizer was measured with the transmission axis fixed at 0° (p-polarization axis) and afterwards at 90° (s-polarization axis).
As plotted in Fig. 7.9a, the MECSEL was s-polarized. The input-output power curve increased linearly throughout the entire measurement and no polarization switching was detected. During the input-output power measurement, emission spectra was simultaneously recorded. The emission wavelength was nearly identical in both

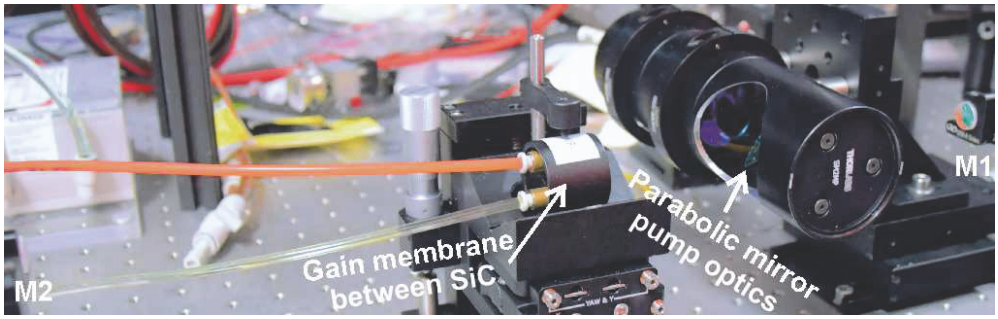

Figure 7.8 Photograph of the 1.5 µm QD MECSEL setup with a linear cavity used to characterize the degree of linear polarization. The linear cavity does not contain any intra cavity elements. An aluminum tube is connected with the fiber-end of the diode pump laser system, and placed between the MECSEL gain element and M1. The tube includes the collimation lens and the 90° off-axis parabolic mirror.

polarizations, centered at 1.5 µm, as exemplarily shown in Fig. 7.9b at 16.4 W absorbed pump power. The longitudinal modes were about 5 nm apart, which was larger than the FSR of the intra cavity heat spreaders and could possibly originate from a beat note effect in a shorter cavity. An additional longitudinal mode oscillating in the p-polarization around ∼ 1498 nm was measurable.

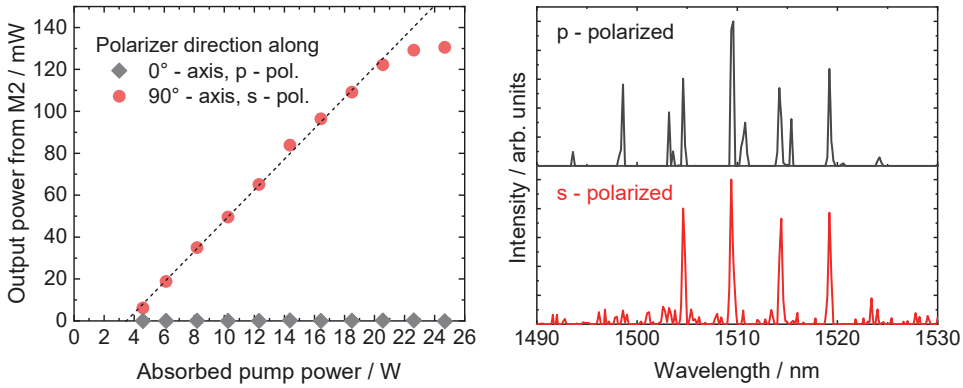

(a) Measured output power transmitted through M2 and a wire-grid polarizer.

(b) Normalized spectra of both polarization axis taken at 16.4 W absorbed pump power.

Figure 7.9 Output recorded at two orthogonal angles of the polarizer transmission axis from M2. Reproduced from [P3], with the permission of AIP Publishing.

Finally, the wire grid polarizer was rotated over 360° to determine the DOP for P_{abs} from 5 W to 26 W. With the measurement data in Fig. 7.10a, the minimum and maximum power, P_{min} and P_{max} were averaged. The DOP in Fig. 7.10b was determined

by $DOP = (P_{max} - P_{min})/(P_{max} + P_{min})$.

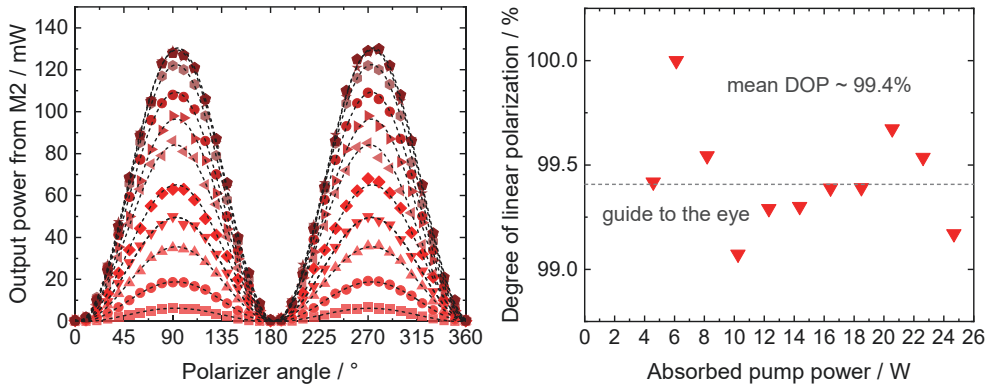

(a) Measured output power transmitted through M2 and a wire-grid polarizer rotated over a full cycle from 5 W to 26 W absorbed pump power.

(b) High degree of linear polarization of > 99.4 ° of the 1.5 µm QD MECSEL, calculated from the data in Fig. 7.10a.

Figure 7.10 Polarization investigations of the QD MECSEL. Reproduced from [P3], with the permission of AIP Publishing.

A mean DOP of ∼ 99.4% corresponds to a polarization extinction ratio of > 22 dB and is a typical value for VECSELs [9, 150, 151]. What supports this high DOP in this gain membrane here is most likely the QD anisotropy. This has also been recently reported in VCSELs with the same 1.5 µm InAs/InP QD layer structure [152].

7.4 Conclusion

The thermal and spectral characteristics of a QD MECSEL providing more than 320 mW output power at room temperature operation were presented in this chapter. The MECSEL emitted around 1.5 µm, a wavelength which is in particular difficult for VECSELs because the thermal conductivity of the monolithically grown DBR is low. Compared with earlier InP VECSELs, the thermal resistance was more than 15 times lower, about $R_{th} = 2.3$ K/W. The MECSEL had the same gain structure with 5×4 InAs/InP QD layers, as the earlier wafer-fused VECSEL [147]. Although the cooling conditions in the MECSEL were worse as the gain membrane was cooled by SiC instead of diamond, it provided a broader wavelength coverage of 86 nm. The slight improvement of about 6 nm could be partly attributable to the use of dielectric mirrors, which had a wider reflection band than semiconductor DBRs. But the

increased integrated bandwidth could contribute to this broader tunability as well as it was proposed by Yang et al. [41]. To conclude, the MECSEL is an alternative solution besides wafer-fusion to address those emission wavelengths at which the DBR becomes too difficult to realize, from 1.3 µm to 1.5 µm, for instance.

8 SUMMARY AND FUTURE WORK

This work aimed at advancing MECSEL technology by working on several aspects related to thermal management, wavelength extension, and pumping architectures. It has been found that the double-side heat extraction from the semiconductor gain membrane leads to a thermal benefit of about a factor two compared to the single-side heat extraction. The better thermal management allows the use of SiC or sapphire heat spreaders, which both have a lower thermal conductivity but are more advantageous in cost than diamond. Power scaling and emission to new wavelengths are demonstrated. The results are summarized alongside with the state-of-the-art MECSEL work in Fig. 8.1.

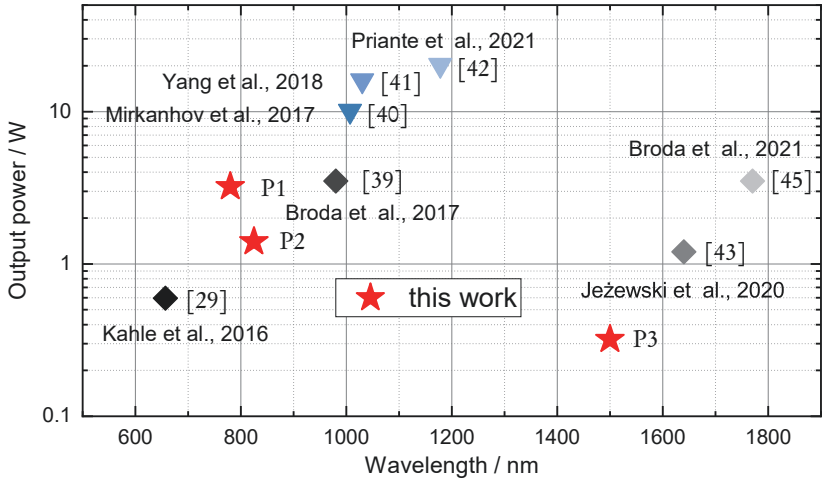

Figure 8.1 Overview of MECSEL results showing the maximum output power reached at different wavelengths. Results with diamond heat spreaders are illustrated as filled diamonds, with SiC heat spreaders as filled triangles. MECSEL results in this work are plotted as filled stars.

1. Similar to classical solid-state lasers, the MECSEL is compatible with double-side pumping, a way to distribute heat and charge carriers axially more homogeneously within the gain membrane. Double-side pumping (DSP) of a

$\sim$ 500 nm thick gain membrane demonstrated in [P1] has lead to a threshold of 0.69 W, which is 0.1 W lower than achieved with single-side pumping (SSP). A differential efficiency of 34.4% has been achieved with DSP, and 31.9% with SSP. The thermal benefit of DSP was investigated by the thermal resistance, which can be lowered from 5.9 K/W (SSP) to 5.36 K/W (DSP). As can be seen in Fig. 8.1, a $>$ 3.2 W high-power MECSEL at 780 nm has been realized. Because the gain membrane is only $\sim$ 500 nm thick, heat is dissipated homogeneously from both sides of the heat spreaders and the way of pumping does not matter much. Here, our FEM thermal model suggests that the thermal benefit from DSP becomes more relevant for gain membranes thicker than 1 µm.

2. The power scalability of MECSELs has been simulated for various types of heat spreader materials, thicknesses, pump beam shapes, pumping approaches, and pump diameters by the FEM. This allows an estimation of the optimal heat spreader and pumping conditions for the realization of high-power MECSELs in the future. When considering the thermal conductivity of gain membranes within the 5 W/m·K to 50 W/m·K regions, it has been found that the membrane thermal conductivity value has only a small effect on the membrane temperature. This could be a possible explanation why the results simulated for a MECSEL emitting in the 800 nm wavelength region are in a good agreement with other experimental MECSEL results from this work and the literature.

3. Initially, a pump spot diameter in the size of about 100 µm has been used to pump our SiC-cooled gain membranes. A larger pump spot diameter of 209 µm has enabled us to pump the gain membrane at more than twice pump power. Consequently, this has doubled the maximum output power of an 825 nm-emitting MECSEL to 1.4 W (see Fig. 8.1). At this point, it needs to be emphasized that an 825 nm-emitting MECSEL that covers a spectral gap of semiconductor disk lasers between 810 nm and 830 nm has been realized in this work. To further advance the pumping efficiency by a more circular pump spot, a parabolic mirror pumping has been implemented which allows a circular pump spot. This avoids the need for beam shaping optics. Furthermore, the formation of a thermal lens in a MECSEL has been suspected to take place for focussing the MECSEL beam. The MECSEL beam divergence angle

decreases with the power of a Gaussian pump beam. It has been found that the thermal lens does not affect the M^2 value much as the beam divergence angle decreases while the beam waist grows.

4. Towards wavelength extension, the MECSEL technology was applied to a wavelength around 1.5 µm, at which no monolithic DBRs with a good quality are available. A MECSEL with an InAs/InP QD-based gain membrane provided over 320 mW output power and 86 nm tuning range. The MECSEL is a technology which allows a larger wavelength coverage of semiconductor disk lasers with a thermal benefit. For instance, the thermal resistance of the 1.5 µm QD MECSEL is only about 2.3 K/W. This value is more than two orders of magnitude lower than in conventional semiconductor disk lasers with a monolithically integrated DBR.

As future work, MECSEL research can be continued in two ways. First, the MECSEL technology can be applied to extend the wavelength coverage of semiconductor disk lasers, particularly in the DBR critical wavelength regions between 1.3 µm and 1.8 µm. For power scaling, membranes thicker than 1 µm for large gain can be pumped from two sides by fiber-coupled diode lasers with a flat super-Gaussian beam profile and the optimal pump spot size. For low-cost MECSELs, sapphire heat spreaders can be considered with a cheap laser diodes for pumping. To increase the efficiencies in general, multi-pass pumping can be applied.

REFERENCES

[1] T. H. Maiman. Stimulated Optical Radiation in Ruby. *Nature* **187** (1960), 493–494. DOI: 10.1038/187493a0.

[2] D. Huang, E. A. Swanson, C. P. Lin, J. S. Schuman, W. G. Stinson, W. Chang, M. R. Hee, T. Flotte, K. Gregory, C. A. Puliafito and J. G. Fujimoto. Optical coherence tomography. *Science* **254**, 5035 (1991), 1178–1181. DOI: 10.1126/science.1957169.

[3] A. Ashkin. Optical trapping and manipulation of neutral particles using lasers. *Proceedings of the National Academy of Sciences* **94**, 10 (1997), 4853–4860. DOI: 10.1073/pnas.94.10.4853.

[4] B. C. Barish and R. Weiss. LIGO and the Detection of Gravitational Waves. *Physics Today* **52**, 10 (1999), 44–50. DOI: 10.1063/1.882861.

[5] R. N. Hall, G. E. Fenner, J. D. Kingsley, T. J. Soltys and R. O. Carlson. Coherent Light Emission From GaAs Junctions. *Physics Review Letters* **9** (1962), 366–368. DOI: 10.1103/PhysRevLett.9.366.

[6] H. Soda, K.-I. Iga, C. Kitahara and Y. Suematsu. GaInAsP/InP Surface Emitting Injection Lasers. *Japanese Journal of Applied Physics* **18**, 12 (1979), 2329–2330. DOI: 10.1143/JJAP.18.2329.

[7] M. C. Amann. URL: https://www.wsi.tum.de/views/sub_group.php?group=Amann.

[8] N. Basov, O. Bogdankevich and A. Grasyuk. Semiconductor lasers with radiating mirrors. *IEEE Journal of Quantum Electronics* **2**, 9 (1966), 594–597. DOI: 10.1109/JQE.1966.1074111.

[9] J. V. Sandusky and S. R. J. Brueck. A CW external-cavity surface-emitting laser. *IEEE Photonics Technology Letters* **8**, 3 (1996), 313–315. DOI: 10.1109/68.481101.

[10] A. Giesen, H. Hügel, A. Voss, K. Wittig, U. Brauch and H. Opower. Scalable concept for diode-pumped high-power solid-state lasers. *Applied Physics B: Lasers and Optics* **58**, 5 (1994), 365–372. DOI: 10.1007/BF01081875.

[11] M. Kuznetsov, F. Hakimi, R. Sprague and A. Mooradian. High-power (> 0.5-W CW) diode-pumped vertical-external-cavity surface-emitting semiconductor lasers with circular TEM_{00} beams. *IEEE Photonics Technology Letters* **9**, 8 (1997), 1063–1065. DOI: 10.1109/68.605500.

[12] A. J. Kemp, G. J. Valentine, J.-M. Hopkins, J. E. Hastie, S. A. Smith, S. Calvez, M. D. Dawson and D. Burns. Thermal management in vertical-external-cavity surface-emitting lasers: finite-element analysis of a heatspreader approach. *IEEE Journal of Quantum Electronics* **41**, 2 (2005), 148–155. DOI: 10.1109/JQE.2004.839706.

[13] M. Guina, A. Härkönen, V.-M. Korpijärvi, T. Leinonen and S. Suomalainen. Semiconductor Disk Lasers: Recent Advances in Generation of Yellow-Orange and Mid-IR Radiation. *Advances in Optical Technologies* **2012** (2012), 19. DOI: 10.1155/2012/265010.

[14] E. Kantola, J.-P. Penttinen, S. Ranta and M. Guina. 72-W vertical-external-cavity surface-emitting laser with 1180-nm emission for laser guide star adaptive optics. *Electronics Letters* **54**, 19 (2018), 1135–1137. DOI: 10.1049/el.2018.6225.

[15] Z. L. Liau. Semiconductor wafer bonding via liquid capillarity. *Applied Physics Letters* **77**, 5 (2000), 651–653. DOI: 10.1063/1.127074.

[16] J. E. Hastie, C. W. Jeon, D. Burns, J.-M. Hopkins, S. Calvez, R. Abramb and M. D. Dawson. A 0.5 W, 850 nm $Al_xGa_{1-x}As$ VECSEL with intra-cavity silicon carbide heatspreader. *The 15th Annual Meeting of the IEEE Lasers and Electro-Optics Society*. **1**. 2002, 329–330. DOI: 10.1109/LEOS.2002.1134063.

[17] A. J. Maclean, A. J. Kemp, J.-M. Hopkins, J. E. Hastie, S. Giet, S. Calvez, M. D. Dawson, D. Burns, J.-Y. Kim, K.-S. Kim and T. Kim. An analysis of power scaling and thermal management in a 1060 nm VECSEL with a diamond heatspreader. *CLEO/QELS 2006*. 2006, 1–2. DOI: 10.1109/CLEO.2006.4628738.

[18] E. Kantola, T. Leinonen, S. Ranta, M. Tavast and M. Guina. High-efficiency 20 W yellow VECSEL. *Optics Express* **22**, 6 (2014), 6372–6380. DOI: 10.1364/OE.22.006372.

[19] E. J. Saarinen, J. Lyytikäinen, S. Ranta, A. Rantamäki, A. Sirbu, V. Iakovlev, E. Kapon and O. G. Okhotnikov. 750 nm 1.5 W frequency-doubled semiconductor disk laser with a 44 nm tuning range. *Optics Letters* **40**, 19 (2015), 4380–4383. DOI: 10.1364/OL.40.004380.

[20] A. Rantamäki, J. Rautiainen, J. Lyytikäinen, A. Sirbu, A. Mereuta, E. Kapon and O. G. Okhotnikov. 1 W at 785 nm from a frequency-doubled wafer-fused semiconductor disk laser. *Optics Express* **20**, 8 (2012), 9046–9051. DOI: 10.1364/OE.20.009046.

[21] C. M. N. Mateo, U. Brauch, H. Kahle, T. Schwarzbäck, M. Jetter, M. Abdou Ahmed, P. Michler and T. Graf. 2.5 W continuous wave output at 665 nm from a multi-pass and quantum-well-pumped AlGaInP vertical-external-cavity surface-emitting laser. *Optics Letters* **41**, 6 (2016), 1245–1248. DOI: 10.1364/OL.41.001245.

[22] S. Kaspar, M. Rattunde, T. Töpper, C. Manz, K. Köhler and J. Wagner. Semiconductor disk laser at 2.05 µm wavelength with < 100 kHz linewidth at 1 W output power. *Applied Physics Letters* **100**, 3, 031109 (2012), 031109. DOI: 10.1063/1.3675637.

[23] D. Pabœuf, P. J. Schlosser and J. E. Hastie. Frequency stabilization of an ultraviolet semiconductor disk laser. *Optics Letters* **38**, 10 (2013), 1736–1738. DOI: 10.1364/OL.38.001736.

[24] P. H. Moriya, R. Casula, G. A. Chappell, D. C. Parrotta, S. Ranta, H. Kahle, M. Guina and J. E. Hastie. InGaN-diode-pumped AlGaInP VECSEL with sub-kHz linewidth at 689 nm. *Optics Express* **29**, 3 (2021), 3258–3268. DOI: 10.1364/OE.416210.

[25] U. Keller. Recent developments in compact ultrafast lasers. *Nature* **424** (2003), 831–838. DOI: 10.1038/nature01938.

[26] B. Heinen, T.-L. Wang, M. Sparenberg, A. Weber, B. Kunert, J. Hader, S. W. Koch, J. V. Moloney, M. Koch and W. Stolz. 106 W continuous-wave output power from vertical-external-cavity surface-emitting laser. *Electronics Letters* **48**, 9 (2012), 516–517. DOI: 10.1049/el.2012.0531.

[27] M. Guina, A. Rantamäki and A. Härkönen. Optically pumped VECSELs: review of technology and progress. *Journal of Physics D: Applied Physics* **50**, 38 (2017), 383001. DOI: 10.1088/1361-6463/aa7bfd.

[28] Z. Yang, A. R. Albrecht, J. G. Cederberg and M. Sheik-Bahae. Optically pumped DBR-free semiconductor disk lasers. *Optics Express* **23**, 26 (2015), 33164–33169. DOI: 10.1364/OE.23.033164.

[29] H. Kahle, C. M. N. Mateo, U. Brauch, P. Tatar-Mathes, R. Bek, M. Jetter, T. Graf and P. Michler. Semiconductor membrane external-cavity surface-emitting laser (MECSEL). *Optica* **3**, 12 (2016), 1506–1512. DOI: 10.1364/OPTICA.3.001506.

[30] J. Piprek, T. Tröger, B. Schröter, J. Kolodzey and C. S. Ih. Thermal conductivity reduction in GaAs-AlAs distributed Bragg reflectors. *IEEE Photonics Technology Letters* **10**, 1 (1998), 81–83. DOI: 10.1109/68.651113.

[31] P. Zhang, R. Zhu, M. Jiang, Y. Song, D. Zhang and Y. Cui. Size effect caused significant reduction of thermal conductivity of GaAs/AlAs distributed Bragg reflector used in semiconductor disk laser. *Optics & Laser Technology* **96** (2017), 259–264. DOI: 10.1016/j.optlastec.2017.05.018.

[32] Y. Huo, C. Y. Cho, K. F. Huang, Y. F. Chen and C. C. Lee. Exploring the DBR superlattice effect on the thermal performance of a VECSEL with the finite element method. *Optics Letters* **44**, 2 (2019), 327–330. DOI: 10.1364/OL.44.000327.

[33] H. Kahle, C. M. N. Mateo, U. Brauch, R. Bek, M. Jetter, T. Graf and P. Michler. *The optically pumped semiconductor membrane external-cavity surface-emitting laser (MECSEL): A concept based on a diamond-sandwiched active region*. 2017. DOI: 10.1117/12.2252182.

[34] J. V. Moloney, J. Hader and S. W. Koch. Quantum design of active semiconductor materials for targeted wavelengths: a predictive design tool for edge emitters and OPSLs. *Proc. SPIE*. **6871**. 2008.

[35] V. Iakovlev, J. Walczak, M. Gębski, A. K. Sokoł, M. Wasiak, P. Gallo, A. Sirbu, R. P. Sarzała, M. Dems, T. Czyszanowski and E. Kapon. Double-diamond high-contrast-gratings vertical external cavity surface emitting laser. *Journal of Physics D: Applied Physics* **47**, 6 (2014), 065104. DOI: 10.1088/0022-3727/47/6/065104.

[36] H. Q. Le, S. Di Cecca and A. Mooradian. Scalable high-power optically pumped GaAs laser. *Applied Physics Letters* **58**, 18 (1991), 1967–1969. DOI: http://dx.doi.org/10.1063/1.105034.

[37] K. W. Su, S. C. Huang, A. Li, S. C. Liu, Y. F. Chen and K. F. Huang. High-peak-power AlGaInAs quantum-well 1.3-μm laser pumped by a diode-pumped actively Q-switched solid-state laser. *Optics Letters* **31**, 13 (2006), 2009–2011. DOI: 10.1364/OL.31.002009.

[38] Z. Yang, A. R. Albrecht, J. G. Cederberg and M. Sheik-Bahae. 80 nm tunable DBR-free semiconductor disk laser. *Applied Physics Letters* **109**, 2 (2016). DOI: 10.1063/1.4958164.

[39] A. Broda, A. Kuźmicz, G. Rychlik, K. Chmielewski, A. Wójcik-Jedlińska, I. Sankowska, K. Gołaszewska-Malec, K. Michalak and J. Muszalski. Highly efficient heat extraction by double diamond heat-spreaders applied to a vertical external cavity surface-emitting laser. *Optical and Quantum Electronics* **49**, 9 (2017), 287. DOI: 10.1007/s11082-017-1129-x.

[40] S. Mirkhanov, A. H. Quarterman, H. Kahle, R. Bek, R. Pecoroni, C. J. C. Smyth, S. Vollmer, S. Swift, P. Michler, M. Jetter and K. G. Wilcox. DBR-free semiconductor disc laser on SiC heatspreader emitting 10.1 W at 1007 nm. *Electronics Letters* **53**, 23 (2017), 1537–1539. DOI: 10.1049/el.2017.2689.

[41] Z. Yang, D. Follman, A. R. Albrecht, P. Heu, N. Giannini, G. D. Cole and M. Sheik-Bahae. 16 W DBR-free membrane semiconductor disk laser with dual-SiC heatspreader. *Electronics Letters* **54**, 7 (2018), 430–432. DOI: 10.1049/el.2018.0101.

[42] D. Priante, M. Zhang, A. Albrecht, R. Bek, M. Zimmer, C. Nguyen, D. Follman, G. Cole and M. Sheik-Bahae. Demonstration of a 20-W membrane-external-cavity surface-emitting laser for sodium guide star applications. *Electronics Letters* **57**, 8 (2021), 337–338. DOI: 10.1049/ell2.12008.

[43] B. Jeżewski, A. Broda, I. Sankowska, A. Kuźmicz, K. Gołaszewska-Malec, K. Czuba and J. Muszalski. Membrane external-cavity surface-emitting laser emitting at 1640 nm. *Optics Letters* **45**, 2 (2020), 539–542. DOI: 10.1364/OL.381531.

[44] A. Broda, B. Jeżewski, I. Sankowska, M. Szymański, P. Hoser and J. Muszalski. Growth and characterization of InP-based 1750 nm emitting membrane external-cavity surface-emitting laser. *Applied Physics B* **126**, 192 (2020). DOI: 10.1007/s00340-020-07544-y.

[45] A. Broda, B. Jeżewski, M. Szymański and J. Muszalski. High-Power 1770 nm Emission of a Membrane External-Cavity Surface-Emitting Laser. *IEEE Journal of Quantum Electronics* **57**, 1 (2021), 1–6. DOI: 10.1109/JQE.2020.3031305.

[46] S. W. Corzine, R. S. Geels, J. W. Scott, R.-H. Yan and L. A. Coldren. Design of Fabry-Perot surface-emitting lasers with a periodic gain structure. *IEEE Journal of Quantum Electronics* **25**, 6 (1989), 1513–1524. DOI: 10.1109/3.29288.

[47] M. Y. A. Raja, S. R. J. Brueck, M. Osinski, C. F. Schaus, J. G. McInerney, T. M. Brennan and B. E. Hammons. Resonant periodic gain surface-emitting semiconductor lasers. *IEEE Journal of Quantum Electronics* **25**, 6 (1989), 1500–1512. DOI: 10.1109/3.29287.

[48] M. Schmid, S. Benchabane, F. Torabi-Goudarzi, R. Abram, A. I. Ferguson and E. Riis. Optical in-well pumping of a vertical-external-cavity surface-emitting laser. *Applied Physics Letters* **84**, 24 (2004), 4860–4862. DOI: 10.1063/1.1760887.

[49] S.-S. Beyertt, M. Zorn, T. Kübler, H. Wenzel, M. Weyers, A. Giesen, G. Tränkle and U. Brauch. Optical in-well pumping of a semiconductor disk laser with high optical efficiency. *IEEE Journal of Quantum Electronics* **41**, 12 (2005), 1439–1449. DOI: 10.1109/JQE.2005.858794.

[50] C. M. N. Mateo, U. Brauch, T. Schwarzbäck, H. Kahle, M. Jetter, M. Abdou Ahmed, P. Michler and T. Graf. Enhanced efficiency of AlGaInP disk laser by in-well pumping. *Optics Express* **23**, 3 (2015), 2472–2486. DOI: 10.1364/OE.23.002472.

[51] S. C. Tidwell, J. F. Seamans, M. S. Bowers and A. K. Cousins. Scaling CW diode-end-pumped Nd:YAG lasers to high average powers. *IEEE Journal of Quantum Electronics* **28**, 4 (1992), 997–1009. DOI: 10.1109/3.135219.

[52] M. Herper, A. van der Lee, J. Kolb, S. Gronenborn, H. Moench and P. Loosen. VCSEL pumped VECSEL concept with compact design. *Electronics Letters* **55**, 12 (2019), 705–707. DOI: 10.1049/el.2019.0574.

[53] R. Häring, R. Paschotta, A. Aschwanden, E. Gini, F. Morier-Genoud and U. Keller. High-power passively mode-locked semiconductor lasers. *IEEE Journal of Quantum Electronics* **38**, 9 (2002), 1268–1275. DOI: 10.1109/JQE.2002.802111.

[54] A. Härkönen, C. Grebing, J. Paajaste, R. Koskinen, J.-P. Alanko, S. Suomalainen, G. Steinmeyer and M. Guina. Modelocked GaSb disk laser producing 384 fs pulses at 2 µm wavelength. *Electronics Letters* **47**, 7 (2011), 454–456. DOI: 10.1049/el.2011.0253.

[55] K. G. Wilcox, A. H. Quarterman, V. Apostolopoulos, H. E. Beere, I. Farrer, D. A. Ritchie and A. C. Tropper. 175 GHz, 400-fs-pulse harmonically mode-locked surface emitting semiconductor laser. *Optics Express* **20**, 7 (2012), 7040–7045. DOI: 10.1364/OE.20.007040.

[56] T. Schwarzbäck, H. Kahle, M. Eichfelder, R. Roßbach, M. Jetter and P. Michler. Wavelength tunable ultraviolet laser emission via intra-cavity frequency doubling of an AlGaInP vertical external-cavity surface-emitting laser down to 328 nm. *Applied Physics Letters* **99**, 26 (2011), 261101 -261101–3. DOI: 10.1063/1.3660243.

[57] S. Ranta, M. Tavast, T. Leinonen, R. Epstein and M. Guina. Narrow linewidth 1118/559 nm VECSEL based on strain compensated GaInAs/GaAs quantum-wells for laser cooling of Mg-ions. *Optical Materials Express* **2**, 8 (2012), 1011–1019. DOI: 10.1364/OME.2.001011.

[58] V. Magni. Resonators for solid-state lasers with large-volume fundamental mode and high alignment stability. *Applied Optics* **25**, 1 (1986), 107–117. DOI: 10.1364/AO.25.000107.

[59] A. Laurain, J. Hader and J. V. Moloney. Modeling and optimization of transverse modes in vertical-external-cavity surface-emitting lasers. *Journal of the Optical Society of America B* **36**, 4 (2019), 847–854. DOI: 10.1364/JOSAB.36.000847.

[60] A. C. Tropper and S. Hoogland. Extended cavity surface-emitting semiconductor lasers. *Progress in Quantum Electronics* **30**, 1 (2006), 1–43. DOI: 10.1016/j.pquantelec.2005.10.002.

[61] H. Kahle, J.-P. Penttinen, H.-M. Phung, P. Rajala, A. Tukiainen, S. Ranta and M. Guina. Comparison of single-side and double-side pumping of membrane external-cavity surface-emitting lasers. *Optics Letters* **44**, 5 (2019), 1146–1149. DOI: 10.1364/OL.44.001146.

[62] H. Lindberg, M. Strassner, E. Gerster, J. Bengtsson and A. Larsson. Thermal management of optically pumped long-wavelength InP-based semiconductor disk lasers. *IEEE Journal of Selected Topics in Quantum Electronics* **11**, 5 (2005), 1126–1134. DOI: 10.1109/JSTQE.2005.853730.

[63] J. V. Moloney, J. Hader and S. W. Koch. Quantum design of semiconductor active materials: laser and amplifier applications. *Laser & Photonics Review* **1**, 1 (2007), 24–43. DOI: 10.1002/lpor.200610003.

[64] J. P. Gordon, R. C. C. Leite, R. S. Moore, S. P. S. Porto and J. R. Whinnery. Long-Transient Effects in Lasers with Inserted Liquid Samples. *Journal of Applied Physics* **36**, 1 (1965), 3–8. DOI: 10.1063/1.1713919.

[65] A. J. Kemp, A. J. Maclean, J. E. Hastie, S. A. Smith, J.-M. Hopkins, S. Calvez, G. J. Valentine, M. D. Dawson and D. Burns. Thermal lensing, thermal management and transverse mode control in microchip VECSELs. *Applied Physics B* **83**, 2 (2006), 189–194. DOI: 10.1007/s00340-006-2151-z.

[66] L. Fan, J. Hader, M. Schillgalies, M. Fallahi, A. R. Zakharian, J. V. Moloney, R. Bedford, J. T. Murray, S. W. Koch and W. Stolz. High-power optically pumped VECSEL using a double-well resonant periodic gain structure. *IEEE Photonics Technology Letters* **17**, 9 (2005), 1764–1766. DOI: 10.1109/LPT.2005.853536.

[67] A. Rantamäki, J. Rautiainen, L. Toikkanen, I. Krestnikov, M. Butkus, E. U. Rafailov and O. Okhotnikov. Flip Chip Quantum-Dot Semiconductor Disk Laser at 1200 nm. *IEEE Photonics Technology Letters* **24**, 15 (2012), 1292–1294. DOI: 10.1109/LPT.2012.2202222.

[68] E. R. Dobrovinskaya, L. A. Lytvynov and V. Pishchik. Sapphire: Material, Manufacturing, Applications - Properties of Sapphire. Boston, MA: Springer US, 2009, 55–176. DOI: 10.1007/978-0-387-85695-7_2.

[69] J. E. Hastie, J.-M. Hopkins, S. Calvez, C. W. Jeon, D. Burns, R. Abram, E. Riis, A. I. Ferguson and M. D. Dawson. 0.5-W single transverse-mode operation of an 850-nm diode-pumped surface-emitting semiconductor laser. *IEEE Photonics Technology Letters* **15**, 7 (2003), 894–896. DOI: 10.1109/LPT.2003.813446.

[70] X. Qian, P. Jiang and R. Yang. Anisotropic Thermal Conductivity of 4H and 6H Silicon Carbide Measured Using Time-Domain Thermoreflectance. *Materials Today Physics* **3** (2017), 70–75. DOI: 10.1016/j.mtphys.2017.12.005.

[71] J.-M. Hopkins, S. A. Smith, C. W. Jeon, H. D. Sun, D. Burns, S. Calvez, M. D. Dawson, T. Jouhti and M. Pessa. 0.6 W CW GaInNAs vertical external-cavity surface emitting laser operating at 1.32 µm. *Electronics Letters* **40**, 1 (2004), 30–31. DOI: 10.1049/el:20040049.

[72] S. Giet, H. D. Sun, S. Calvez, M. D. Dawson, S. Suomalainen, A. Härkönen, M. Guina, O. Okhotnikov and M. Pessa. Spectral narrowing and locking of a vertical-external-cavity surface-emitting laser using an intracavity volume Bragg grating. *IEEE Photonics Technology Letters* **18**, 16 (2006), 1786–1788. DOI: 10.1109/LPT.2006.880735.

[73] A. Härkönen, S. Suomalainen, E. Saarinen, L. Orsila, R. Koskinen, O. Okhotnikov, S. Calvez and M. Dawson. 4 W single-transverse mode VECSEL utilising intra-cavity diamond heat spreader. *Electronics Letters* **42**, 12 (2006), 693–694. DOI: 10.1049/el:20060462.

[74] D. Waldburger, S. M. Link, M. Mangold, C. G. E. Alfieri, E. Gini, M. Golling, B. W. Tilma and U. Keller. High-power 100 fs semiconductor disk lasers. *Optica* **3**, 8 (2016), 844–852. DOI: 10.1364/OPTICA.3.000844.

[75] M. Butkus, J. Rautiainen, O. G. Okhotnikov, C. J. Hamilton, G. P. A. Malcolm, S. S. Mikhrin, I. L. Krestnikov, D. A. Livshits and E. U. Rafailov. Quantum Dot Based Semiconductor Disk Lasers for 1–1.3 µm. *IEEE Journal of Selected Topics in Quantum Electronics* **17**, 6 (2011), 1763–1771. DOI: 10.1109/JSTQE.2011.2112638.

[76] B. Cordero, V. Gómez, A. Platero-Prats, M. Revés, J. Echeverria, E. Cremades, F. Barragán and S. Alvarez. Covalent radii revisited. *Dalton transactions* **21** (2008), 2832–8. DOI: 10.1039/b801115j.

[77] D. E. Aspnes, S. M. Kelso, R. A. Logan and R. Bhat. Optical properties of $Al_xGa_{1-x}As$. *Journal of Applied Physics* **60**, 2 (1986), 754–767. DOI: 10.1063/1.337426.

[78] H. A. Zarem, J. A. Lebens, K. B. Nordstrom, P. C. Sercel, S. Sanders, L. E. Eng, A. Yariv and K. J. Vahala. Effect of Al mole fraction on carrier diffusion lengths and lifetimes in $Al_xGa_{1-x}As$. *Applied Physics Letters* **55**, 25 (1989), 2622–2624. DOI: 10.1063/1.101955.

[79] L. Pavesi and M. Guzzi. Photoluminescence of $Al_xGa_{1-x}As$ alloys. *Journal of Applied Physics* **75**, 10 (1994), 4779–4842. DOI: 10.1063/1.355769.

[80] J. Roberts, J. David, L. Smith and P. Tihanyi. The influence of trimethylindium impurities on the performance of InAlGaAs single quantum well lasers. *Journal of Crystal Growth* **195**, 1 (1998), 668–675. DOI: 10.1016/S0022-0248(98)00665-4.

[81] L. J. Mawst, S. Rusli, A. Al-Muhanna and J. K. Wade. Short-Wavelength ($0.7\,\mu m < \lambda < 0.78\,\mu m$) High-Power InGaAsP-Active Diode Lasers. *IEEE Journal of Selected Topics in Quantum Electronics* **5**, 3 (1999), 785–791. DOI: 10.1109/2944.788452.

[82] R. Moon, G. Antypas and L. W. James. Bandgap and lattice constant of GaInAsP as a function of alloy composition. *Journal of Electronic Materials* **3** (1974), 635–644.

[83] Y. Yamazoe, T. Nishino, Y. Hamakawa and T. Kariya. Bandgap Energy of InGaAsP Quaternary Alloy. *Japanese Journal of Applied Physics* **19**, 8 (1980), 1473. DOI: 10.1143/JJAP.19.1473.

[84] G. Zhang, M. Pessa, K. Hjelt, H. Collan and T. Tuomi. Gas-source molecular beam epitaxy of lattice-matched $Ga_xIn_{1-x}As_yP_{1y}$ on GaAs over the entire composition range. *Journal of Crystal Growth* **150** (1995), 607–611. DOI: 10.1016/0022-0248(95)80281-G.

[85] J. K. Wade, L. J. Mawst, D. Botez and J. A. Morris. 8.8 W CW power from broad-waveguide Al-free active-region ($\lambda = 805$ nm) diode lasers. *Electronics Letters* **34**, 11 (1998), 1100–1101. DOI: 10.1049/el:19980775.

[86] J. Diaz, I. Eliashevich, K. Mobarhan, E. Kolev, L. Wang, D. Garbuzov and M. Razeghi. InGaP/InGaAsP/GaAs 0.808 µm separate confinement laser diodes grown by metalorganic chemical vapor deposition. *IEEE Photonics Technology Letters* **6**, 2 (1994), 132–134. DOI: 10.1109/68.275405.

[87] K. Uppal, A. Mathur and P. Dapkus. Strain effects on InGaP-InGaAsP-GaAsP tensile strained quantum-well lasers. *IEEE Photonics Technology Letters* **7**, 10 (1995), 1128–1130. DOI: 10.1109/68.466565.

[88] F. Daiminger, S. Heinemann, J. Nappi, M. Toivonen and H. Asonen. 100 W cw Al-free 808 nm linear bar arrays. *CLEO '97., Summaries of Papers Presented at the Conference on Lasers and Electro-Optics*. **11**. 1997, 482–483. DOI: 10.1109/CLEO.1997.603475.

[89] J. Diaz, H. J. Yi, M. Razeghi and G. T. Burnham. Long-term reliability of Al-free InGaAsP/GaAs (=808nm) lasers at high-power high-temperature operation. *Applied Physics Letters* **71**, 21 (1997), 3042–3044. DOI: 10.1063/1.119431.

[90] D. Garbuzov, N. Antonishkis, A. Bondarev, A. Gulakov, S. Zhigulin, N. Katsavets, A. Kochergin and E. Rafailov. High-power 0.8 µm InGaAsP-GaAs SCH SQW lasers. *IEEE Journal of Quantum Electronics* **27**, 6 (1991), 1531–1536. DOI: 10.1109/3.89973.

[91] C. Paranthoën, N. Bertru, O. Dehaese, A. Le Corre, S. Loualiche, B. Lambert and G. Patriarche. Height dispersion control of InAs/InP quantum dots emitting at 1.55. *Applied Physics Letters* **78**, 12 (2001), 1751–1753. DOI: 10.1063/1.1356449.

[92] K. Nechay, A. Mereuta, C. Paranthoën, G. Brévalle, C. Levallois, M. Alouini, N. Chevalier, M. Perrin, G. Suruceanu, A. Caliman, M. Guina and E. Kapon. InAs/InP quantum dot VECSEL emitting at 1.5 µm. *Applied Physics Letters* **115**, 17 (2019), 171105. DOI: 10.1063/1.5125632.

[93] J. E. Ayers, T. Kujofsa, P. Rago and J. E. Raphael. Heteroepitaxy of Semiconductors: Theory, Growth, and Characterization. 2nd ed. CRC Press, 2016. DOI: 10.1201/9781315372440-4.

[94] M. Pessa, K. Tappura and A. Ovtchinnikov. GaInAsP gas-source MBE technology. *Thin Solid Films* **267**, 1 (1995). Workshop on molecular beam expitaxy-growth physics and technology, 99–105. DOI: 10.1016/0040-6090(95)06626-8.

[95] W. Zhou and Z. L. Wang. Scanning microscopy for nanotechnology : techniques and applications. 6th ed. New York: Springer, 2007.

[96] J. Cederberg, A. Albrecht, M. Ghasemkhani, S. Melgaard and M. Sheik-Bahae. Growth and testing of vertical external cavity surface emitting lasers (VECSELs) for intracavity cooling of Yb:YLF. *Journal of Crystal Growth* **393** (2014), 28–31. DOI: 10.1016/j.jcrysgro.2013.09.042.

[97] H. Kahle. AlGaInP-based high-performance semiconductor disk lasers for the red spectral range: Gain-chip design, harmonic generation and a new laser concept. PhD thesis. University of Stuttgart, Institute for Semiconductor Optics and Functional Interfaces, 2017.

[98] S. Arscott, P. Mounaix and D. Lippens. Substrate transfer process for InP-based heterostructure barrier varactor devices. *Journal of Vacuum Science & Technology B: Microelectronics and Nanometer Structures* **18** (2000), 150–155. DOI: 10.1116/1.591167.

[99] P. H. L. Notten. The Etching of InP in HCl Solutions: A Chemical Mechanism. *Journal of The Electrochemical Society* **131**, 11 (1984), 2641–2644. DOI: 10.1149/1.2115375.

[100] P. Eliáš, S. Hasenöhrl, V. Cambel and I. Kostič. Crystallographic dependence of OMVPE InGaAs/InP lateral growth on patterned (100) InP substrates prepared by wet etching. *Thin Solid Films* **380**, 1 (2000), 105–107. DOI: 10.1016/S0040-6090(00)01479-6.

[101] A. J. Maclean, R. B. Birch, P. W. Roth, A. J. Kemp and D. Burns. Limits on efficiency and power scaling in semiconductor disk lasers with diamond heatspreaders. *Journal of the Optical Society of America B* **26**, 12 (2009), 2228–2236. DOI: 10.1364/JOSAB.26.002228.

[102] S. Adachi. Lattice thermal resistivity of III–V compound alloys. *Journal of Applied Physics* **54**, 4 (1983), 1844–1848. DOI: 10.1063/1.332820.

[103] H. Yang, H. Wang, K. Radhakrishnan and C. Tan. Thermal resistance of metamorphic InP-based HBTs on GaAs substrates using a linearly graded $In_xGa_{1-x}P$ metamorphic buffer. *IEEE Trans. Electron Devices* **51** (2004), 1221–1227. DOI: 10.1109/TED.2004.831364.

[104] B. Heinen, F. Zhang, M. Sparenberg, B. Kunert, M. Koch and W. Stolz. On the Measurement of the Thermal Resistance of Vertical-External-Cavity Surface-Emitting Lasers (VECSELs). *IEEE Journal of Quantum Electronics* **48**, 7 (2012), 934–940. DOI: 10.1109/JQE.2012.2196678.

[105] H. Kahle, J.-P. Penttinen, H.-M. Phung, P. Rajala, A. Tukiainen, S. Ranta and M. Guina. MECSELs with direct emission in the 760 nm to 810 nm spectral range: A single- and double-side pumping comparison and high-power continuous-wave operation. **10901**. 2019. DOI: 10.1117/12.2512111.

[106] H.-M. Phung, H. Kahle, J.-P. Penttinen, P. Rajala, S. Ranta and M. Guina. Power scaling and thermal lensing in 825nm emitting membrane external-cavity surface-emitting lasers. *Optics Letters* **45**, 2 (2020), 547–550. DOI: 10.1364/OL.382377.

[107] H.-M. Phung, P. Tatar-Mathes, C. Paranthoën, C. Levallois, N. Chevalier, M. Perrin, A. Kerchaoui, H. Kahle, M. Alouini and M. Guina. Quantum dot membrane external-cavity surface-emitting laser at 1.5 µm. *Applied Physics Letters* **118**, 23 (2021), 231101. DOI: 10.1063/5.0053961.

[108] H. Kahle, J.-P. Penttinen, H.-M. Phung, P. Rajala, A. Tukiainen, S. Ranta and M. Guina. Double-side pumped membrane external-cavity surface-emitting lasers (MECSELs): Towards a "solid-state laser"-like gain pump configuration. *2019 Conference on Lasers and Electro-Optics Europe and European Quantum Electronics Conference*. Optical Society of America, 2019, cb_11_3. URL: http://www.osapublishing.org/abstract.cfm?URI=CLEO_Europe-2019-cb_11_3.

[109] B. Heinen, C. Möller, K. Jandieri, B. Kunert, M. Koch and W. Stolz. The Thermal Resistance of High-Power Semiconductor Disk Lasers. *IEEE Journal of Quantum Electronics* **51**, 5 (2015), 1–9. DOI: 10.1109/JQE.2015.2412458.

[110] M. A. Afromowitz. Thermal conductivity of $Ga_{1-x}Al_xAs$ alloys. *Journal of Applied Physics* **44**, 3 (1973), 1292–1294. DOI: 10.1063/1.1662342.

[111] B. Monemar, K. K. Shih and G. D. Pettit. Some optical properties of the $Al_xGa_{1-x}As$ alloys system. *Journal of Applied Physics* **47**, 6 (1976), 2604–2613. DOI: 10.1063/1.322979.

[112] G. N. West, A. C. Sills and P. O. Leisher. Volume holographic grating stabilized 780 nm VECSEL. **9134**. 2014, 91340Y. DOI: 10.1117/12.2048810.

[113] H. Kahle, K. Nechay, J.-P. Penttinen, A. Tukiainen, S. Ranta and M. Guina. AlGaAs-based vertical-external-cavity surface-emitting laser exceeding 4 W of direct emission power in the 740 - 790 nm spectral range. *Optics Letters* **43**, 7 (2018), 1578–1581. DOI: 10.1364/OL.43.001578.

[114] K. Nechay, H. Kahle, J. Penttinen, P. Rajala, A. Tukiainen, S. Ranta and M. Guina. AlGaAs/AlGaInP VECSELs with direct emission at 740 -770 nm. *IEEE Photonics Technology Letters* (2019), 1–1. DOI: 10.1109/LPT.2019.2924289.

[115] S. Masui, T. Miyoshi, T. Yanamoto and S.-i. Nagahama. 1 W AlInGaN Based Green Laser Diodes. *2013 Conference on Lasers and Electro-Optics Pacific Rim* (2013), WH3_1. URL: http://www.osapublishing.org/abstract.cfm?URI=CLEOPR-2013-WH3_1.

[116] A. R. Zakharian, J. Hader, J. V. Moloney, S. W. Koch, P. Brick and S. Lutgen. Experimental and theoretical analysis of optically pumped semiconductor disk lasers. *Applied Physics Letters* **83**, 7 (2003), 1313–1315. DOI: 10.1063/1.1601672.

[117] O. G. Okhotnikov. Power scalable semiconductor disk lasers for frequency conversion and mode-locking. *Quantum Electronics* **38**, 12 (2008), 1083–1096. DOI: 10.1070/QE2008v038n12ABEH013965.

[118] M. Kuznetsov, F. Hakimi, R. Sprague and A. Mooradian. Design and characteristics of high-power (> 0.5-W CW) diode-pumped vertical-external-cavity surface-emitting semiconductor lasers with circular TEM_{00} beams. **5**, 3 (1999), 561–573. DOI: 10.1109/2944.788419.

[119] L. Fan, M. Fallahi, J. Hader, A. R. Zakharian, J. V. Moloney, J. T. Murray, R. Bedford, W. Stolz and S. W. Koch. Multichip vertical-external-cavity surface-emitting lasers: a coherent power scaling scheme. *Optics Letters* **31**, 24 (2006), 3612–3614. DOI: 10.1364/OL.31.003612.

[120] E. J. Saarinen, A. Härkönen, S. Suomalainen and O. G. Okhotnikov. Power scalable semiconductor disk laser using multiple gain cavity. *Optics Express* **14**, 26 (2006), 12868–12871. DOI: 10.1364/OE.14.012868.

[121] C. Stewen, K. Contag, M. Larionov, A. Giesen and H. Hugel. A 1-kW CW thin disc laser. *IEEE Journal of Selected Topics in Quantum Electronics* **6**, 4 (2000), 650–657. DOI: 10.1109/2944.883380.

[122] R. G. Bedford, M. Kolesik, J. L. A. Chilla, M. K. Reed, T. R. Nelson and J. V. Moloney. Power-limiting mechanisms in VECSELs. Ed. by J. Andrew R. Pirich; Michael J. Hayduk; Eric J. Donkor; Peter J. Delfyett. **5814**. Enabling Photonics Technologies for Defense, Security, and Aerospace Applications. 2005, 199–208. DOI: 10.1117/12.607428.

[123] T.-L. Wang, B. Heinen, J. Hader, C. Dineen, M. Sparenberg, A. Weber, B. Kunert, S. W. Koch, J. V. Moloney, M. Koch and W. Stolz. Quantum design strategy pushes high-power vertical-external-cavity surface-emitting lasers beyond 100 W. *Laser Photonics Rev.* **6**, 5 (2012), L12–L14. DOI: 10.1002/lpor.201200034.

[124] M. Schiller. A high-power laser transmitter for ground-based and airborne water-vapor measurements in the troposphere. PhD thesis. University of Stuttgart, 2009.

[125] G. Wagner, A. Behrendt, V. Wulfmeyer, F. Späth and M. Schiller. High-power Ti: Sapphire laser at 820 nm for scanning ground-based water-vapor differential absorption lidar. *Applied Optics* **52** (2013), 2454–69. DOI: 10.1364/AO.52.002454.

[126] A. Yariv and P. Yeh. *Photonics: Optical Electronics in Modern Communications (The Oxford Series in Electrical and Computer Engineering)*. New York, NY, USA: Oxford University Press, Inc., 2006.

[127] D. Findlay and R. Clay. The measurement of internal losses in 4-level lasers. *Phys. Lett.* **20**, 3 (1966), 277–278. DOI: DOI:10.1016/0031-9163(66)90363-5.

[128] S. J. McGinily. Optically Pumped Semiconductor Vertical External Cavity Surface Emitting Lasers. PhD thesis. University of Strathclyde, 2005.

[129] S.-S. Beyertt, U. Brauch, F. Demaria, N. Dhidah, A. Giesen, T. Kübler, S. Lorch, F. Rinaldi and P. Unger. Efficient Gallium-Arsenide Disk Laser. *IEEE Journal of Quantum Electronics* **43**, 10 (2007), 869–875. DOI: 10.1109/JQE.2007.904074.

[130] Y. Bai, Z. Xu, Y. Lin, J. Wisdom, C. Scholz, E. Weiss, J. Chilla and A. Diening. *AlGaAs-based optically pumped semiconductor lasers*. 2018. DOI: 10.1117/12.2291082.

[131] H.-M. Phung, H. Kahle, J.-P. Penttinen, P. Rajala, S. Ranta and M. Guina. A membrane external-cavity surface-emitting laser (MECSEL) with emission around 825 nm. *Vertical External Cavity Surface Emitting Lasers (VECSELs) X*. **11263**. 2020, 49–56. DOI: 10.1117/12.2545980.

[132] D. Lorenser, D. J. H. C. Maas, H. J. Unold, A.-R. Bellancourt, B. Rudin, E. Gini, D. Ebling and U. Keller. 50-GHz passively mode-locked surface-emitting semiconductor laser with 100-mW average output power. *IEEE Journal of Quantum Electronics* **42**, 8 (2006), 838–847. DOI: 10.1109/JQE.2006.878183.

[133] A. E. Siegman. *Lasers*. Mill Valley, California: University Science Books, 1986.

[134] S. G. Sokolov, J. L. Lian, S. Combrie, A. De Rossi and A. P. Mosk. Measurement of the linear thermo-optical coefficient of $Ga_{0.51}In_{0.49}P$ using photonic crystal nanocavities. *Applied Optics* **56**, 11 (2017), 3219–3222. DOI: 10.1364/AO.56.003219.

[135] S. Ranta. Wavelength Extension of Visible VECSELs by Structural Engineering. PhD thesis. Tampere University of Technology, 2014.

[136] C. Symonds, I. Sagnes, A. Garnache, S. Hoogland, G. Saint-Girons, A. C. Tropper and J.-L. Oudar. Continuous-wave operation of monolithically grown 1.5-µm optically pumped vertical-external-cavity surface-emitting lasers. *Applied Optics* **42**, 33 (2003), 6678–6681. DOI: 10.1364/AO.42.006678.

[137] S. Hoogland, A. Garnache, I. Sagnes, B. Paldus, K. J. Weingarten, R. Grange, M. Haiml, R. Paschotta, U. Keller and A. C. Tropper. Picosecond pulse generation with 1.5 µm passively modelocked surface-emitting semiconductor laser. *Electronics Letters* **39**, 11 (2003), 846–847. DOI: 10.1049/el:20030576.

[138] C. Symonds, I. Sagnes, J.-L. Oudar, S. Bouchoule, A. Garnache, J. Berggren and M. Strassner. Room temperature CW lasing operation of monolithically grown 1.55 µm vertical external cavity surface emitting laser. *Optics Communications* **230**, 4 (2004), 419–423. DOI: 10.1016/j.optcom.2003.11.023.

[139] H. Lindberg, A. Larsson and M. Strassner. Single-frequency operation of a high-power, long-wavelength semiconductor disk laser. *Optics Letters* **30**, 17 (2005), 2260–2262. DOI: 10.1364/OL.30.002260.

[140] J.-P. Tourrenc, S. Bouchoule, A. Khadour, J.-C. Harmand, A. Miard, J. Decobert, N. Lagay, X. Lafosse, I. Sagnes, L. Leroy and J.-L. Oudar. Thermal optimization of 1.55 µm OP-VECSEL with hybrid metal-metamorphic mirror for single-mode high power operation. *Optical and Quantum Electronics* **40** (2 2008), 155–165.

[141] V. M. Korpijärvi, E. L. Kantola, T. Leinonen, R. Isoaho and M. Guina. Monolithic GaInNAsSb/GaAs VECSEL Operating at 1550 nm. *IEEE Journal of Selected Topics in Quantum Electronics* **21**, 6 (2015), 480–484. DOI: 10.1109/JSTQE.2015.2415200.

[142] A. Mereuta, K. Nechay, A. Caliman, G. Suruceanu, A. Rudra, P. Gallo, M. Guina and E. Kapon. Flip-chip Wafer-fused OP-VECSELs emitting 3.65 W at the 1.55-µm waveband. *IEEE Journal of Selected Topics in Quantum Electronics* (2019), 1–1. DOI: 10.1109/JSTQE.2019.2922819.

[143] E. J. Saarinen, J. Puustinen, A. Sirbu, A. Mereuta, A. Caliman, E. Kapon and O. G. Okhotnikov. Power-scalable 1.57 µm mode-locked semiconductor disk laser using wafer fusion. *Optics Letters* **34**, 20 (2009), 3139–3141. DOI: 10.1364/OL.34.003139.

[144] J. Rautiainen, J. Lyytikäinen, A. Sirbu, A. Mereuta, A. Caliman, E. Kapon and O. Okhotnikov. 2.6 W optically-pumped semiconductor disk laser operating at 1.57-µm using wafer fusion. *Optics Express* **16** (2009), 21881–6. DOI: 10.1364/OE.16.021881.

[145] A. Sirbu, N. Volet, A. Mereuta, J. Lyytikäinen, J. Rautiainen, O. Okhotnikov, J. Walczak, M. Wasiak, T. Czyszanowski, A. Caliman, Q. Zhu, I. Vladimir and E. Kapon. Wafer-Fused Optically Pumped VECSELs Emitting in the 1310-nm and 1550-nm Wavebands. *Advances in Optical Technologies* **2011** (2011). DOI: 10.1155/2011/209093.

[146] E. J. Saarinen, J. Lyytikäinen, S. Ranta, A. Rantamäki, A. Saarela, A. Sirbu, V. Iakovlev, E. Kapon and O. G. Okhotnikov. A 1.5-W frequency doubled semiconductor disk laser tunable over 40 nm at around 745 nm. *Vertical External Cavity Surface Emitting Lasers (VECSELs) VI*. Ed. by K. G. Wilcox. **9734**. International Society for Optics and Photonics. SPIE, 2016, 103–110. DOI: 10.1117/12.2209384.

[147] K. Nechay, A. Mereuta, C. Paranthoën, G. Brévalle, C. Levallois, M. Alouini, N. Chevalier, M. Perrin, G. Suruceanu, A. Caliman, E. Kapon and M. Guina. High-Power 760 nm VECSEL Based on Quantum Dot Gain Mirror. *IEEE Journal of Quantum Electronics* **56**, 4 (2020), 1–4. DOI: 10.1109/JQE.2020.2986770.

[148] I. Kudman and E. F. Steigmeier. Thermal Conductivity and Seebeck Coefficient of InP. *Physics Review* **133** (6A 1964), A1665–A1667. DOI: 10.1103/PhysRev.133.A1665.

[149] Z. Chen, J. Yang and Y. Chen. Thermal Conductivity of InGaAs/InGaAsP Superlattices measured with 3ω Method. *2006 1st IEEE International Conference on Nano/Micro Engineered and Molecular Systems* (2006), 283–286.

[150] A. Laurain, M. Myara, G. Beaudoin, I. Sagnes and A. Garnache. High power single–frequency continuously–tunable compact extended–cavity semiconductor laser. *Optics Express* **17**, 12 (2009), 9503–9508. DOI: 10.1364/OE.17.009503.

[151] S. Pes, C. Paranthoën, C. Levallois, N. Chevalier, C. Hamel, K. Audo, G. Loas, S. Bouhier, C. Gomez, J.-C. Harmand, S. Bouchoule, H. Folliot and M. Alouini. Class-A operation of an optically-pumped 1.6 µm-emitting quantum dash-based vertical-external-cavity surface-emitting laser on InP. *Optics Express* **25**, 10 (2017), 11760–11766. DOI: 10.1364/OE.25.011760.

[152] C. Paranthoën, C. Levallois, G. Brévalle, M. Perrin, A. Le Corre, N. Chevalier, P. Turban, C. Cornet, H. Folliot and M. Alouini. Low Threshold 1550-nm Emitting QD Optically Pumped VCSEL. *IEEE Photonics Technology Letters* **33**, 2 (2021), 69–72. DOI: 10.1109/LPT.2020.3044457.

PUBLICATIONS

PUBLICATION

I

Comparison of single-side and double-side pumping of membrane external-cavity surface-emitting lasers

H. Kahle, J.-P. Penttinen, H.-M. Phung, P. Rajala, A. Tukiainen, S. Ranta and M. Guina

Optics Letters **44**(5) (2019), 1146–1149
DOI: 10.1364/OL.44.001146

Optics Letters

Comparison of single-side and double-side pumping of membrane external-cavity surface-emitting lasers

Hermann Kahle,* Jussi-Pekka Penttinen, Hoy-My Phung, Patrik Rajala, Antti Tukiainen, Sanna Ranta, and Mircea Guina

Optoelectronics Research Centre (ORC), Physics Unit/Photonics, Faculty of Engineering and Natural Science, Tampere University, Korkeakoulunkatu 3, 33720 Tampere, Finland
**Corresponding author: hermann.kahle@tuni.fi*

Received 2 January 2019; revised 27 January 2019; accepted 27 January 2019; posted 29 January 2019 (Doc. ID 356544); published 21 February 2019

We studied and compared single-side pumping (SSP) and double-side pumping (DSP) of a semiconductor membrane external-cavity surface-emitting laser (MECSEL). The MECSEL-active region was based on an AlGaAs quantum well structure embedded between two silicon carbide (SiC) wafer pieces that were used as transparent intra-cavity (IC) heat spreaders creating a symmetrical cooling environment. The gain structure targeted emission at 780 nm, a wavelength region that is important for many applications, and where the development of high-brightness high-power laser sources is gaining more momentum. By DSP at 20°C heat sink temperature, we could reduce the laser threshold from 0.79 to 0.69 W of absorbed pump power, while the maximum output power was increased from 3.13 to 3.22 W. The differential efficiency was improved from 31.9% to 34.4%, which represents a record value for SiC-cooled vertically emitting semiconductor lasers. The improvements are enabled by a reduced thermal resistance of the gain element by 9% compared to SSP. The beam quality was measured to be $M^2 < 1.09$. Finally, we demonstrate a maximum tuning range from 767 to 811 nm. This wavelength range was not addressed by any MECSEL or vertical external-cavity surface-emitting laser device before and extends the available wavelengths for semiconductor based high-quality beam and high-power laser sources to a wavelength window relevant for quantum technology, spectroscopy, or medicine.

https://doi.org/10.1364/OL.44.001146

The membrane external-cavity surface-emitting laser (MECSEL) has recently emerged to solve some of the constraints limiting wavelength extension and power scaling of vertical external-cavity surface-emitting lasers (VECSELs) [1]. The key distinctive feature is that the gain element does not contain a monolithically integrated distributed Bragg reflector (DBR) as is the case in conventional VECSELs [2,3]. Second, the MECSEL enables the gain structure to be placed between two heat spreaders and, hence, potentially leads to a more efficient cooling and better power scaling capability. Pioneering work towards this achievement was made by Iakovlev *et al.* who proposed a very similar setup [4] in 2014. Furthermore, Yang *et al.* investigated a semiconductor membrane laser, also called DBR-free semiconductor disk laser [5], with the laser-active semiconductor membrane bonded onto one IC heat spreader. They also proposed the laser-active region arrangement between two heat spreaders as thermally beneficial. Recently, a MECSEL with diamond heat spreaders operating around 985 nm was reported [6]. Moreover, Yang *et al.* succeeded in demonstrating [7] a MECSEL double-side cooled using SiC emitting approximately at 1037 nm and also reported on the comparison with the single SiC heat spreader approach [8]. The use of SiC as an IC heat spreader has its benefits in the huge thickness homogeneity, the high degree of parallelism, and the comparably low price related to a single-crystal diamond.

In this Letter, we present a study comparing single-side pumping (SSP) and double-side pumping (DSP) of a MECSEL, as well as a detailed set of characterization data. The possibility of DSP is a built-in benefit of the MECSEL itself, enabling the pumping and treating of this type of active region membrane heat spreader package in a similar way, like classical solid-state (thin-disk) laser elements [9,10]. This study was performed with an active region optimized for 780 nm emission with the aim at extending the accessible wavelength range into the red/near-infrared transition region and to meet the need of high-quality beam sources in this wavelength range.

The MECSEL structure was grown on an undoped 2 in. GaAs (100) ± 0.5° wafer using a *V80H-10 VG Semicon* solid source molecular beam epitaxy system at a growth temperature of about 575°C. A GaAs buffer layer was first grown on the substrate followed by an ∼150 nm thick AlAs process layer and the active region, which was designed to be completely symmetric and resonant for 780 nm. The total thickness of the gain region was 577 nm [see the scanning

electron microscope (SEM) picture inset in Fig. 1] and corresponded to a resonant 2.5λ subcavity. It consists of twelve $Al_{0.09}Ga_{0.91}As$ quantum wells (QWs) with a thickness of about 7 nm each, arranged in four groups of three QWs each. The QWs are separated and embedded by layers of $Al_{0.39}Ga_{0.61}As$—8 nm in between the QWs and 12 nm around the QW package. These four QW packages can be seen in the SEM inset in Fig. 1 as vertical stripes, which are a little bit brighter than the surrounding and equally spaced within the active region. As spacer material separating the QW groups, we employed $Al_{0.58}Ga_{0.42}As$, which has an absorption edge at ~550 nm [11]. The whole active region was then embedded between a 10 nm thick AlInP and a 10 nm thick GaInP layer. These layers helped block the electron diffusion and act as window layer at the semiconductor heat spreader interface.

In order to isolate the gain membrane, a piece of about 7 mm × 7 mm of the as-grown structure was bonded with the epitaxy side onto one ~350 μm thick and uncoated 4H-SiC wafer piece. The SiC wafer piece was of about the same size as the gain membrane sample and acts later as an IC heat spreader. After the substrate and AlAs layer removal process (details can be found elsewhere [1]), a second (uncoated) SiC heat spreader originating from the same SiC wafer was bonded on top of the SiC-membrane package. The whole sandwich was then clamped between water/glycol-cooled and Peltier-element temperature controlled copper plates. Indium foil was used to improve the thermal contact between the SiC heat spreaders and the copper plates. For all measurements presented here, the heat sink temperature of the gain element was set and stabilized to $T_{hs} = 20°C$. The gain sandwich clamped between copper plates was mounted to a XYZ stage, which was mounted onto a tilt/jar stage itself. The whole characterization setup was built around this gain element mount and is schematically shown in Fig. 1. Each of the copper plates had a conical aperture of about 1.5 mm in diameter (see photograph inset of Fig. 1) to enable vertical laser emission as well as pumping from both sides. As a pump laser, we used a *Coherent Verdi-V18*, which delivered up to 18.5 W of pump power at a 532 nm emission wavelength.

For an accurate comparison of SSP and DSP of the gain element, incident pump power P_{inc}, reflected pump power P_{refl}, and transmitted pump power P_{trans} were measured directly before or after the gain element and the absorbed pump power $P_{abs.,pump}$ could be calculated. For DSP, the pump beam was divided with a polarizing beam splitter (PBS). A $\lambda/2$ plate was used to adjust the polarization of the pump beam before the PBS to divide the pump beam in such a way that the different losses in the two different pump arms 1 and 2, as well as the polarization depending variation in reflection at the air–SiC interface, are compensated, and a symmetrically balanced pump absorption situation was created. The distribution of the absorbed pump light for the two incident directions related to the pump arms and the total absorbed pump light (100%) within the gain package was 50.03% for pump arm 1 and 49.97% for pump arm 2. For the high-power measurements with SSP, the PBS was removed, and only pump arm 1 was used. A pump spot diameter of (88 ± 8)μm in the tangential and (91 ± 8)μm in the sagittal plane was calculated from a measured pump lens distance of (204 ± 1)mm. For the MECSEL characterization, a V-shaped resonator with a total length of ~495.5 mm was used (see Fig. 1). The gain element was placed at the waist of the IC laser beam between mirrors M1 and M2 [both high reflective (HR)], which is located at a distance of approximately 98.5 mm from M1. Mirror M3 was either HR with $R_{M3} > 99.9\%$ (hereinafter referred to as the HR outcoupler) for the broadband tuning measurement or partly transmissive for the MECSEL's wavelengths with $R_{M3} = (95 \pm 1)\%$ (hereinafter referred to as the 5% outcoupler) for all other measurements presented in this Letter. The calculated

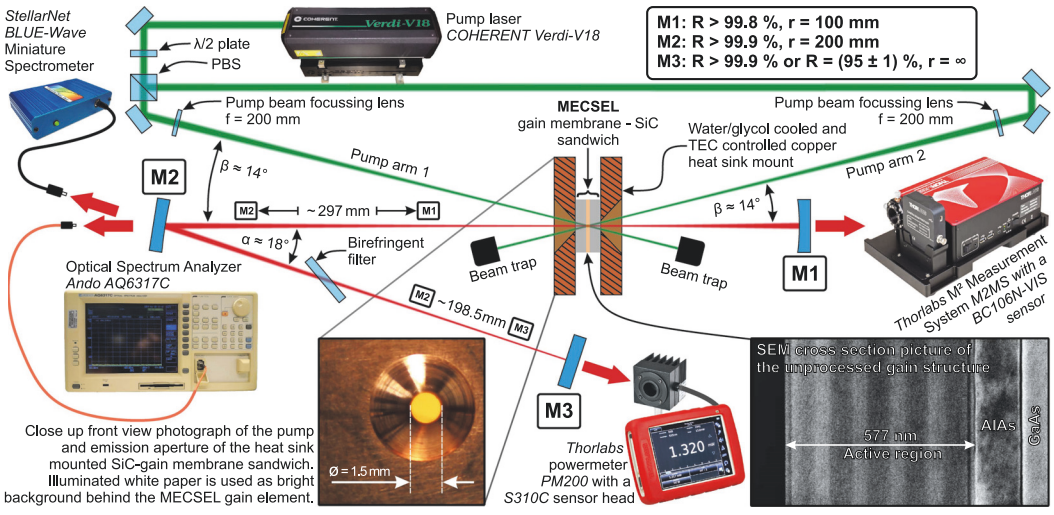

Fig. 1. Detailed schematic drawing of the V-shaped MECSEL setup including the resonator with its mirrors M1, M2, and M3, the pump optics, and the pump beam path, as well as all devices that were used for characterization.

IC beam waist diameter was ~80 μm in the tangential and ~155 μm in the sagittal plane. Therefore, mode matching was achieved for the tangential plane during laser operation. In the sagittal plane, the mode diameter was pump spot limited.

The power transfer behavior was measured for both configurations, SSP and DSP, using a *Thorlabs PM200* with *S310C* sensor head. The output power (P_{out}) results are plotted in Fig. 2 as a function of P_{out} over $P_{abs.,pump}$. For DSP, a slightly smaller pump threshold of 0.69 W was determined compared to SSP via pump arm 1 (PBS was removed) with a threshold of 0.79 W. The maximum output power increased from 3.13 to 3.22 W, and the differential efficiency η_{diff} increased from 31.9% to 34.4% for the DSP configuration. η_{diff} was determined via linearly fitting the data points between 2.5 and 8 W of $P_{abs.,pump}$. In the DSP configuration, the MECSEL reaches its maximum power output slightly earlier than with SSP, but the thermal influence on the slope behavior starts for both configurations at about 8 W of absorbed pump power, from which the output values deviate from the expected linear increase. This was also recently observed by Yang *et al.* [7].

An essential figure of merit enabling us to compare the pump configurations (DSP, SSP arms 1 and 2) and to determine the thermal behavior [12] of the system is the thermal resistance R_{th}. Therefore, spectra were taken whilst power transfer measurements for all pump configurations at the same spot on the sample were performed, determining the spectral shift per change of dissipated power $\Delta\lambda/\Delta P_{diss}$.

P_{diss} was calculated as follows: $P_{diss} = P_{abs.,pump} - P_{out}$. Furthermore, the thermal shift of the laser emission $\Delta\lambda/\Delta T_{hs}$ was measured under constant pumping of $P_{abs.,pump} = 2.53$ W with a duty cycle of 5% to avoid heating effects of the pump laser. The spectra were recorded with a *StellarNet Blue-Wave* spectrometer (resolution limit 0.8 nm). Figure 3 shows the spectral positions of the long wavelength flank at half-maximum of the laser emission plotted over dissipated power P_{diss} and heat sink temperature T_{hs}, respectively. The linear fits applied to the data show the lowest spectral shift per dissipated power of 1.34 nm/W for the DSP configuration. For SSP via pump arms 1 and 2, the spectral shifts per dissipated power are both higher (1.43 nm/W and 1.52 nm/W for SSP arms 1 and 2), but differ slightly. We connect this difference with

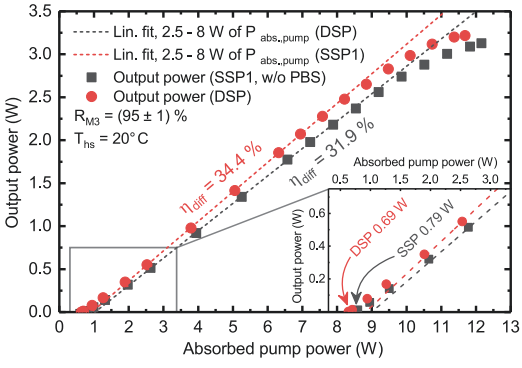

Fig. 2. Power transfer measurements of the free-running MECSEL in SSP (pump arm 1) and DSP configurations. The inset shows an enlarged view of the threshold region.

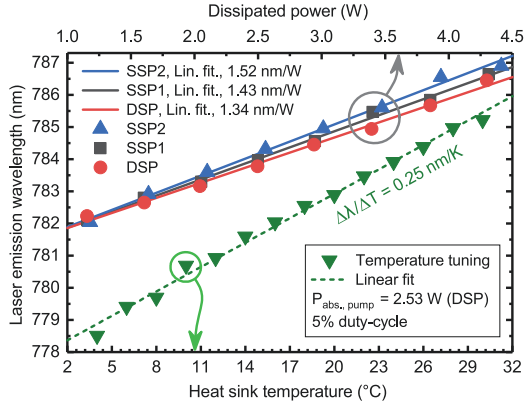

Fig. 3. Spectral shifts of laser emission $\Delta\lambda$ plotted over dissipated power P_{diss} (full squares, circles, and upwards pointing triangles) and heat sink temperature T_{hs} (full downwards pointing triangles) are plotted here.

pump spot sizes that are not identical due to slight variations in the pump lens distances. The heat sink temperature tuning measurements reveal a spectral shift of 0.25 nm/K. The thermal resistance can now be calculated [12] to $R_{th,DSP} = 5.36$ K/W for DSP and, considering the average, $R_{th,\overline{SSP12}} = 5.9$ K/W for SSP.

The spectral tuning was measured using IC birefringent filters and the results are plotted in Fig. 4. Two different filters, 0.5 mm and 2 mm in thickness, were used as the 0.5 mm thick filter with a free spectral range of $\Delta\lambda_{780\,nm} = 136.6$ nm that did not introduce enough losses to properly tune the laser with the 5% outcoupler. A wide tuning range of 44.5 nm from 767.0 to 811.5 nm was determined using the HR outcoupler and the 0.5 mm thick birefringent filter. With the 5% outcoupler and the 2 mm birefringent filter, a tuning range of 22.5 nm was reached, while the laser exceeded 1 W output from 776 to 790 nm with a maximum of 1.61 W at 781.3 nm.

As a further important laser parameter, the beam quality factor M^2 was measured. It revealed a value of $M^2 < 1.09$

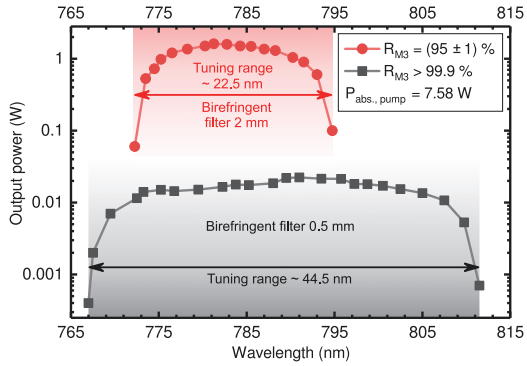

Fig. 4. Tuning measurements at $P_{abs.,pump} = 7.58$ W, taken with the 5% outcoupler and HR outcoupler.

($M_X^2 < 1.134$ and $M_Y^2 < 1.040$, including device inaccuracy of 5%), performed at ~2 W of absorbed pump power with a *Thorlabs M2MS* that was equipped with a *Thorlabs BC106N-VIS* camera. The emitted beam possesses a slight ellipticity of 1:1.19 originating from the V-shape of the resonator, but it was limited by the pump beam diameter as mentioned above.

Determining the spectral emission characteristics of the free-running MECSEL, a high-resolution spectrum was recorded (see Fig. 5) behind mirror M2. For this spectral measurement, an *Ando AQ6317C* optical spectrum analyzer with a resolution limit of 0.02 nm was used. The visible Fabry–Perot resonances, which are equally spaced by $\Delta\lambda \approx 0.32$ nm, are caused by the single SiC heat spreaders. Owing to the excellent thickness homogeneity of the SiC wafer pieces, no beat-node was visible, in difference to other reports where diamond heat spreaders were used [1,6]. The spectral spacing can be connected to the wafer thickness, which is measured to be ~350 μm.

Looking at the power transfer behavior of both pump configurations (Fig. 2) and assuming the pump light absorption follows Beer–Lambert's law, one could explain the lower laser threshold, the improved differential efficiency by 2.5% points, and the slightly higher maximum output power by 90 mW for DSP by the more homogeneous distributed pump light within the active region membrane. A closer look at the thermal rollover point reveals a slightly earlier rollover for the DSP configuration. This could be understood, as the more homogeneous pump distribution also leads to a less strong temperature gradient within the active region, assuming heat is created where absorption takes place. This means that once the gain structure rolls over thermally, this happens more simultaneously within the structure in the DSP configuration. On the other hand, in the SSP configuration, where a stronger thermal gradient can be expected, this side of the gain membrane facing the pump light might experience a slightly earlier rollover than the side turned away from the pump light, and the laser maintains operation up to a slightly higher $P_{\mathrm{abs.,pump}}$ before the thermal shutdown. A stronger thermal gradient could be beneficial for the heat dissipation within the semiconductor membrane and finally into the SiC heat spreaders. Also, sufficient charge carrier diffusion [13] from the hot to the cold side in the semiconductor might partly compensate negative thermal effects. Despite the fact that higher local temperatures inside the gain membrane are present [12] for SSP, which is confirmed by the ~9% higher thermal resistance, the determined differences comparing DSP and SSP in laser threshold, differential efficiency, maximum output power, and thermal rollover are rather small. This already indicates relative good heat removal conditions. The thickness of the gain membrane is obviously small enough, dissipating the introduced heat properly, while not experiencing a huge impact of the different pumping schemes. Due to this, finding an optimum gain membrane thickness containing more QWs, considering pump light absorption and heat dissipation out of the membrane itself, has an additional margin to power scale the presented system.

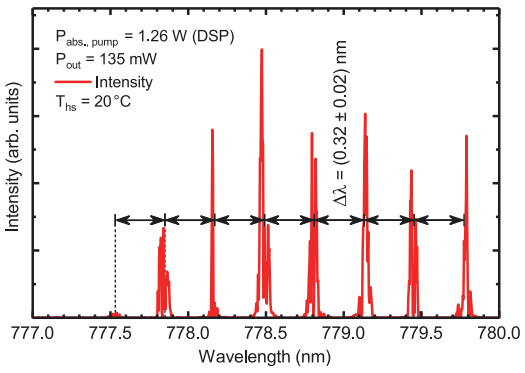

Fig. 5. Typical high-resolution spectrum of the free-running MECSEL is shown here.

In summary, a MECSEL employing SiC heat spreaders for symmetrical cooling was experimentally examined using single/double-side barrier pumping. This MECSEL represents the first one operating at room temperature as well as in DSP configuration. A decrease of 9% in thermal resistance was determined for DSP explained by the 2.8% improved value in maximum output power of 3.22 W, the increase in differential efficiency to 34.4% by 2.5% points, and the reduced absorbed pump power by 12.7% for the laser threshold. The presented laser with a maximum operation range from 767.0 to 811.5 nm and excellent beam quality factor of $M^2 < 1.09$ extends the available range of vertically emitting high-power semiconductor lasers and paves the way for further research on power scaling of MECSELs, where DSP or even multi-pass pumping [10] might become relevant.

Funding. Academy of Finland (315121).

Acknowledgment. The authors thank Marcelo Rizzo Piton for the help with SEM measurements and the Finnish National Agency for Education (EDUFI) for supporting Hoy-My Phung.

REFERENCES

1. H. Kahle, C. M. N. Mateo, U. Brauch, P. Tatar-Mathes, R. Bek, M. Jetter, T. Graf, and P. Michler, Optica **3**, 1506 (2016).
2. J. V. Sandusky and S. R. J. Brueck, IEEE Photon. Technol. Lett. **8**, 313 (1996).
3. M. Kuznetsov, F. Hakimi, R. Sprague, and A. Mooradian, IEEE Photon. Technol. Lett. **9**, 1063 (1997).
4. V. Iakovlev, J. Walczak, M. Gębski, A. K. Sokoł, M. Wasiak, P. Gallo, A. Sirbu, R. P. Sarzała, M. Dems, T. Czyszanowski, and E. Kapon, J. Phys. D **47**, 065104 (2014).
5. Z. Yang, A. R. Albrecht, J. G. Cederberg, and M. Sheik-Bahae, Opt. Express **23**, 33164 (2015).
6. A. Broda, A. Kuźmicz, G. Rychlik, K. Chmielewski, A. Wójcik-Jedlińska, I. Sankowska, K. Gołaszewska-Malec, K. Michalak, and J. Muszalski, Opt. Quantum Electron. **49**, 287 (2017).
7. Z. Yang, D. Follman, A. R. Albrecht, P. Heu, N. Giannini, G. D. Cole, and M. Sheik-Bahae, Electron. Lett. **54**, 430 (2018).
8. S. Mirkhanov, A. H. Quarterman, H. Kahle, R. Bek, R. Pecoroni, C. J. C. Smyth, S. Vollmer, S. Swift, P. Michler, M. Jetter, and K. G. Wilcox, Electron. Lett. **53**, 1537 (2017).
9. S. C. Tidwell, J. F. Seamans, M. S. Bowers, and A. K. Cousins, IEEE J. Quantum Electron. **28**, 997 (1992).
10. C. M. N. Mateo, U. Brauch, H. Kahle, T. Schwarzbäck, M. Jetter, M. A. Ahmed, P. Michler, and T. Graf, Opt. Lett. **41**, 1245 (2016).
11. B. Monemar, K. K. Shih, and G. D. Pettit, J. Appl. Phys. **47**, 2604 (1976).
12. B. Heinen, F. Zhang, M. Sparenberg, B. Kunert, M. Koch, and W. Stolz, IEEE J. Quantum Electron. **48**, 934 (2012).
13. A. H. Quarterman and K. G. Wilcox, Optica **2**, 56 (2015).

PUBLICATION

II

Power scaling and thermal lensing in 825 nm emitting membrane external-cavity surface-emitting lasers

H.-M. Phung, H. Kahle, J.-P. Penttinen, P. Rajala, S. Ranta and M. Guina

Optics Letters **44**(2) (2020), 547–550
DOI: 10.1364/OL.382377

Optics Letters

Power scaling and thermal lensing in 825 nm emitting membrane external-cavity surface-emitting lasers

Hoy-My Phung,* Hermann Kahle, Jussi-Pekka Penttinen, Patrik Rajala, Sanna Ranta, and Mircea Guina

Optoelectronics Research Centre (ORC), Physics Unit/Photonics, Faculty of Engineering and Natural Science, Tampere University, Korkeakoulunkatu 3, 33720 Tampere, Finland
**Corresponding author: hoy-my.phung@tuni.fi*

Received 7 November 2019; revised 13 December 2019; accepted 13 December 2019; posted 16 December 2019 (Doc. ID 382377); published 13 January 2020

We present a membrane external-cavity surface-emitting laser (MECSEL) operating around 825 nm at room temperature. With a tuning range of 22 nm, the MECSEL fills the spectral gap between 810 nm and 830 nm, and extends the wavelength coverage of this category of high-beam-quality semiconductor lasers. For high-power operation, the pump spot size and cavity mode size can be enlarged in MECSELs. We apply this technique and demonstrate power scaling. The maximum output power is increased from 0.7 W to 1.4 W. Investigations on the beam quality reveal thermal lensing with a marginally changing M^2 value close to the diffraction limit.

https://doi.org/10.1364/OL.382377

Vertical external-cavity surface-emitting lasers (VECSELs) are ideal sources for the generation of near diffraction-limited beams [1] in the multi-watt regime [2]. For high output power operation, several techniques were put into practice such as in-well pumping, pump recycling, or optimizing the gain structure design [3–7]. The development of high-power VECSELs was further advanced by using an intracavity heat spreader, such as silicon carbide (SiC) [8] or diamond [9]. Efficient single-side cooling of the gain region could be enabled in this way. The distributed Bragg reflector (DBR) behind the gain mirror consists of multiple semiconductor pairs in order to provide a sufficiently high reflectivity, especially when only low refractive index contrast materials are available. As a result, DBRs are typically a few micrometers thick and have a comparatively small thermal conductivity [10–12]. Therefore, it is beneficial to use an alternative laser architecture in which the gain region is operated in transmission and the DBR function is taken by an external mirror; this allows implementing the double-side cooling for the gain region as recently proposed for membrane external-cavity surface-emitting lasers (MECSELs) [13–15].

The first MECSEL incorporating two diamond heat spreaders was successfully demonstrated in the red spectral range in 2016 [16] and various types of MECSELs were realized [17–20] shortly after. In addition to the more efficient heat dissipation, one further advantage can be seen from the epitaxial point of view. Without the DBR, only lattice matching between the gain region and the substrate needs to be considered, which gives more freedom to various semiconductor material systems.

VECSELs in the 8XX nm wavelength region have been realized for 830 nm to 870 nm [21,22], also with passive mode locking [23] or linewidth narrowing [24,25]. On the short 8XX nm range, a spectral gap was left (illustrated as red area in Fig. 1) although there should be no fundamental limits to realize VECSELs in this wavelength regime.

In this Letter, we present a MECSEL extending the wavelength coverage in the 810 nm to 830 nm filling the gap. With a tuning range of more than 20 nm, such a laser source opens new perspectives in numerous fields. These include biology research, spectroscopy, and metrology, e.g., in water-vapor differential absorption lidar [26], in which a good beam quality is required. The external cavity and optical pumping yield a strong benefit and enable power scaling [27] in a MECSEL with the adjustable pump spot diameter and cavity mode area on the gain membrane. Our investigations focus on two aspects: power scaling and thermal lensing in a MECSEL.

Our MECSEL structure was fabricated by molecular beam epitaxy using a V80H-10 VG Semicon solid source reactor. On top of a 50.8 mm GaAs (100) $\pm$ 0.5° substrate, a GaAs buffer layer was deposited, followed by a 150 nm thick AlAs process layer. The active region had a resonant design for an emission wavelength of 825 nm. It contained nine GaInAsP quantum wells (QWs) that were equally allocated to three groups. GaInP was used for the barrier/spacer layers to achieve a sufficient confinement of the charge carriers. A 20 nm thick AlGaInP window layer enclosed the active region on both sides to prevent electron diffusion to the semiconductor–heat spreader interface. For efficient thermal management, the substrate and the AlAs layer were removed via wet chemical etching [16], and the gain membrane was bonded between a pair of uncoated 4H-SiC heat spreaders. Due to its lower thermal conductivity, SiC is not favorable to diamond. SiC was used here because of its lower cost. A schematic illustration of the experimental setup is shown

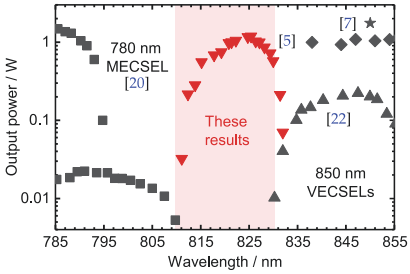

Fig. 1. Realized VECSELs and MECSELs between 785 nm and 855 nm at heat sink temperatures $T_{hs} \geq 10°C$.

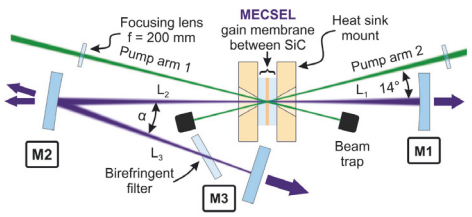

Fig. 2. Schematic illustration of the experimental setup. The used configurations are listed in Table 1.

in Fig. 2. The gain membrane sandwich was mounted to a copper heat sink with indium foil to improve the thermal contact. The heat sink plates were cooled by water/glycol, while the temperature was set and stabilized to 20°C via thermoelectric cooling. A Coherent V-18 laser emitting at 532 nm was used to optically pump the gain membrane from two sides at an incident angle of 14°. The resulting pump spot was slightly elliptical, and its diameters in tangential ($D_{p,tan}$) and sagittal planes ($D_{p,sag}$) were calculated with the measured distance between the lens and the membrane. To obtain the absorbed pump power, the reflected and transmitted powers were subtracted from the incident pump power. The pump absorption for the gain media was about 70% and the reflection about 26% of the incident pump power.

We used two v-shaped cavities (cavity 1 and cavity 2) to characterize the MECSEL at different pump spot and cavity mode diameters. Each cavity was composed of laser mirrors M1, M2, and M3 with the radius of curvature r and the transmission T as listed in Table 1. L_1 denotes the distance between M1 and the membrane, L_2 between membrane and M2, and L_3 between M2 and M3. Accordingly, the cavity was adjusted close to its stability limit, and the membrane was positioned at the beam waist of the cavity. In the small pump spot configuration (cavity 1), the mode diameter ($D_{m,tan}$) was about the same size as the pump diameter in the tangential plane. This was different in the large pump spot configuration (cavity 2). Here, the pump spot diameter was adjusted at the highest deliverable pump power of 18.5 W, and an optimum for high output power was found when the cavity mode diameter was smaller than the pump mode with a ratio of about 0.66 ± 0.14. This value is in very good agreement with the simulated values of Laurain *et al.* [28].

The output power characteristics of the MECSEL using a pump spot diameter of (88 ± 4) µm (cavity 1) and

Table 1. Cavity Configurations with the Radius of Curvature r and Transmission T Given in the Data Sheet[a]

	Cavity 1 with $\alpha \sim 18°$	Cavity 2 with $\alpha \sim 11°$
M1	$r = 100$ mm, $T < 0.2\%$	$r = 250$ mm, $T < 0.2\%$
M2	$r = 200$ mm, $T < 0.1\%$	$r = 300$ mm, $T < 0.1\%$
M3	$r = \infty$, $T = 2.5\%$	$r = \infty$, $T = 2.5\%$, 1.0%, 0.1%
L_1	(98.0 ± 0.5) mm	(248.0 ± 0.5) mm
L_2	(197.0 ± 0.5) mm	(298.0 ± 0.5) mm
L_3	(198.0 ± 0.5) mm	(298.0 ± 0.5) mm
$D_{m,tan}$	(87 ± 18) µm	(127 ± 16) µm
$D_{m,sag}$	(162 ± 6) µm	(173 ± 8) µm
$D_{p,tan}$	(88 ± 4) µm	(209 ± 6) µm
$D_{p,sag}$	(98 ± 5) µm	(234 ± 7) µm

[a]The mode diameter D_m and pump spot diameter D_p are calculated values.

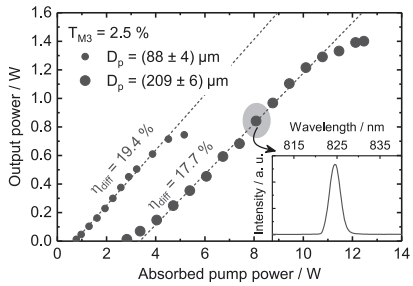

Fig. 3. Performance of the MECSEL operated in cavity 1 and 2 at $T_{hs} = 20°C$. The inset shows the emission spectrum at 8 W absorbed pump power.

(209 ± 6) µm (cavity 2) are compared in Fig. 3. The output power was measured behind M3. In the case of the large pump spot diameter (cavity 2), a significant amount (about 13.3%) of the total output power was coupled out through M1. A possible reason is that the transmission of M1 ($r = 250$ mm, $T < 0.2\%$) in cavity 2 was higher than the value given in the data sheet. Thus, the output from M1 (cavity 2) was always taken into account and added to the total output power, whereas in cavity 1, the output power was not measurable behind M1 ($r = 100$ mm, $T < 0.2\%$).

In the small pump spot configuration (cavity 1), the threshold was reached at an absorbed pump power of 0.77 W. It can be seen that the output power increased linearly, and the maximum output power of about 0.72 W was attained with 4.52 W of absorbed pump power before thermal rollover. In the large pump spot configuration (cavity 2), the threshold increased to 2.83 W and the maximum output power was doubled to 1.4 W. The differential efficiency indeed decreased slightly from 19.4% to 17.7%, but thermal rollover started at a much higher absorbed pump power of 11.45 W, as heat load generated by the pump was spread over a larger area.

A typical emission spectrum of the MECSEL, measured by a StellarNet BLUE-Wave miniature spectrometer, is illustrated in the inset in Fig. 3. It can be seen that the emission is centered at ~825 nm. For tuning the wavelength, a 2 mm thick birefringent filter without temperature control was placed at Brewster's angle between M2 and M3. By rotating the birefringent filter

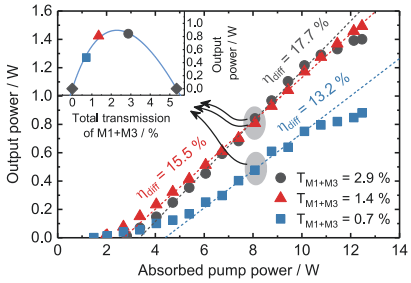

Fig. 4. Performance of the MECSEL with different total transmission values T_{M1+M3} in cavity 2. The inset displays the output power at 8 W absorbed pump power for different T_{M1+M3}.

around the axis normal to its surface, the lasing wavelength could be tuned between 810 nm and 832 nm, as shown in Fig. 1.

For the estimation of internal losses and laser gain in cavity 2, further output characteristics with outcoupling mirror transmission 1.0% and 0.1% were recorded and are displayed in Fig. 4. By including the transmission of M1, the total transmission $T_{M1+\ M3}$ from M1 and M3 corresponded to 1.4% and 0.7%, respectively. In the $T_{M3} = 2.5\%$ configuration, T_{M1+M3} was about 2.9%.

The inset in Fig. 4 illustrates how the performance of the MECSEL varied for all outcoupler transmission values at 8 W absorbed pump power. Two data points with zero output $P_{out} = 0$ W were additionally included to an outcoupler transmission of $T_{M1+M3} = 0\%$ and $T_{M1+M3} = 5.4\%$. The latter case was tested in the setup and no lasing occurred due to the high outcoupling losses. By setting the threshold to $T_{M1+M3} = 5.4\%$, realistic values for the unsaturated gain g_0 per pass were obtained, which was not the case for T_{M1+M3} much lower than 5.4%. A fit function $P_{out} = C \cdot T[g_0/(L_i + T) - 1]$ [29], with a fit parameter C, was used to estimate the unsaturated gain g_0 per pass and the internal losses L_i arising from absorption, scattering, and diffraction. g_0 resulted as $(12.1 \pm 2.7)\%$ and L_i as $(6.8 \pm 2.7)\%$. The fit curve reveals an optimum at $T_{M1+M3} = 2.3\%$. This relatively small value can be related to the small amount of QWs.

The beam quality was studied in cavity 2 with a Thorlabs CCD Camera Beam Profiler BC106N-VIS/M, which was placed behind M1 at a fixed distance. Due to the v-shape of the cavity, the beam profile was elliptical, as shown in Fig. 5. It turned into a nearly circular and smaller spot when the pump power was increased. On the one hand, this change is partly initiated by the growth of the mode diameter with increasing pump power, as the pump laser possesses a Gaussian power distribution. On the other hand, we suspect the thermal lensing setting in [30,31]. The thermal lens can result from heating the gain medium and the heat spreaders. In this case, the pump laser as a Gaussian heat source creates a nonuniform temperature distribution. Associated with the thermo-optical effect, a refractive index gradient effectively acting as a lens is created. Although the thermal lens from the gain medium and the heat spreaders cannot be distinguished in the following M^2 measurements, the thermal lens from the gain medium is expected to take the dominating part [31]. This is because the thermo-optical coefficient in semiconductor materials is typically up to two orders of magnitude larger than in dielectric materials. Furthermore,

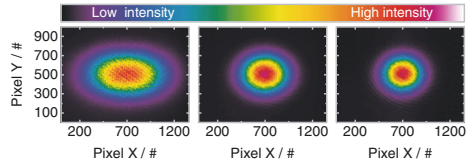

Fig. 5. Beam profile at 3.4 W absorbed pump power with cavity 2 (left). The pump power was increased by a factor of two (center) and three (right).

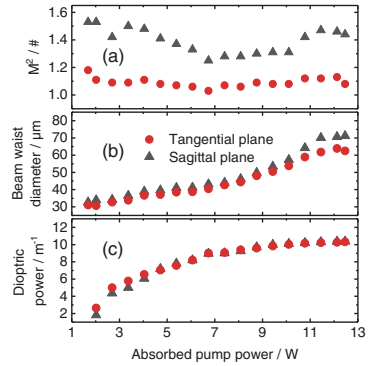

Fig. 6. (a) M^2 and (b) beam waist diameter of the outcoupled beam in the M^2 measurement system. (c) Calculated dioptric power of the thermal lens.

pump power absorption leads to higher temperature rise in the gain medium. To further investigate the effect of thermal lensing, M^2 measurements were performed with a Thorlabs M^2 Measurement System M2MS. The M^2 value of about 1.1 in the tangential plane did not change substantially, as shown in Fig. 6(a). A decrease in the M^2 value in the sagittal plane is visible between laser threshold and 7 W absorbed pump power. This change is a matter of the thermal gradient, which gets stronger in this pump power regime. However, the M^2 value increases when the absorbed pump power exceeds 7 W. It should be noted that there might be a loss of the thermal gradient because the high temperature area on the membrane grows with absorbed pump power. As the beam parameter product remained nearly unaffected, it was consistent that the beam divergence angle decreased from 2.5° to 1.1°, and the beam waist diameter created inside the M^2 measurement system enlarged from 33 µm to 71 µm, as shown in Fig. 6(b).

The dioptric power of the thermal lens was estimated by a ray matrix algorithm that simulates the mode diameter of the Gaussian beam within the MECSEL cavity [32,33]. A thin biconvex lens in the simulation was directly positioned in front of the SiC heat spreader. It was assumed that the thin lens changes the intracavity and the external beam divergence angle by the same factor. For the external beam, we used the beam divergence angle near threshold at which the thermal lensing effect was weakest as a reference. The resulting dioptric power of the thermal lens is illustrated in Fig. 6(c) and saturated at about (10.3 ± 0.1) m^{-1}. This reveals that the thermal gradient does not alter much before thermal rollover.

To clarify whether the thermal lens can be attributed to the thermo-optical effect, we calculated the dioptric power by considering the refractive index rise at the optical center of the lens. The thermo-optical coefficient for identifying the refractive index rise was indeed not measured, but for simplification, it was assumed that the gain membrane consists only of GaInP with a linear thermo-optical coefficient of $\sim(2.0 \pm 0.3) \cdot 10^{-4}$ K^{-1} [34]. The temperature rise from laser threshold to thermal rollover was about $\Delta T = 46.83$ K according to the calculated thermal resistance of $R_{\mathrm{th}} = 4.09$ K/W originating from spectral shift measurements of the MECSEL emission [35]. The refractive index value at the optical center of the lens was calculated by summing up the refractive index of GaInP and the refractive index rise. For the refractive index profile, the following assumptions were made: according to the Gaussian heat source, 87% of the heat is concentrated mainly within the full width at half maximum [30] allowing quadratic approximations for small radial distances. This relation was adapted to describe the refractive index in variation with distance from the optical center. This yields a dioptric power of about (8.4 ± 2.2) m^{-1}, which is on the same order of magnitude as in the experimental findings. In the future, the appearance of thermal lensing with different pump spot diameters, mode ratios, heat spreader materials, and thicknesses [31] could be analyzed, which could be important for future semiconductor disk laser development. Also relevant are separate thermal lensing effects from a single standing membrane or the heat spreader itself.

In conclusion, a room temperature operating MECSEL providing wavelength coverage from 810 nm to 832 nm was demonstrated. The near diffraction-limited M^2 value remained nearly unchanged in the presence of thermal lensing. The power scalability of a MECSEL was shown by increasing the cavity mode and pump spot diameter. The results revealed only a small decrease in the differential efficiency, and in turn, the maximum output power could be doubled to 1.4 W. The pump spot diameter we used was about 209 μm. This is lower than what is usually used in VECSELs, and it can further be increased. Moreover, thicker SiC or diamond heat spreaders and an outcoupling mirror with optimal transmission value can be used to achieve even higher output power. Additionally, the pump laser should not be necessarily a diffraction-limited diode-pumped solid-state laser. High-power laser diodes in combination with the technique of power scaling can be applied to further push the limits of this new category of semiconductor lasers to higher powers with much lower cost.

Funding. Academy of Finland (315121, 320168, 326443); Opetushallitus; PREIN Flagship Programme.

Disclosures. The authors declare no conflicts of interest.

REFERENCES

1. M. Kuznetsov, F. Hakimi, R. Sprague, and A. Mooradian, IEEE Photon. Technol. Lett. **9**, 1063 (1997).
2. M. Guina, A. Rantamäki, and A. Härkönen, J. Phys. D **50**, 383001 (2017).
3. M. Schmid, S. Benchabane, F. Torabi-Goudarzi, R. Abram, A. I. Ferguson, and E. Riis, Appl. Phys. Lett. **84**, 4860 (2004).
4. W. Zhang, T. Ackemann, S. McGinily, M. Schmid, E. Riis, and A. I. Ferguson, Appl. Opt. **45**, 7729 (2006).
5. S.-S. Beyertt, U. Brauch, F. Demaria, N. Dhidah, A. Giesen, T. Kübler, S. Lorch, F. Rinaldi, and P. Unger, IEEE J. Quantum Electron. **43**, 869 (2007).
6. S. J. McGinily, R. H. Abram, K. S. Gardner, E. Riis, A. I. Ferguson, and J. S. Roberts, IEEE J Quantum Electron. **43**, 445 (2007).
7. Y. Bai, Z. Xu, Y. Lin, J. Wisdom, C. Scholz, E. Weiss, J. Chilla, and A. Diening, Proc. SPIE **10515**, 105150E (2018).
8. J. E. Hastie, C. W. Jeon, D. Burns, J.-M. Hopkins, S. Calvez, R. Abram, and M. D. Dawson, *15th Annual Meeting of the IEEE Lasers and Electro-Optics Society* (2002), pp. 329–330.
9. J.-M. Hopkins, S. A. Smith, C. W. Jeon, H. D. Sun, D. Burns, S. Calvez, M. D. Dawson, T. Jouhti, and M. Pessa, Electron. Lett. **40**, 30 (2004).
10. J. Piprek, T. Tröger, B. Schröter, J. Kolodzey, and C. S. Ih, IEEE Photon. Technol. Lett. **10**, 81 (1998).
11. P. Zhang, R. Zhu, M. Jiang, Y. Song, D. Zhang, and Y. Cui, Opt. Laser Technol. **96**, 259 (2017).
12. Y. Huo, C. Y. Cho, K. F. Huang, Y. F. Chen, and C. C. Lee, Opt. Lett. **44**, 327 (2019).
13. J. V. Moloney, J. Hader, and S. W. Koch, Proc. SPIE **6871**, 687113 (2008).
14. V. Iakovlev, J. Walczak, M. Gębski, A. K. Sokoł, M. Wasiak, P. Gallo, A. Sirbu, R. P. Sarzała, M. Dems, T. Czyszanowski, and E. Kapon, J. Phys. D **47**, 065104 (2014).
15. Z. Yang, A. R. Albrecht, J. G. Cederberg, and M. Sheik-Bahae, Opt. Express **23**, 33164 (2015).
16. H. Kahle, C. M. N. Mateo, U. Brauch, P. Tatar-Mathes, R. Bek, M. Jetter, T. Graf, and P. Michler, Optica **3**, 1506 (2016).
17. A. Broda, A. Kuźmicz, G. Rychlik, K. Chmielewski, A. Wójcik-Jedlińska, I. Sankowska, K. Gołaszewska-Malec, K. Michalak, and J. Muszalski, Opt. Quantum Electron. **49**, 287 (2017).
18. Z. Yang, D. Follman, A. R. Albrecht, P. Heu, N. Giannini, G. D. Cole, and M. Sheik-Bahae, Electron. Lett. **54**, 430 (2018).
19. S. Mirkhanov, A. H. Quarterman, H. Kahle, R. Bek, R. Pecoroni, C. J. C. Smyth, S. Vollmer, S. Swift, P. Michler, M. Jetter, and K. G. Wilcox, Electron. Lett. **53**, 1537 (2017).
20. H. Kahle, J.-P. Penttinen, H.-M. Phung, P. Rajala, A. Tukiainen, S. Ranta, and M. Guina, Opt. Lett. **44**, 1146 (2019).
21. M. A. Holm, D. Burns, P. Cusumano, A. I. Ferguson, and M. D. Dawson, Appl. Opt. **38**, 5781 (1999).
22. J. E. Hastie, J.-M. Hopkins, S. Calvez, C. W. Jeon, D. Burns, R. Abram, E. Riis, A. I. Ferguson, and M. D. Dawson, IEEE Photon. Technol. Lett. **15**, 894 (2003).
23. K. G. Wilcox, Z. Mihoubi, S. Elsmere, A. Quarterman, H. D. Foreman, S. Hashimoto, T. Südmeyer, U. Keller, and A. Tropper, Electron. Lett. **44**, 1469 (2008).
24. M. A. Holm, D. Burns, A. I. Ferguson, and M. D. Dawson, IEEE Photon. Technol. Lett. **11**, 1551 (1999).
25. B. Cocquelin, G. Lucas-Leclin, D. Holleville, N. Dimarcq, I. Sagnes, A. Garnache, and P. Georges, *International Conference on Space Optics* (2008).
26. G. Wagner, A. Behrendt, V. Wulfmeyer, F. Späth, and M. Schiller, Appl. Opt. **52**, 2454 (2013).
27. M. Guina, A. Härkönen, V.-M. Korpijärvi, T. Leinonen, and S. Suomalainen, Adv. Opt. Technol. **2012**, 1 (2012).
28. A. Laurain, J. Hader, and J. V. Moloney, J. Opt. Soc. Am. B **36**, 847 (2019).
29. A. Yariv and P. Yeh, *Photonics: Optical Electronics in Modern Communications*, The Oxford Series in Electrical and Computer Engineering (Oxford University, 2006).
30. J. P. Gordon, R. C. C. Leite, R. S. Moore, S. P. S. Porto, and J. R. Whinnery, J. Appl. Phys. **36**, 3 (1965).
31. A. J. Kemp, A. J. Maclean, J. E. Hastie, S. A. Smith, J.-M. Hopkins, S. Calvez, G. J. Valentine, M. D. Dawson, and D. Burns, Appl. Phys. B **83**, 189 (2006).
32. A. E. Siegman, *Lasers* (University Science Books, 1986).
33. D. Lorenser, D. J. H. C. Maas, H. J. Unold, A.-R. Bellancourt, B. Rudin, E. Gini, D. Ebling, and U. Keller, IEEE J. Quantum Electron. **42**, 838 (2006).
34. S. G. Sokolov, J. L. Lian, S. Combrie, A. De Rossi, and A. P. Mosk, Appl. Opt. **56**, 3219 (2017).
35. B. Heinen, F. Zhang, M. Sparenberg, B. Kunert, M. Koch, and W. Stolz, IEEE J. Quantum Electron. **48**, 934 (2012).

PUBLICATION III

Quantum dot membrane external-cavity surface-emitting laser at 1.5 µm

H.-M. Phung, P. Tatar-Mathes, C. Paranthoën, C. Levallois, N. Chevalier, M. Perrin, A. Kerchaoui, H. Kahle, M. Alouini and M. Guina

Applied Physics Letters **118**(23) (2021), 231101
DOI: 10.1063/5.0053961

Applied Physics Letters

Quantum dot membrane external-cavity surface-emitting laser at 1.5 μm

Cite as: Appl. Phys. Lett. **118**, 231101 (2021); https://doi.org/10.1063/5.0053961
Submitted: 13 April 2021 . Accepted: 25 May 2021 . Published Online: 07 June 2021

H.-M. Phung, P. Tatar-Mathes, C. Paranthoën, C. Levallois, N. Chevalier, M. Perrin, A. Kerchaoui, H. Kahle, M. Alouini, and M. Guina

Applied Physics Letters ARTICLE scitation.org/journal/apl

Quantum dot membrane external-cavity surface-emitting laser at 1.5 μm

Cite as: Appl. Phys. Lett. **118**, 231101 (2021); doi: 10.1063/5.0053961
Submitted: 13 April 2021 · Accepted: 25 May 2021 ·
Published Online: 7 June 2021

H.-M. Phung,[1,a] P. Tatar-Mathes,[1] C. Paranthoën,[2] C. Levallois,[2] N. Chevalier,[2] M. Perrin,[2] A. Kerchaoui,[2] H. Kahle,[1] M. Alouini,[2] and M. Guina[1]

AFFILIATIONS

[1]Optoelectronics Research Centre (ORC), Physics Unit/Photonics, Faculty of Engineering and Natural Science, Tampere University, Korkeakoulunkatu 3, 33720 Tampere, Finland
[2]Institut FOTON, UMR-CNRS 6082, Institut National des Sciences Appliquées de Rennes, University of Rennes, 35700 Rennes, France

[a]Author to whom correspondence should be addressed: hoy-my.phung@tuni.fi

ABSTRACT

A membrane external-cavity surface-emitting laser (MECSEL) with an InAs/InP quantum dot (QD) based gain region is demonstrated. The pumping scheme employs a 90° off-axis parabolic mirror to focus the diode laser pump beam to a nearly circular pump spot. With this pump arrangement, the QD MECSEL with SiC heat spreaders produced 320 mW output power at room temperature with direct emission in the near-infrared at 1.5 μm. We report a record value of 86 nm for the tuning range at this wavelength region, owing to a broad QD gain bandwidth and wide tunability in MECSELs.

Vertical-external-cavity surface-emitting lasers (VECSELs)[1] have emerged as a versatile platform for high-power coherent light sources with high beam quality. In terms of operation principles and cavity architecture, VECSELs integrate the major benefits of thin-disk solid-state lasers as well as semiconductor lasers. The high-quality beam is rendered possible by the external cavity, while the semiconductor bandgap engineering enables wavelength versatility in a broad range. The key element of a VECSEL is the semiconductor gain mirror, which typically consists of a multi-quantum well (QW) or multi-quantum dot (QD) gain structure and a monolithically integrated distributed Bragg reflector (DBR). To achieve gain and enable lasing, such a gain mirror, which is incorporated in the external cavity configuration, is typically pumped optically. Although semiconductor gain media ensure a much broader wavelength coverage compared to solid-state lasing materials, the power capability and wavelength coverage of VECSELs are neither equally distributed nor available at all possible wavelengths covered by typical III–V compound semiconductors. There are various reasons behind this state of fact, ranging from the maturity of technology at certain wavelengths to more profound ones related to intrinsic features of the material systems used.

For example, owing to the mature development stage of the InGaAs/AlGaAs material system, ensuring a high reflectivity, high carrier confinement, and relatively good thermal conductivity, the highest power VECSELs have been demonstrated at around 1 μm.[2,3] However, if one moves away from this wavelength range requiring different material systems,[4] either the DBR, the carrier confinement, thermal conductivity, or a combination of these features will become increasingly difficult to manage. Simplifying this analysis, we can point out the limitation arising from the DBR, which requires specific layers with a reasonable high refractive index contrast and also being compatible in terms of lattice constant with the QW or QD gain heterostructure. These features are readily available for the 1 μm region but become an issue when targeting lasing in the 1.3–1.5 μm region, where the QWs are InP-based rendering impossible the use of GaAs/AlGaAs DBRs. To overcome the spectral limitations of the DBR and to some extent also improve the operation of the gain heterostructure by better thermal management, an alternative laser concept has emerged, the membrane external-cavity surface-emitting laser (MECSEL).[5–7] In MECSELs, the gain medium is comprised only of the thin QW or QD heterostructure (without a DBR), which is then used in an external cavity architecture. Moreover, in MECSELs, the thermal management is more efficient as the active structure can be bonded between two intra cavity heat spreaders,[8] i.e., it is cooled from both sides with heat spreaders in the close proximity of the gain region. In turn, this

enables us to use heat-spreading materials with lower conductivity but more cost-effective as silicon carbide (SiC). Owing to these advantages, recent efforts have led to the demonstration of MECSELs emitting in the red and near-infrared.[9–15]

In this paper, we focus our attention on the important 1.5 μm telecom region, where the DBR technology is particularly difficult due to the low refractive index contrast of InP-based materials. For the sake of generality, we point out that although 1.5 μm monolithic InP-based VECSELs have been demonstrated,[16–19] the highest output power reported at room temperature operation is only 140 mW,[16] which is a small fraction of what would be available at 1 μm. We note here that the thermal resistance of this VECSEL, measured under laser operation, is as high as 470 K/W.[17] To have a better thermal resistance of 34 K/W, a hybrid metal-metamorphic AlAs/GaAs DBR has been implemented.[18] Alternative demonstrations, involving GaInAsN/GaAs QWs and AlAs/GaAs DBR pairs grown on GaAs, have also resulted in rather low output power in the 80 mW range.[19] An alternative solution to the monolithic approach is to grow the InP-based active structure and the AlAs/GaAs DBR separately on two different types of substrates, and afterwards combining them via wafer-fusion.[20–22] This involves a higher level of complexity. Nevertheless, this technique has enabled to fabricate high-power VECSELs exceeding 3.65 W at 1.55 μm.[23] In this Letter, we demonstrate a MECSEL with InAs QDs at an emission wavelength of 1.5 μm. In particular, we demonstrate wavelength tuning over a large bandwidth. The laser implemented an optical pumping scheme[24] to favor an almost circular pumping.

The QD MECSEL structure was grown by gas source molecular beam epitaxy (GSMBE) on a 300 μm thick InP substrate with a (311)B crystal orientation. First, a 100 nm thick InGaAs etch stop layer was fabricated. The gain structure consisted of 20 InAs QD layers separated by 15 nm thick GaInAsP barrier layers and distributed over groups of five QD layers with InP cladding layers as schematically illustrated in Fig. 1.

The structure has been designed with a fixed number of QD layers per groups. To optimize the structure in terms of charge carrier distribution, an increase in the thickness of the GaInAsP barrier absorbing layers compensated for the exponential decrease in the input pump absorption. As a consequence, the total thicknesses of the absorbing layers from the back up to the front side are as follows: 240, 160, 120, and 90 nm. The whole structure appears, thus, as asymmetric, but is still resonant with a 2.5λ design because of the InP/SiC interface. Here, the InP cladding layer between the first and second QD layers is more than twice thicker than the other InP cladding layers in the gain structure. The antinode between these two QD layers is practically left out, such that each QDs group is carefully positioned at stationary field antinodes. Details of the QD fabrication by the Stranski–Krastanow growth mode, the gain structure and its laser performance as a VECSEL at 14 °C employing intra cavity diamond heat spreaders have been described elsewhere.[22]

After the growth was completed, the substrate was mechanically thinned before being removed wet-chemically with an HCl solution. An H_3PO_4:H_2O_2:H_2O solution was applied to eliminate the InGaAs process layer. After the etching process, the membrane was bonded between two uncoated 4H SiC heat spreader pieces and mounted into a copper heat sink. During all operation conditions, the membrane heat spreader sandwich was cooled in a heat sink mount via water/glycol cooling at a temperature of 19 °C. A schematic illustration of the V-cavity for the output power and wavelength tuning experiments performed is shown in Fig. 1. The V-cavity consisted of a plane outcoupling mirror M3, and two curved high-reflecting mirrors M1 and M2, which both had the same reflectivity of $R_{M1,M2} > 99.8$ % and the same radius of curvature of $r_{M1,M2} = 200$ mm. The mirror distances of M1 and M2 to the gain membrane sandwich were adjusted to $L_1 = 195$ mm and $L_2 = 199$ mm. M3 was positioned under an opening angle of 11° between L_2 and L_3. The distance between M2 and M3 was $L_3 = 199$ mm. The calculated cavity mode diameter on the gain membrane was about 200 μm using the ray transfer method for a Gaussian beam. A 980 nm LIMO diode laser coupled into a multimode fiber with a 200 μm core diameter and a numerical aperture of 0.22 was used as a pump source. The fiber output was collimated by a $f = 100$ mm plano–convex lens and focused onto a spot size of about 360 μm in diameter by a 90° off-axis parabolic mirror (MPD249H-M01 from Thorlabs) with a protected gold reflection coating ($R_{980nm} > 98$ %) and a reflected focal length of 101.6 mm. Thus, the ratio between the cavity and pump mode diameter was about 0.56. It is lower than the suggested optimum from 0.65 to 0.82 simulated by Laurain *et al.*[25] The parabolic mirror used in these experiments has a diameter of 50.8 mm as well as a hole with a diameter of 3 mm that is large enough and does not cut the laser mode. The pump beam covered almost the whole area of the parabolic mirror. For the pump beam, the losses caused by this 3 mm hole were investigated and were below 1% and, therefore, negligible. With an angle of incidence of the pump laser ranges from almost 0° to less than 15°, this pump approach enables a nearly circular pump spot with $D_{p,sag}/D_{p,tan} > 0.96$ in the focus. In particular, the pump efficiency can be enhanced by having similar mode shapes (see Fig. 1).

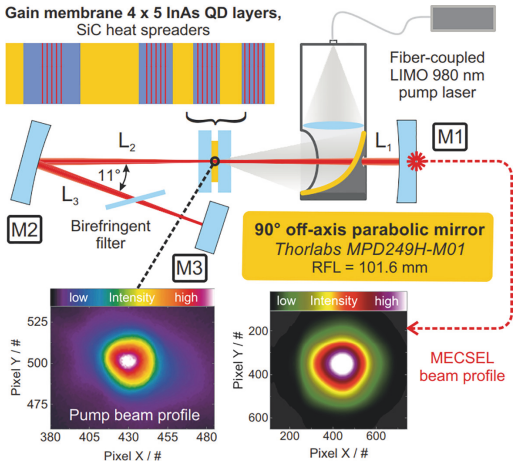

FIG. 1. Experimental setup of the MECSEL employing 4 × 5 InAs/InP QD layers and a V-cavity. By using a 90° off-axis parabolic mirror with a high-reflection protected gold coating, the pump beam is focused down to a nearly circular pump spot onto the laser-active membrane as illustrated. This also favors an almost round beam profile of the MECSEL as captured by a scanning slit beam profiler.

Following the Fresnel equations, approximately 20% of incident pump power was reflected at the SiC heat spreader front surface for incident angles between 0° and 15°. Pump transmission measurements revealed an absorption by the gain membrane of about 65% of the incident pump power.

The QD MECSEL output characteristics are shown as a function of the absorbed pump power in Fig. 2 and include the transmission from M1, M2, and M3 with an outcoupler reflectivity of $R_{M3} = 99\,\%$.

Lasing was achieved with a threshold pump power of $P_{pump,thr.} = 4.7$ W. By increasing the pump power further to a value of 22.6 W of absorbed power, a maximum output power of 320 mW was obtained with a differential efficiency of 2%. As can be seen in Fig. 2, the output power was limited by thermal rollover, which was setting in at about 22 W absorbed pump power. The QD MECSEL produced a near diffraction limited fundamental transverse mode profile, in both, sagittal and tangential planes with an M^2 value of less than 1.05, measured with a dual scanning-slit BP209-IR/M beam profiler and a Thorlabs M^2 M2MS measurement system. As can be seen in Fig. 1, the MECSEL beam profile reproduced from the scanning-slit measurement was nearly circular, which is most likely favored by the circular pump approach.

A set of spectra was simultaneously recorded with an Ando AQ6317C optical spectrum analyzer with a resolution of 0.02 nm during the output power measurements. In addition to the spectral red shift, the emission spectrum widened with pump power. This was probably due to the state-filling effect in QDs,[26] as the threshold of higher emission energy modes could be reached at high excitation power and contribute to lasing. The inset in Fig. 2 shows an emission spectrum at 21 W absorbed pump power. It contained typical Fabry–Pérot resonances, related to the spectral filtering induced by the 350 μm thick intra cavity SiC heat spreaders.

Furthermore, the spectral red shift by heating up the gain membrane by the pump source was determined as 0.16 nm/W. The emission spectra shifted on average by 0.07 nm/K with the heat sink temperature. Correspondingly, the thermal resistance[27] is obtained. The value of 2.3 K/W is more than one order of magnitude lower than in monolithic InP VECSELs[17,18] and rather in the same order of magnitude as the 1.77 μm-emitting MECSEL with a QW-based active region.[14]

Tuning experiments have been conducted by inserting a birefringent filter within the cavity (see Fig. 1) using different output coupler reflectivities. This 1.5 mm thick filter enables to cover a large free spectral range of 180 nm. With a $R_{M3} = 99\,\%$ outcoupler, the emission wavelength was tunable from 1474 nm to 1519 nm as illustrated in Fig. 3. The broader tuning range of 86 nm was achievable with a high-reflecting $R_{M3} > 99.8\,\%$ outcoupling mirror. Compared to earlier 1.5 μm VECSELs,[21,22] the highest tuning range has been achieved at the 1.5 μm wavelength band, here, in this work.

The polarization behavior of the QD MECSEL was analyzed without any intra cavity elements inside a linear cavity to avoid any preferred polarization that would be given by a V-cavity. The mirrors M1 and M2 with the mirror distances of about $L_1 = L_2 = 197$ mm were used. An ultra broad band wire grid polarizer from Thorlabs (WP25M-UB) with an extinction ratio of 1000:1 was set behind M2. With the transmission axis fixed at 0° (p-polarization) axis and 90° (s-polarization) axis, the measured output power curve was linearly increasing with pump power as shown in Fig. 4 without power drop. Also, the spectra taken at both polarization axes at an absorbed pump power of 16.4 W in the inset of Fig. 4 revealed that there was no wavelength hopping.

To determine the degree of linear polarization (DOP), the polarizer was rotated over a full cycle. The DOP was calculated with the maximum and minimum output power P_{max} and P_{min} from M2 transmitted through the polarizer by

$$DOP = \frac{P_{max} - P_{min}}{P_{max} + P_{min}}.$$

As can be seen in Fig. 5, the DOP was calculated to be larger than 99%, meaning that the MECSEL was almost fully s-polarized. In VECSELs, similar values have been obtained.[28] The preferential polarization state was fixed at lasing. No switching over the wafer and the whole output power characteristic was observed. This originates most likely from the QD anisotropy, similarly to the recently reported VCSELs integrating the same 1.5 μm InAs QDs.[29]

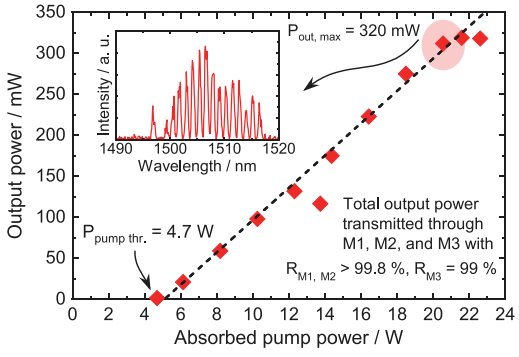

FIG. 2. Power performance of the 1.5 μm QD MECSEL using SiC heat spreaders at 19 °C cooling water temperature. The plotted output power is a sum of transmitted power from M1, M2, and M3. A spectrum at 21 W pump power absorption is illustrated in the inset.

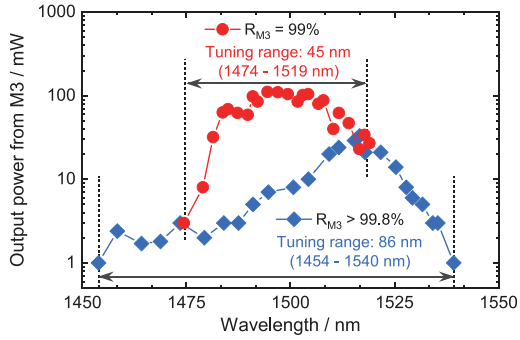

FIG. 3. Wavelength tuning results of the QD MECSEL by tilting a 1.5 mm thick intra cavity birefringent filter at 16.4 W absorbed pump power.

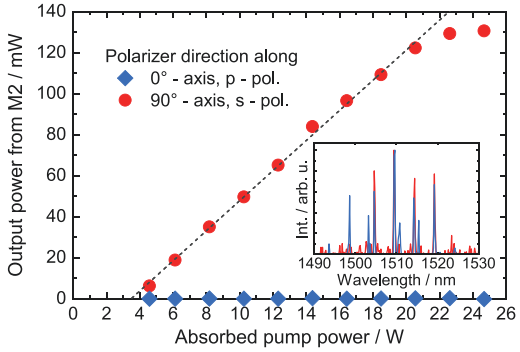

FIG. 4. Polarization output power characteristics recorded at two orthogonal angles of the polarizer transmission axis from a linear cavity with the corresponding spectra in the inset. The spectra are normalized in intensity and measured at an absorbed pump power of 16.4 W.

In conclusion, we demonstrated a QD MECSEL operating at 1.5 μm. With the combination of the broad gain of InAs QDs and the absence of the DBR,[30] the MECSEL has made a record tuning range of 86 nm, which is higher than the gain structure provides as a VECSEL.[21,22] Over 320 mW of output power was achieved at room temperature with relatively low cost SiC heat spreaders available in wafer quality. To optically pump the gain membrane under small pump incident angles below 15° with an almost circular pump spot, a 90° off-axis parabolic mirror was integrated in the pump optics. In the future, this pump approach could be extended by a second set of pump optics, positioned on the opposite side of the MECSEL for double-side pumping[11] or pump recycling[31] by reflecting the transmitted pump beam back to the MECSEL structure to increase the pump efficiency. Additionally, a high DOP larger than 99% was obtained where the s-polarized modes were far more prominent than the p-polarized ones, which was reproducible across the sample. From the application point of view, QD MECSELs with a near diffraction limited beam with an M^2 value of less than 1.05 and a broad gain bandwidth could be applied in coherent Doppler LIDAR[32] in the future for wind velocity sensing, wind turbulence measurements,[33] or wake vortices detection created by aircrafts in flight formations.[34]

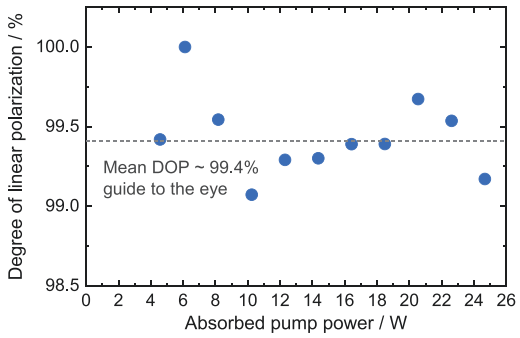

FIG. 5. Calculated degree of polarization of a QD MECSEL recorded in a linear cavity.

The authors acknowledge the Academy of Finland (No. 326455), the PREIN Flagship Programme, the Magnus Ehrnrooth Foundation, the Finnish Foundation for Technology Promotion, and the French National Agency of Research (ANR IDYLIC Project, Grant No. ANR-15-CE24-0034-01) for the funding. The authors would like to acknowledge RENATECH+ (the French national network of facilities for micronanotechnology) with NanoRennes platform for the sample growth.

DATA AVAILABILITY

The data that support the findings of this study are available from the corresponding author upon reasonable request.

REFERENCES

[1]M. Kuznetsov, F. Hakimi, R. Sprague, and A. Mooradian, "High-power (>0.5-W CW) diode-pumped vertical-external-cavity surface-emitting semiconductor lasers with circular TEM_{00} beams," IEEE Photonics Technol. Lett. **9**, 1063–1065 (1997).
[2]E. Kantola, J.-P. Penttinen, S. Ranta, and M. Guina, "72-W vertical-external-cavity surface-emitting laser with 1180-nm emission for laser guide star adaptive optics," Electron. Lett. **54**, 1135–1137 (2018).
[3]B. Heinen, T.-L. Wang, M. Sparenberg, A. Weber, B. Kunert, J. Hader, S. W. Koch, J. V. Moloney, M. Koch, and W. Stolz, "106 W continuous-wave output power from vertical-external-cavity surface-emitting laser," Electron. Lett. **48**, 516–517 (2012).
[4]M. Guina, A. Härkönen, V.-M. Korpijärvi, T. Leinonen, and S. Suomalainen, "Semiconductor disk lasers: Recent advances in generation of yellow-orange and mid-IR radiation," Adv. Opt. Technol. **2012**, 1.
[5]H. Kahle, C. M. N. Mateo, U. Brauch, P. Tatar-Mathes, R. Bek, M. Jetter, T. Graf, and P. Michler, "Semiconductor membrane external-cavity surface-emitting laser (MECSEL)," Optica **3**, 1506–1512 (2016).
[6]V. Iakovlev, J. Walczak, M. Gębski, A. K. Sokoł, M. Wasiak, P. Gallo, A. Sirbu, R. P. Sarzała, M. Dems, T. Czyszanowski, and E. Kapon, "Double-diamond high-contrast-gratings vertical external cavity surface emitting laser," J. Phys. D: Appl. Phys. **47**, 065104 (2014).
[7]Z. Yang, A. R. Albrecht, J. G. Cederberg, and M. Sheik-Bahae, "Optically pumped DBR-free semiconductor disk lasers," Opt. Express **23**, 33164–33169 (2015).
[8]Z. Yang, D. Follman, A. R. Albrecht, P. Heu, N. Giannini, G. D. Cole, and M. Sheik-Bahae, "16 W DBR-free membrane semiconductor disk laser with dual-SiC heatspreader," Electron. Lett. **54**, 430–432 (2018).
[9]A. Broda, A. Kuźmicz, G. Rychlik, K. Chmielewski, A. Wójcik-Jedlińska, I. Sankowska, K. Gołaszewska-Malec, K. Michalak, and J. Muszalski, "Highly efficient heat extraction by double diamond heat-spreaders applied to a vertical external cavity surface-emitting laser," Opt. Quantum Electron. **49**, 287 (2017).
[10]S. Mirkhanov, A. H. Quarterman, H. Kahle, R. Bek, R. Pecoroni, C. J. C. Smyth, S. Vollmer, S. Swift, P. Michler, M. Jetter, and K. G. Wilcox, "DBR-free semiconductor disc laser on SiC heatspreader emitting 10.1 W at 1007 nm," Electron. Lett. **53**, 1537–1539 (2017).
[11]H. Kahle, J.-P. Penttinen, H.-M. Phung, P. Rajala, A. Tukiainen, S. Ranta, and M. Guina, "Comparison of single-side and double-side pumping of membrane external-cavity surface-emitting lasers," Opt. Lett. **44**, 1146–1149 (2019).
[12]H.-M. Phung, H. Kahle, J.-P. Penttinen, P. Rajala, S. Ranta, and M. Guina, "Power scaling and thermal lensing in 825 nm emitting membrane external-cavity surface-emitting lasers," Opt. Lett. **45**, 547–550 (2020).
[13]B. Jeżewski, A. Broda, I. Sankowska, A. Kuźmicz, K. Gołaszewska-Malec, K. Czuba, and J. Muszalski, "Membrane external-cavity surface-emitting laser emitting at 1640 nm," Opt. Lett. **45**, 539–542 (2020).

[14]A. Broda, B. Jeżewski, M. Szymański, and J. Muszalski, "High-power 1770 nm emission of a membrane external-cavity surface-emitting laser," IEEE J. Quantum Electron. **57**, 1–6 (2021).
[15]D. Priante, M. Zhang, A. R. Albrecht, R. Bek, M. Zimmer, C. Nguyen, D. Follman, G. D. Cole, and M. Sheik-Bahae, "Demonstration of a 20 W membrane-external-cavity surface-emitting laser for sodium guide star applications," Electron. Lett. **57**, 337 (2021).
[16]H. Lindberg, A. Larsson, and M. Strassner, "Single-frequency operation of a high-power, long-wavelength semiconductor disk laser," Opt. Lett. **30**, 2260–2262 (2005).
[17]C. Symonds, I. Sagnes, J.-L. Oudar, S. Bouchoule, A. Garnache, J. Berggren, and M. Strassner, "Room temperature CW lasing operation of monolithically grown 1.55 μm vertical external cavity surface emitting laser," Opt. Commun. **230**, 419–423 (2004).
[18]J.-P. Tourrenc, S. Bouchoule, A. Khadour, J.-C. Harmand, A. Miard, J. Decobert, N. Lagay, X. Lafosse, I. Sagnes, L. Leroy, and J.-L. Oudar, "Thermal optimization of 1.55 μm OP-VECSEL with hybrid metal-metamorphic mirror for single-mode high power operation," Opt. Quantum Electron. **40**, 155–165 (2008).
[19]V. M. Korpijärvi, E. L. Kantola, T. Leinonen, R. Isoaho, and M. Guina, "Monolithic GaInNAsSb/GaAs VECSEL operating at 1550 nm," IEEE J. Sel. Top. Quantum Electron. **21**, 480–484 (2015).
[20]A. Sirbu, N. Volet, A. Mereuta, J. Lyytikäinen, J. Rautiainen, O. Okhotnikov, J. Walczak, M. Wasiak, T. Czyszanowski, A. Caliman, Q. Zhu, I. Vladimir, and E. Kapon, "Wafer-fused optically pumped VECSELs emitting in the 1310 nm and 1550 nm wavebands," Adv. Opt. Technol. **2011**, 1.
[21]E. J. Saarinen, J. Lyytikäinen, S. Ranta, A. Rantamäki, A. Saarela, A. Sirbu, V. Iakovlev, E. Kapon, and O. G. Okhotnikov, "A 1.5 W frequency doubled semiconductor disk laser tunable over 40 nm at around 745 nm," Proc. SPIE **9734**, 103–110 (2016).
[22]K. Nechay, A. Mereuta, C. Paranthoën, G. Brévalle, C. Levallois, M. Alouini, N. Chevalier, M. Perrin, G. Suruceanu, A. Caliman, M. Guina, and E. Kapon, "InAs/InP quantum dot VECSEL emitting at 1.5 μm," Appl. Phys. Lett. **115**, 171105 (2019).
[23]A. Mereuta, K. Nechay, A. Caliman, G. Suruceanu, A. Rudra, P. Gallo, M. Guina, and E. Kapon, "Flip-chip wafer-fused OP-VECSELs emitting 3.65 W at the 1.55 m waveband," IEEE J. Sel. Top. Quantum Electron. **25**, 1–1 (2019).
[24]M. Herper, A. van der Lee, J. Kolb, S. Gronenborn, H. Moench, and P. Loosen, "VCSEL pumped VECSEL concept with compact design," Electron. Lett. **55**, 705–707 (2019).
[25]A. Laurain, J. Hader, and J. V. Moloney, "Modeling and optimization of transverse modes in vertical-external-cavity surface-emitting lasers," J. Opt. Soc. Am. B **36**, 847–854 (2019).
[26]A. R. Albrecht, T. J. Rotter, C. P. Hains, A. Stintz, J. V. Moloney, K. J. Malloy, and G. Balakrishnan, "Multi-watt 1.25 μm quantum dot VECSEL," Electron. Lett. **46**, 856–857 (2010).
[27]B. Heinen, F. Zhang, M. Sparenberg, B. Kunert, M. Koch, and W. Stolz, "On the measurement of the thermal resistance of vertical-external-cavity surface-emitting lasers (VECSELs)," IEEE J. Quantum Electron. **48**, 934–940 (2012).
[28]A. Laurain, M. Myara, G. Beaudoin, I. Sagnes, and A. Garnache, "High power single-frequency continuously-tunable compact extended-cavity semiconductor laser," Opt. Express **17**, 9503–9508 (2009).
[29]C. Paranthoën, C. Levallois, G. Brévalle, M. Perrin, A. Le Corre, N. Chevalier, P. Turban, C. Cornet, H. Folliot, and M. Alouini, "Low threshold 1550 nm emitting QD optically pumped VCSEL," IEEE Photonics Technol. Lett. **33**, 69–72 (2021).
[30]Z. Yang, A. R. Albrecht, J. G. Cederberg, and M. Sheik-Bahae, "80 nm tunable DBR-free semiconductor disk laser," Appl. Phys. Lett. **109**, 022101 (2016).
[31]C. M. N. Mateo, U. Brauch, H. Kahle, T. Schwarzbäck, M. Jetter, M. Abdou Ahmed, P. Michler, and T. Graf, "2.5 W continuous wave output at 665 nm from a multipass and quantum-well-pumped AlGaInP vertical-external-cavity surface-emitting laser," Opt. Lett. **41**, 1245–1248 (2016).
[32]P. J. Rodrigo and C. Pedersen, "Comparative study of the performance of semiconductor laser based coherent doppler lidars," Proc. SPIE **8241**, 292–298 (2012).
[33]Q. Hu, P. J. Rodrigo, and C. Pedersen, "Remote wind sensing with a CW diode laser lidar beyond the coherence regime," Opt. Lett. **39**, 4875–4878 (2014).
[34]S. Wu, B. Liu, J. Liu, X. Zhai, C. Feng, G. Wang, H. Zhang, J. Yin, X. Wang, R. Li, and D. Gallacher, "Wind turbine wake visualization and characteristics analysis by Doppler lidar," Opt. Express **24**, A762–A780 (2016).

PUBLICATION

IV

Thermal behavior and power scaling potential of membrane external-cavity surface-emitting lasers (MECSELs)

H.-M. Phung, P. Tatar-Mathes, A. Rogers, P. Rajala, S. Ranta, H. Kahle and M. Guina

XXX (2021). Submitted for publication to IEEE Journal Quantum Electronics
DOI: N/A